



INDIAN OCEAN CIRCULATION AND CLIMATE VARIABILITY

Friedrich A. Schott,^{1,2} Shang-Ping Xie,³ and Julian P. McCreary Jr.³

Received 16 September 2007; revised 18 February 2008; accepted 29 July 2008; published 27 January 2009.

[1] In recent years, the Indian Ocean (IO) has been discovered to have a much larger impact on climate variability than previously thought. This paper reviews climate phenomena and processes in which the IO is, or appears to be, actively involved. We begin with an update of the IO mean circulation and monsoon system. It is followed by reviews of ocean/atmosphere phenomenon at intraseasonal, interannual, and longer time scales. Much of our review addresses the two important types of interannual variability in the IO, El Niño–Southern Oscillation (ENSO)

and the recently identified Indian Ocean Dipole (IOD). IOD events are often triggered by ENSO but can also occur independently, subject to eastern tropical preconditioning. Over the past decades, IO sea surface temperatures and heat content have been increasing, and model studies suggest significant roles of decadal trends in both the Walker circulation and the Southern Annular Mode. Prediction of IO climate variability is still at the experimental stage, with varied success. Essential requirements for better predictions are improved models and enhanced observations.

Citation: Schott, F. A., S.-P. Xie, and J. P. McCreary Jr. (2009), Indian Ocean circulation and climate variability, *Rev. Geophys.*, *47*, RG1002, doi:10.1029/2007RG000245.

1. INTRODUCTION

[2] Until quite recently, it was generally accepted that the influence of the Indian Ocean (IO) on climate variability, beyond its probable impact on the monsoons, was not appreciable. This view has changed profoundly recently, particularly since 1997, with new evidence indicating an important climatic role of IO sea surface temperature (SST) both within the region and in other sectors of the globe. By many measures, 1997 was an extraordinary year for the IO and countries on its rim. Record rainfall was observed in East Africa during October and November. Severe flooding in Somalia, Ethiopia, Kenya, Sudan, and Uganda caused several thousand deaths and displaced hundreds of thousands of people. On the other side of the IO, Indonesia suffered severe droughts at the same time, and wild fires broke out of control on several of its islands. The smoke and haze they generated caused severe health problems in Indonesia and surrounding countries. Not all of these climatic anomalies were due to the El Niño of the century; unusual conditions in the tropical IO made them worse. Among other things, the usual westerly winds switched to easterlies during July–November, and the otherwise typical eastward equatorial surface current never

developed during boreal fall. Efforts to determine the physical cause of the extraordinary 1997 event led to rapid progress in understanding IO air-sea interaction and modes of climate variability.

[3] The tropical Indian Ocean forms the major part of the largest warm pool on Earth, and its interaction with the atmosphere plays an important role in shaping climate on both regional and global scales. It exhibits a number of modes of climate variability, ranging from intraseasonal-to-interannual and longer time scales, most of which are coupled to the strong seasonal cycle. It differs from the Atlantic and Pacific in a number of climatically important ways. For one thing, the IO is bounded to the north by the Asian continent, preventing northward heat export and only allowing weak ventilation of the IO thermocline from the north. For another, the Asian continent drives the strongest monsoon on Earth, and the monsoonal winds generate large seasonal variations in ocean currents, many of which display annual reversals such as the Somali Current and the Southwest/Northeast Monsoon Current south of India/Sri Lanka. Equally important, the IO lacks steady equatorial easterlies, a consequence of the rising branch of the IO Walker circulation being anchored over the maritime continent. As a result, there is no climatological equatorial upwelling in the eastern ocean, in contrast to the other two tropical oceans. Instead, upwelling occurs in the Northern Hemisphere off northwest Africa and the Arabian peninsula and east and west of the tip of India and in the Southern Hemisphere along the northern edge of the southeast trades.

¹Leibniz Institut für Meereswissenschaften an der Universität Kiel, Kiel, Germany.

²Deceased 30 April 2008.

³International Pacific Research Center, University of Hawai'i, Honolulu, Hawaii, USA.

The northern upwelling is supplied by a shallow cross-equatorial cell (CEC) that again does not exist in the other oceans and carries most of the cross-equatorial heat transport. Finally, the IO has a low-latitude exchange route with the Pacific, the Indonesian Throughflow (ITF).

[4] In this paper, we review current evidence that supports the IO's influence on climate variability. Specifically, we report on climate phenomena for which IO SST anomalies are known (or hypothesized) to feed back to the atmosphere and on the oceanic processes that generate those SST anomalies. We begin with an overview of the climatological forcings and upper ocean circulations in the IO that provide the background state about which climate signals develop (section 2). We then discuss IO climate phenomena sorted by time scale. (This division is practical and sensible but not perfect since phenomena at different time scales interact significantly.) Section 3 discusses intraseasonal variability, one of the primary processes affecting rainfall in the region. Section 4 reviews interannual climate variability, for which the two major signals are the El Niño–Southern Oscillation (ENSO) and the Indian Ocean Dipole (IOD; also called the Indian Ocean Zonal Mode). Section 5 considers variability at decadal and longer time scales, including the secular warming trend that has occurred since the 1950s. Section 6 provides a summary on the new discoveries and discusses remaining challenges.

[5] Several review papers have been published previously on IO circulation and climate variability. *Schott and McCreary* [2001] (hereinafter referred to as SMC01) is a review of IO circulation, and section 2 updates this review. *Yamagata et al.* [2004], *Annamalai and Murtugudde* [2004], and *Chang et al.* [2006] focus mostly on the IOD mode, southwest IO Rossby waves, and their climatic influences. Our review is broader in scope, covering time scales from intraseasonal to secular trends. It presents the latest advances in ocean circulation studies and in the description and understanding of modes of IO climate variability, including their predictability and remote influences.

2. OCEAN CIRCULATIONS AND PROCESSES

[6] In much of this section, we review aspects of the IO climatological circulation that impact SST, namely, the ocean and atmosphere fields that interact at the air-sea interface (section 2.1), near-surface currents (section 2.2), the shallow meridional overturning circulations that carry cool subsurface water to upwelling regions (section 2.3), and the interocean circulations that connect the IO to the other oceans (section 2.4). We conclude with a general discussion of the oceanic processes that are known (or expected) to alter IO SST and, hence, climate variability (section 2.5).

2.1. Air-Sea Interface

2.1.1. Winds

[7] South of about 10°S, the southeast trades are relatively steady (Figure 1), with their northern edge shifting northward (southward) during the northern summer and fall

(winter and spring). In contrast, north of 10°S the winds vary markedly, reversing direction with the monsoons (Figures 1a and 1c). A striking, and dynamically important, difference from the other tropical oceans is the absence of sustained easterly winds along the equator. Instead, the near-equatorial winds have an easterly component only during the late winter/early spring (Figure 1a), a semiannual westerly component during both intermonsoons (Figures 1b and 1d), and a weak westerly annual mean.

2.1.2. Thermocline Depth

[8] One measure of the dynamical response of the ocean to wind forcing is the depth of the thermocline. To illustrate, Figure 1 also plots the depth of the 20°C isotherm (Z20; shading), a typical midthermocline isotherm in the tropical ocean, from the Simple Ocean Data Assimilation (SODA) product [*Carton et al.*, 2000]. It is deeper in regions of Ekman convergence, i.e., where the Ekman pumping velocity w_{ek} is negative. (The wind-driven Ekman transports are given by $\mathbf{M}_e = (M^x, M^y) = (1/\rho_o)\hat{\mathbf{k}} \times (\boldsymbol{\tau}/f)$, where $\boldsymbol{\tau}$ is the wind stress vector, $\hat{\mathbf{k}}$ is a unit vector in the z direction, and f is the Coriolis parameter. They are directed to the right (left) of $\boldsymbol{\tau}$ in the Northern (Southern) Hemisphere. The Ekman pumping velocity is the divergence of \mathbf{M}_e , that is, $w_{ek} = -\nabla \cdot \mathbf{M}_e = (1/\rho_o)\hat{\mathbf{k}} \cdot \nabla \times (\boldsymbol{\tau}/f)$, and so is closely related to the wind stress curl.) One such region is the subtropical gyre south of 10°S, which resembles conditions in the other subtropical oceans. Another is the interior of the Arabian Sea during the summer (Figure 1c), where Ekman transports converge southeast of the axis of the maximum monsoon (Findlater) jet.

[9] More importantly for climate, Z20 is shallow in regions where w_{ek} is positive and in coastal regions where the alongshore winds are upwelling favorable. It is in these regions where upwelling of cool subsurface water is possible. Particularly noteworthy for our purposes are the regions of shallow Z20 in the tropical southwestern IO (SWIO) from 5 to 10°S throughout the year, where Ekman drift transports water southwestward from the northern edge of the trades. During the summer monsoon, pronounced upwelling also occurs in the western Arabian Sea where the alongshore winds cause offshore Ekman transports (Figure 1c) and east and west of the tip of India where positive wind stress curl causes local isopycnal doming and open ocean upwelling. Conditions are also favorable for upwelling off Java and Sumatra during boreal summer, an important process during IOD events (section 4.2.1). Typically, however, warm-water pulses are carried eastward twice annually along the equator by surface jets, called Wyrтки Jets after their discoverer [*Wyrтки*, 1973]; they deepen the thermocline along the eastern IO boundary in the late phase of the semiannual intermonsoon westerlies and weaken or eliminate upwelling there (section 2.2.3).

2.1.3. SST and Precipitation

[10] Precipitation over the IO shows a general migration, northward (southward) during the boreal summer (winter), following the Sun and regions of warm SST. Wintertime cooling in the northern Arabian Sea is particularly strong because of latent heat loss caused by cool, dry air blowing

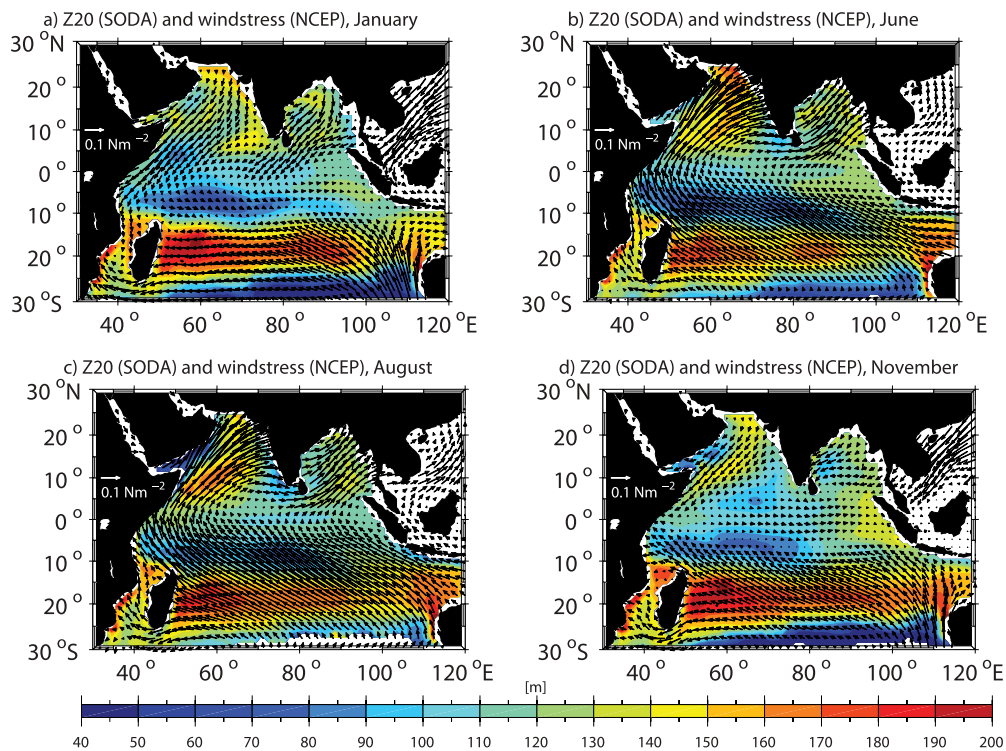


Figure 1. Monsoon wind stress fields from the 1990–1998 National Centers for Environmental Prediction (NCEP) [Kalnay et al., 1996] climatology (vectors) and depths of 20°C isotherm (Z20) from Simple Ocean Data Assimilation (SODA) (mean for 1992–2001, color shaded) for (a) January, (b) June, (c) August, and (d) November.

off the Asian continent (Figure 2a). Against these seasonal tendencies, there is strong summertime cooling in the western Arabian Sea (Figure 2b), a result of upwelling near, and offshore advection from, the Somali and Omani coasts and of latent heat loss caused by the strong southwesterly winds of the Findlater Jet. Cooling in the 5–10°S band and

off India is not apparent in SST because the upwelling in these open ocean divergence regions is weaker than the concentrated coastal upwelling off northwest Africa and Arabia.

[11] The precipitation patterns are remarkably similar to those for SST, indicative of the strong coupling between the

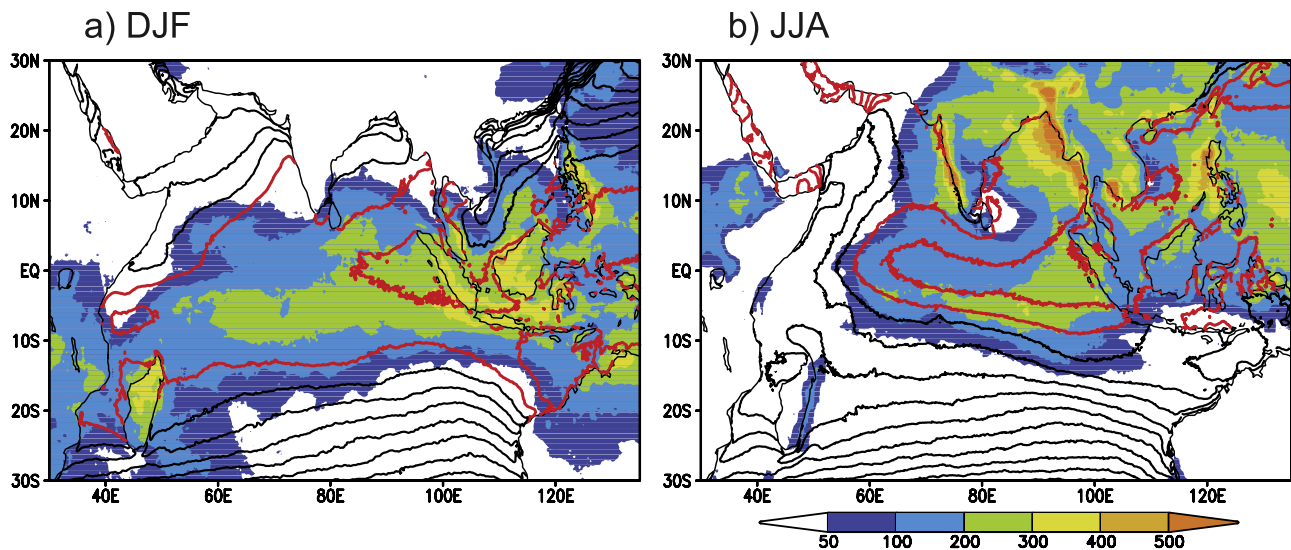


Figure 2. (a) December, January, and February (DJF) and (b) June, July, and August (JJA) climatology of sea surface temperature (SST) (intervals at 1°C; 28°C or higher in red) and precipitation (color shade in mm/month) based on advanced very high resolution radiometer [Armstrong and Vazquez-Cuervo, 2001] and Tropical Rain Measuring Mission [Huffman et al., 2007] satellite observations, respectively.

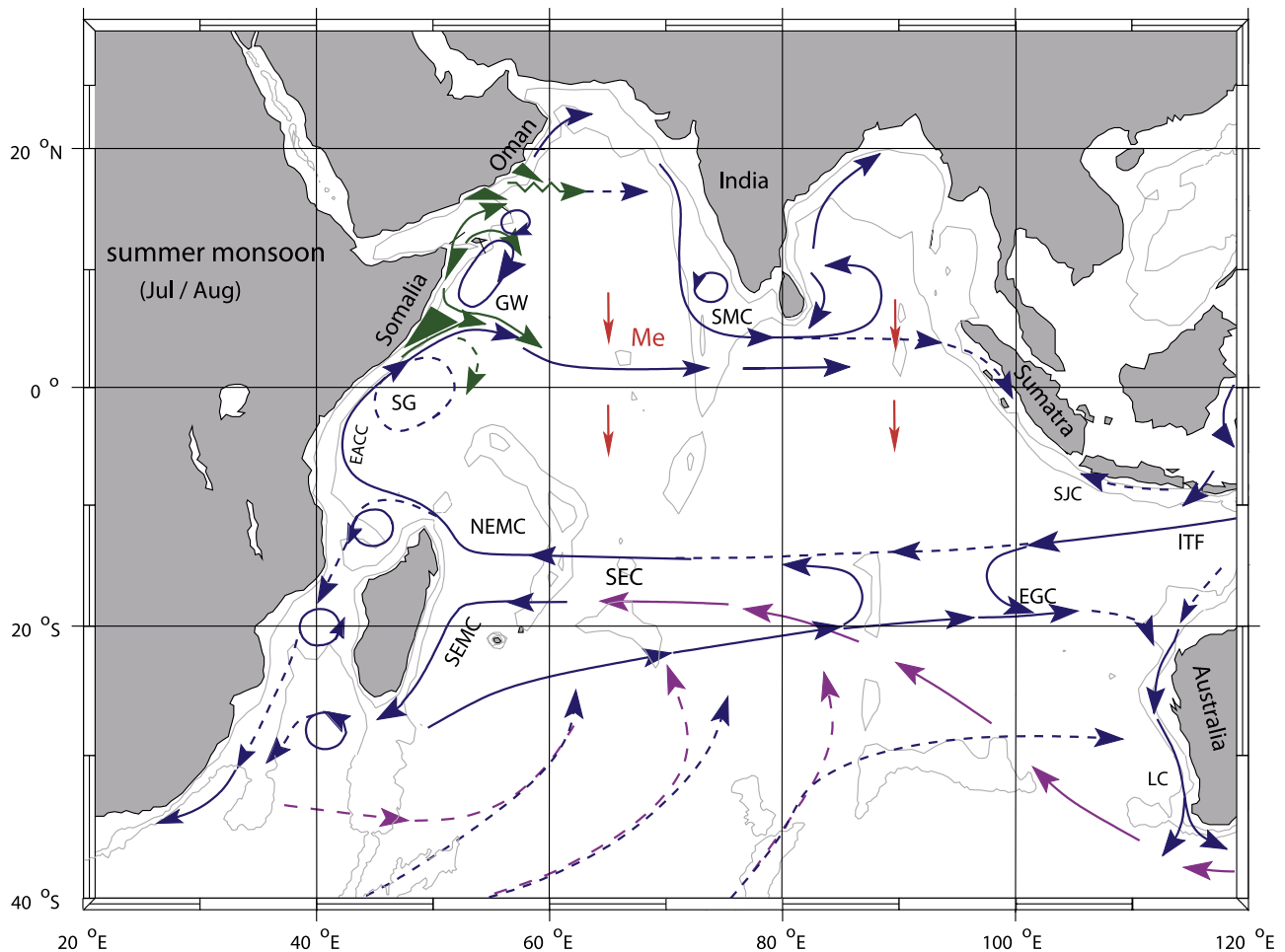


Figure 3. Schematic representation of identified current branches during the summer (southwest) monsoon. Current branches indicated (see also Figure 4) are the South Equatorial Current (SEC), South Equatorial Countercurrent (SECC), Northeast and Southeast Madagascar Current (NEMC and SEMC), East African Coastal Current (EACC), Somali Current (SC), Southern Gyre (SG) and Great Whirl (GW) and associated upwelling wedges (green shades), Southwest and Northeast Monsoon Currents (SMC and NMC), South Java Current (SJC), East Gyral Current (EGC), and Leeuwin Current (LC). The subsurface return flow of the supergyre is shown in magenta. Depth contours shown are for 1000 m and 3000 m (grey). Updated representations are from SMC01; red vectors (Me) show directions of meridional Ekman transports. ITF indicates Indonesian Throughflow.

two fields. During summer, the cooling by upwelling off Somalia keeps atmospheric convection from the western Arabian Sea. Elsewhere north of the equator, from the eastern Arabian Sea to the South China Sea, SST is high and conducive to atmospheric deep convection. There, the Asian summer monsoon is organized into several well-defined convection centers, all anchored by mountain ranges [Xie *et al.*, 2006].

2.2. Upper Ocean Circulation

[12] Figures 3 and 4 provide schematic diagrams that summarize the near-surface flow field in the IO during the summer and winter monsoon periods, respectively. In the Northern Hemisphere, where the observational knowledge base was well established by the large experiments of the mid-1990s, the schematic flow paths have not changed since the publication of SMC01. In the southern IO, however, several circulation elements are now quantified

that were only qualitatively known at the time of SMC01, and pathways have changed. (Compare Figures 8 and 9 of SMC01 with our revised schematic diagrams.)

2.2.1. Southern Indian Ocean

2.2.1.1. Westward South Equatorial Current and Southward Western Boundary Currents

[13] The South IO is characterized by the westward flowing South Equatorial Current (SEC), to a large part supplied by the ITF (Figure 3). It splits at the east coast of Madagascar near 17°S into northward and southward branches, the Northeast and Southeast Madagascar Currents (NEMC and SEMC). The NEMC transports about 30 Sv (SMC01), supplying water for the Mozambique Channel flow and the East African Coastal Current (EACC; Figure 3). The southward branch transports about 20 Sv to the southern tip of Madagascar, where it is suggested to dissolve into a sequence of eddies and dipoles that migrate to the African coast [de Ruijter *et al.*, 2004; Quartly *et al.*, 2006]. Part of

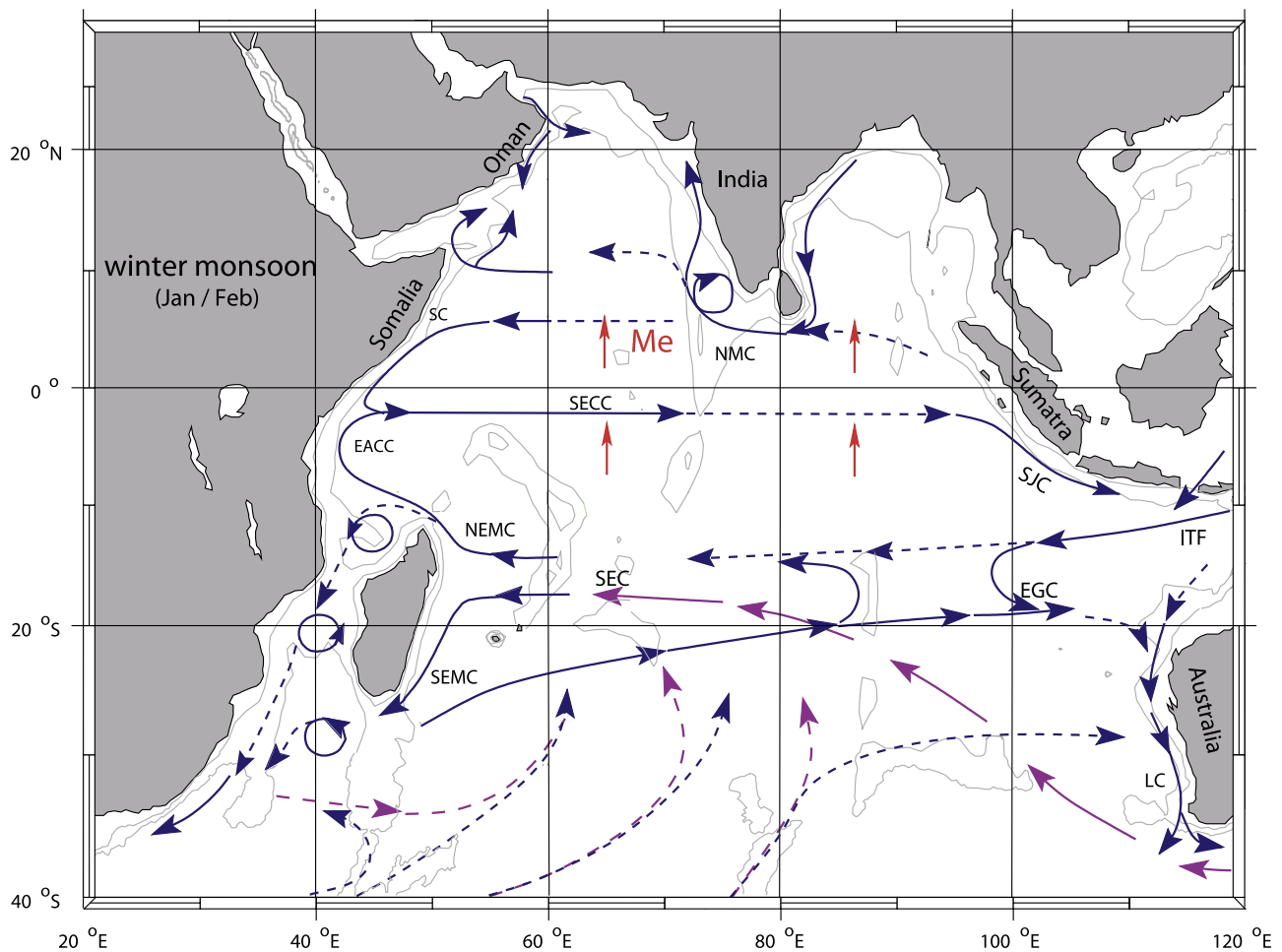


Figure 4. As in Figure 3 but for the winter (northeast) monsoon.

the SEMC may also retroflect to supply the northeastward flow east of Madagascar (see below).

[14] Since the publication of SMC01, the transport through the Mozambique Channel has emerged as a major thoroughfare of tropical/subtropical exchange. Its mean transport has been estimated at 17 Sv from a multiyear moored array [*de Ruijter et al.*, 2002], and a similar value was obtained in hydrographic section analysis [*Donohue and Toole*, 2003], in agreement with earlier inverse model results of 15 ± 5 Sv [*Ganachaud et al.*, 2000]. The transport is not carried by a quasi-laminar boundary current, however, but rather by migrating anticyclonic eddies (Figure 3). It has been suggested that after propagating farther southward along the South African coast, they trigger eddies of the Agulhas retroflection and thus affect the transfer of IO waters into the Atlantic [*de Ruijter et al.*, 2002; *Penven et al.*, 2006].

2.2.1.2. Northeastward and Eastward Flows

[15] Figure 5a presents the mean geostrophic near-surface circulation of the subtropical IO, based on the absolute surface topography derived from drifter velocities and altimetry [*Niiler et al.*, 2003; *Maximenko and Niiler*, 2005]. Streamlines of the surface geostrophic flow follow the map contours, indicating that eastward outflow from the Agulhas retroflection reenters the IO as a broad north-

eastward flow, much of which extends to the west coast of Australia. Recent studies of ship sections and altimetry, however, support the existence of a narrow zonal counter-current across the subtropics from 22 to 26°S, the South Indian Counter Current (SICC [*Siedler et al.*, 2006; *Palastanga et al.*, 2007]), which is somewhat at odds with the zonally slanted absolute surface topography of Figure 5a. Figure 5b presents a map of near-surface currents from the SODA–Parallel Ocean Program (POP) 2.0.3 reanalysis [*Carton and Giese*, 2008] that seems to reconcile both concepts. The plotted currents are taken from a depth of 46 m so as to illustrate the geostrophic flow just below the Ekman layer. On the one hand, it supports the existence of an intensified zonal eastward flow near 25°S; on the other, it shows that the band of eastward flow expands latitudinally to the east, allowing a connection from south of Madagascar to northwest Australia. The SODA-POP reanalysis also suggests that the eastward upper layer flow and SICC are supplied partly by a retroflection of the SEMC and partly from a source farther to the west. Part of the eastward flow also recirculates northwestward into the SEC.

[16] Persistent eastward geostrophic flow, the East Gyrals Current (EGC; Figures 3 and 4), was observed near and north of 20°S in the Perth–Indonesia expendable bathythermograph (XBT) ship sections (World Ocean Circulation

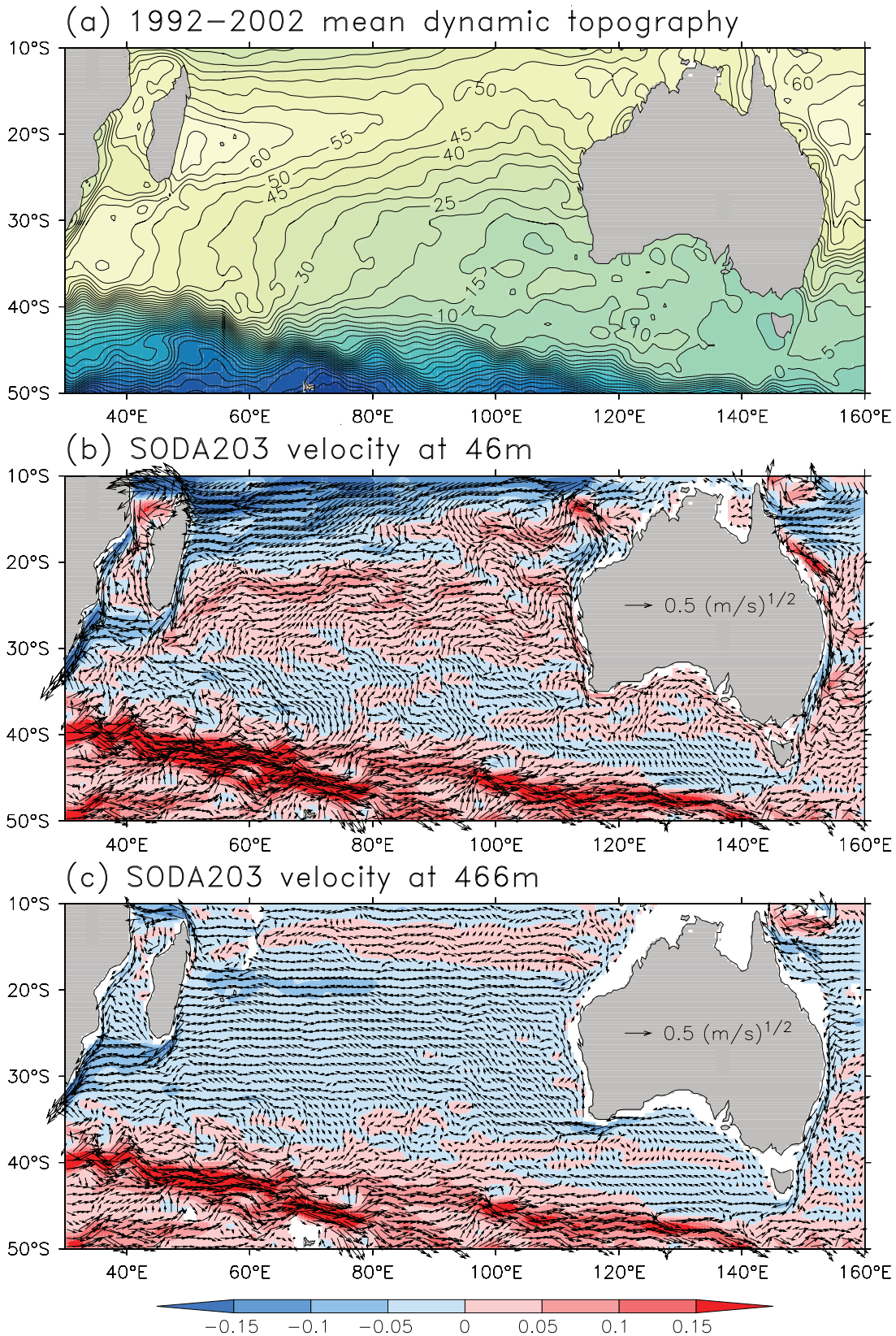


Figure 5. (a) Mean sea surface topography (cm), based on merged drifter velocities and altimetry (courtesy N. Maximenko); (b) currents of the SODA–Parallel Ocean Program (POP) 2.0.3 assimilation model, presented as $(\text{m/s})^{1/2}$ for better vector visibility (courtesy B. Giese and R. Furue) at 46 m depth, showing eastward upper layer flow and suggestions of an eastward countercurrent near 25°S; and (c) as in Figure 5b but for 466 m depth, showing westward midthermocline countercurrent across the subtropics.

Experiment line IX-1) across the ITF regime and was found to be strongest at the beginning of the year [Meyers, 1996]. The EGC is supplied both from the north by recirculation out of the ITF/SEC (Figures 3 and 5) [see also Domingues et al., 2007, Figure 11a] and by the aforementioned northeastward flow that extends to the Agulhas retroflexion.

2.2.2. Northern Indian Ocean

2.2.2.1. Summer Monsoon

[17] During the summer monsoon, the SEC and EACC supply the northward Somali Current. Depending on the time of the season and driving wind field, the Somali Current can appear as a set of different cells and gyres (SMC01). Figure 3 shows the typical situation for the fully developed summer monsoon. After crossing the equator, part of the low-latitude Somali Current turns offshore near 4°N, with a cold upwelling wedge on its left shoulder, and part recirculates across the equator as the “Southern Gyre.” In the north, a second gyre is formed, the “Great Whirl.” A third gyre, the “Socotra Eddy,” is seen in many summer monsoons northeast of Socotra (Figure 3). Interestingly, the upwelling wedges and filaments associated with these features impact the stability of the atmospheric planetary boundary layer, significantly affecting the surface wind stress and heat fluxes [Vecchi et al., 2004]. Elsewhere, the Southwest Monsoon Current flows eastward south of Sri Lanka (Figure 3) and then turns northward to bring saltier Arabian Sea water into the Bay of Bengal [Jensen, 2003].

2.2.2.2. Winter Monsoon

[18] During the winter monsoon, the Somali Current flows southward. It meets the northward flowing EACC in a confluence zone from 2 to 4°S, supplying water for the eastward flowing South Equatorial Countercurrent (SECC, Figure 4). As shown earlier in the model study of McCreary et al. [1993], in model particle trajectory studies [Song et al., 2004, Figure 12], and also in the SODA-POP 2.0.3 reanalysis, the SECC is a feature that exists year round, except that during the summer monsoon it is subsurface, masked by overlying westward Ekman currents (see section 2.3). The Northeast Monsoon Current flows westward across the basin during this season, carrying fresher Bay of Bengal water into the Arabian Sea. As model studies have suggested, Bay of Bengal water is also transported across the equator in the eastern basin during this season [Han and McCreary, 2001; Jensen, 2003].

2.2.3. Equatorial Regime

[19] A remarkable IO phenomenon is the occurrence of strong eastward surface jets during the intermonsoon periods, commonly referred to as Wyrtki Jets (WJs). They are unique to the IO, owing their existence to the semiannual westerly equatorial winds (Figures 1b and 1d). The WJs are climatically important because they carry warm upper layer waters eastward, thereby increasing sea level and mixed layer thickness in the east and decreasing them in the west. The WJs reflect from the eastern boundary of the basin as packets of coastal Kelvin and Rossby waves, thereby extending their impact well off the equator (section 2.5). The interaction of reflected equatorial waves with directly wind-forced waves in generating the seasonal cycle of the

equatorial regime was recently explored by Yuan and Han [2006], in a comparison of model analysis and observations. As mentioned in section 2.1, the WJs affect the upwelling regime off Sumatra, thus impacting IOD preconditioning.

[20] The lack of sustained equatorial easterlies is also the reason for another IO peculiarity in that an eastward Equatorial Undercurrent (EUC) exists only during part of the year, typically February–June when the winds have an easterly component. The EUC can appear in other seasons as well but only when anomalous easterlies occur [Reppin et al., 1999].

2.3. Meridional Overturning Cells

[21] The Pacific and Atlantic oceans each have two shallow meridional overturning circulations, the northern and southern subtropical cells (STCs), in which cool surface water subducts in the subtropics, flows to the equator within the thermocline, and upwells to the surface in the eastern, equatorial ocean [Schott et al., 2004]. Because the IO lacks sustained equatorial easterlies, its primary upwelling regions are located in off-equatorial regions where the thermocline is shallow: along the coasts of Somalia and Oman, near the tip of India, and along the 5–10°S thermocline ridge (Figures 1a and 6a). These upwellings drive the ascending branches of the IO’s primary shallow overturning circulations, namely, the CEC and the southern STC.

2.3.1. Cross-Equatorial Cell

[22] The meridional exchange of mass and heat between the hemispheres occurs predominantly by the CEC, as identified in both observations [Schott et al., 2002] and modeling studies [McCreary et al., 1993; Miyama et al., 2003; Schoenefeldt and Schott, 2006]. Figures 6a and 6b illustrate its horizontal and vertical structures. At thermocline levels, the CEC connects the SEC with the northern upwelling regions along the western boundary via a subsurface northward flowing part of the Somali Current. At the surface, it is closed by southward cross-equatorial Sverdrup transport in the interior ocean. Water for the CEC is supplied from three regions in the Southern Hemisphere: by recirculation within the subtropical gyre, from the subduction regions of the southeastern subtropics, and by the ITF (Figure 6a).

[23] A key process that drives the CEC is the mean southward cross-equatorial Sverdrup transport, determined by the zonally integrated wind stress curl along the equator. As noted by Godfrey et al. [2001] and Miyama et al. [2003], the zonal component of the winds nearly vanishes at the equator during both monsoons and is roughly proportional to the distance from the equator on either side ($\tau^x \propto y$). This special wind drives no geostrophic currents, and it follows that the cross-equatorial Sverdrup transport is equal to the Ekman drift, τ^x/f , which is well defined at the equator since both τ^x and f vanish there. The magnitude of the CEC is about 6 Sv [Schott et al., 2002, 2004], and despite its shallowness, it is the main agent of cross-equatorial heat transport variability [Schoenefeldt and Schott, 2006].

[24] On the equator, the winds in both monsoon seasons are directed meridionally and against the Ekman transports,

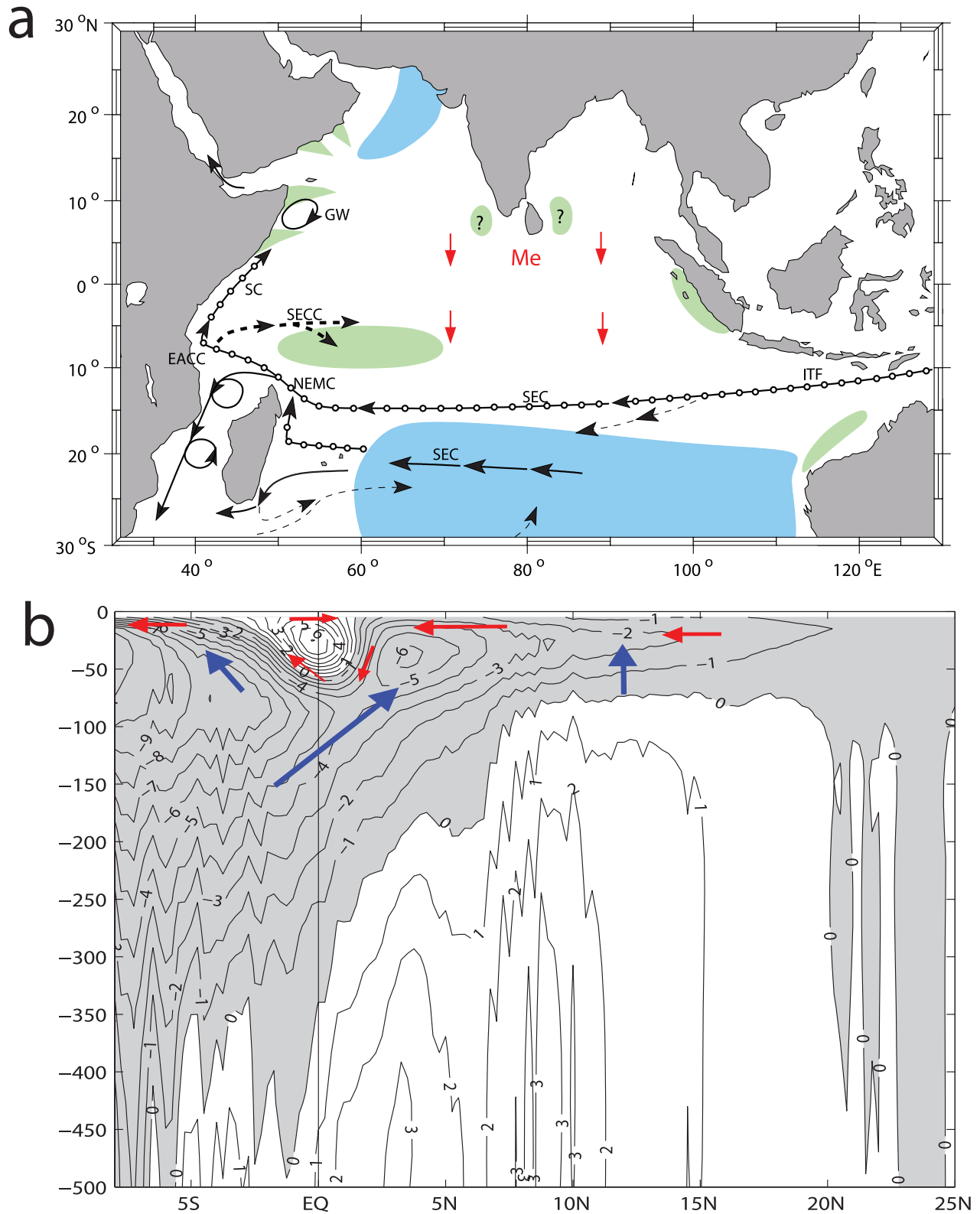


Figure 6. (a) Schematic representation of the Indian Ocean cross-equatorial cell (CEC) (light dashed stream paths for upper layer inflow into subduction zone (blue), dotted for thermocline Somali Current supply, and solid for Southern Hemisphere thermocline flow) and of the subtropical cell (STC) (heavy dashed supply route via SECC) along with upwelling zones (green) that participate in the CEC and STC. See Figure 3 for circulation names (based on Schott et al. [2004]). (b) Mean overturning stream function (units in Sv) of model used by Miyama et al. [2003] showing southward near-surface warm water flow by Ekman transports (red vectors), which have to “dive underneath” the equatorial roll, and upwelling (blue) supplying coastal upwelling regimes off Somalia and Arabia at 5–20°N and open ocean upwelling at 3–12°S.

causing a small near-surface equatorial overturning cell, the equatorial roll (Figure 6b) [*Wacongne and Pacanowski, 1996; Miyama et al., 2003*]. The roll, however, is almost entirely confined to the surface-mixed layer and thus does not impact the oceanic heat budget or climate.

2.3.2. Subtropical Cell

[25] In the southern IO, the upwelling from 5–10°S is driven by Ekman pumping along the northern edge of the southeast trade winds (Figure 1). It drives the Southern Hemispheric STC (Figure 6b), with a magnitude of about 8 Sv [*McCreary et al., 1993; Lee, 2004*]. As for the CEC, thermocline water for the STC is supplied by southern subduction, recirculation, and inflow from the ITF. These source waters first flow westward across the basin to the African coast, northward along the coast to about 5°S, and only then flow to the northern flank of the upwelling region within a subsurface part of the SECC as schematically indicated in Figure 6a.

2.3.3. Other Overturning Cells

[26] There are also weak upwelling regions in the eastern IO, off Sumatra/Java and northwest Australia in the Arafura Sea [*Godfrey and Mansbridge, 2000; SMC01; Du et al., 2005*] (Figure 6a). Both regimes are associated with overturning cells, the details of which still need further study. (The Sumatra/Java upwelling strengthens episodically during IOD events; see section 4.2.2.)

[27] Finally, the IO has a deep overturning circulation, marked by northward cores below 3500 m along the meridional ridges and southward return flow from 1000 to 3500 m [*Ganachaud et al., 2000*]. Since it is climatically relevant only at very long time scales, we do not consider it further here.

2.4. Interocean Circulations

[28] The IO is connected to the global circulation through the Indonesian passages and its open southern boundary. New evidence, which has become available since SMC01, has allowed a better quantification of the exchange associated with both pathways.

2.4.1. Indonesian Throughflow

[29] The ITF transports Pacific waters into the IO, mostly within the upper ocean (<400 m) and dominantly composed of North Pacific water from the Mindanao Current [*Gordon, 2005*]. The ITF transport also has a subsurface core at intermediate depths, most of which comes from the South Pacific [*Gordon, 2005; McCreary et al., 2007*]. In the Indonesian passages, drastic water mass modifications occur through tidal mixing and internal wave breaking [*Ffield and Gordon, 1992; Koch-Larrouy et al., 2007*], generating a new water mass, Banda Sea Water, that is identifiable by a salinity minimum along all of the SEC. From combined measurements in different passages, the mean ITF has been estimated to be about 10 Sv [*Gordon, 2005*]. Some global inverse model studies yield even higher mean ITF transports, such as 15 ± 4 Sv by *Ganachaud et al. [2000]* and 13 ± 2 Sv by *Lumpkin and Speer [2007]*. There is a seasonal cycle to the ITF, with maximum (minimum) outflow in June/July (February) and an amplitude of 3–4 Sv

(SMC01), and interannual variability related to ENSO and other forcing factors (section 4.1.6).

2.4.2. Supergyre

[30] While in the past, attention has been focused on Indo-Pacific exchange by the ITF, new observational results from float trajectories at 1000 m [*Davis, 2005*] and from high-resolution hydrographic data sets [*Ridgway and Dunn, 2007*] as well as model simulations [*Speich et al., 2002, 2007*] indicate that there is also a linkage south of Australia, one branch of a “supergyre” that connects all three oceans [*Cai, 2006*]. Figure 7 illustrates the supergyre in a solution to a numerical model [*Speich et al., 2007*], plotting Lagrangian parcel trajectories at various depths. Westward flow in the supergyre occurs at intermediate depths, with water from the East Australian Current flowing around South Australia, then across the IO within a deep part of the subtropical gyre, and eventually joining the Agulhas Current; farther west, it extends into the South Atlantic at surface and intermediate depths. The eastward branch occurs along the northern edge of the Antarctic Circumpolar Current, with shallower (deeper) water bending northward to enter the subtropical gyre of the Indian (Pacific) Ocean. Figure 5c illustrates this Indo-Pacific linkage in greater detail, showing currents at 466 m from the SODA-POP 2.0.3 reanalysis. There is a narrow westward current around Tasmania (an extension of the EAC); broad, weak westward flow south of Australia; and a well-defined jet off southwest Australia underneath the eastward flowing extension of the Leeuwin Current (Figure 5b). In the IO, flow at thermocline level, 200–700 m, is to the northwest (Figure 5c), passing below northeastward surface flow (Figures 5a and 5b).

[31] At its most basic level, the supergyre is a Sverdrup circulation that begins at the west coast of South America and continues around Australia and Africa because they do not extend as far south as South America. The Sverdrup circulation itself (a barotropic response), however, can only extend due west around Australia (from the tip of Tasmania, in fact) and so cannot enter the interiors of either the Indian or Atlantic oceans. For the westward branch of the supergyre to join the subtropical gyres in the Indian and Atlantic oceans, then, there must be considerable “local” baroclinic forcing south of Australia and in both the Indian and Atlantic oceans. For example, note in Figure 5c that there is not an obvious linkage between the strong jets south of Tasmania and southwest Australia, which points toward the importance of local forcing south of Australia. Processes that can drive intermediate flow into the IO are discussed by *Hirst and Godfrey [1993]* and *McCreary et al. [2007]*.

2.5. Processes

[32] A number of oceanic and coupled processes can produce SST anomalies that last long enough to affect climate. They divide into processes that are primarily dynamical and thermodynamical in nature.

2.5.1. Dynamical Processes

2.5.1.1. Upwelling and Thermocline Depth

[33] Any change in the upwelling of cool subsurface water can profoundly affect SST. Such changes can be

Lagrangian reconstruction of ORCA2 Global Thermohaline Circulation

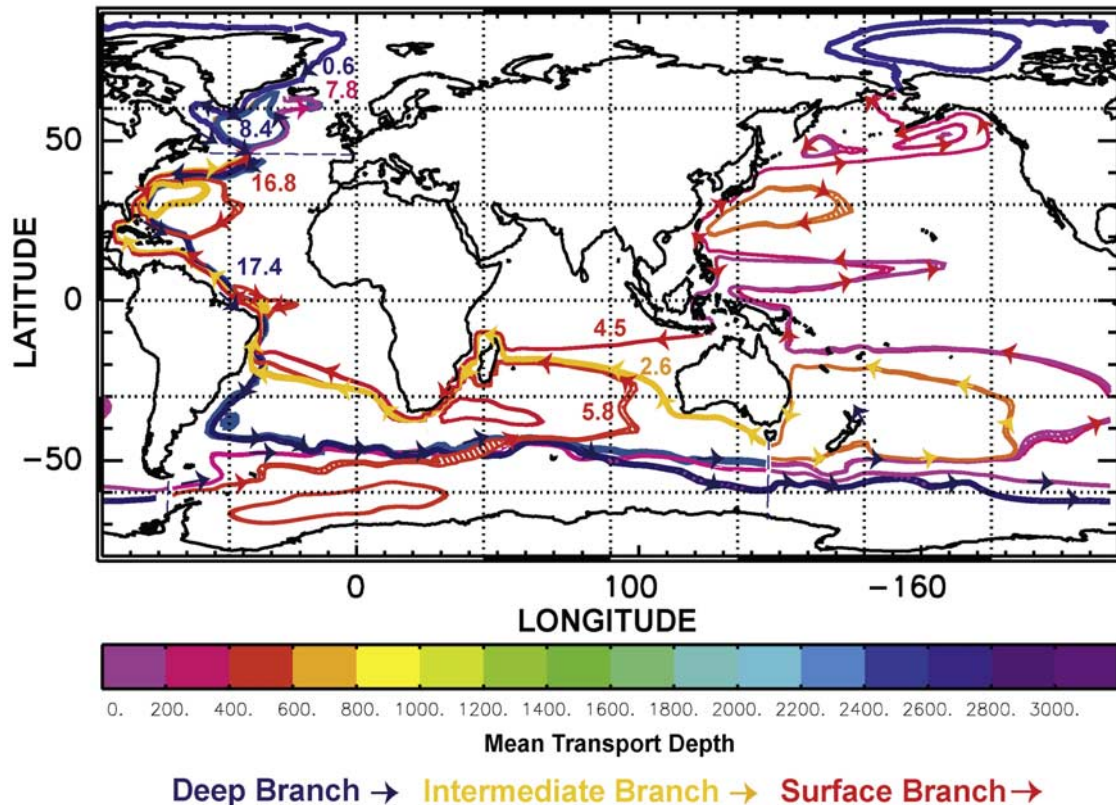


Figure 7. Lagrangian pathways of water parcels in global model simulation of *Speich et al.* [2007]. Colors indicate depths, and numbers are transports (in Sv).

directly forced by the atmosphere, by a modification of the winds that drive the upwelling. They can also be oceanographically forced by a change in the temperature of the water that upwells. As noted above, upwelling of cool water is confined to regions where the thermocline is shallow (Figures 1 and 6a; section 2.1). Because wind-driven upwelling is confined near the surface [e.g., *McCreary*, 1981], typically within the upper 100–200 m, it follows that a modest change of the thermocline depth can significantly change the temperature of the water that upwells and hence impact SST. Upwelling in the 5–10°S band and off Sumatra are key areas for this process in the IO (sections 2.1 and 4.2.2).

2.5.1.2. Remote Forcing and Waves

[34] Although changes in thermocline depth can be directly driven by the local winds, they can also be driven remotely via the propagation of baroclinic waves. Such waves are a prominent feature of the IO climatological circulation, with well-known effects on upwelling regions (SMC01). Their importance lies in the time it takes them to propagate across the basin (weeks to months), allowing predictability of SST variations months ahead of time (section 4.5). For example, consider the ocean's response to a patch of easterly wind centered on the equator: After the winds switch on, upwelling favorable equatorially trapped Kelvin waves radiate into the eastern ocean, shallowing the thermocline there; they reflect from the eastern boundary as packets of coastal Kelvin and

Rossby waves, spreading the shallowing well off the equator. At the same time, downwelling favorable Rossby waves propagate into the western ocean from the forcing region, deepening the thermocline there (section 4.2.2). Waves can also be generated in off-equatorial regions. Consider the response to forcing by an off-equatorial patch of anticyclonic (downwelling) Ekman pumping in the eastern ocean. In response, downwelling favorable Rossby waves radiate from the forcing region, deepening the thermocline in the western ocean (section 4.1.2).

[35] The ITF region also serves as a pathway for long waves to propagate between both oceans. Rossby waves from the Pacific can propagate through the passages into the IO with important climatic effects; for example, they can impact the thermocline depth in the 5–12°S belt, impacting SST there (section 4.1.2). Similarly, equatorial Kelvin waves that are generated by zonal wind stress variability in the equatorial IO can continue as coastal Kelvin waves into the Indonesian seas to modify the ITF profile and transport [*Wijffels and Meyers*, 2004; *Iskandar et al.*, 2005]. (If the Indonesian passages did not exist, these Kelvin waves would continue down the west Australian coast and shed midlatitude Rossby waves.) More than half of the intraseasonal transport variability in the main ITF passageway, Makassar Straits, can be explained by the combined lagged response to the zonal equatorial IO and Pacific winds (A. Gordon, personal communication, 2006).

2.5.1.3. Bjerknes Feedback

[36] *Bjerknes* [1969] proposed a coupled positive feedback process between the ocean and atmosphere that links all the above processes. Let $\Delta\tau^x$, Δh_e , Δw_e , and ΔSST_e be anomalies of zonal wind stress along the equator and of the thermocline depth, upwelling strength, and SST in the eastern equatorial ocean, respectively. Then, “Bjerknes feedback” is the positive interaction loop summarized by

$$\Delta\text{SST}_e \rightarrow \Delta\tau^x \rightarrow \Delta h_e \text{ and } -\Delta w_e \rightarrow \Delta\text{SST}_e. \quad (1)$$

The initial change can be either positive or negative, and the loop can start at any point in the cycle. For example, suppose that there is an initial decrease in SST_e . Then, according to (1), the equatorial easterlies, τ^x , strengthen in response to a stronger zonal SST gradient, leading to a shallowing of h_e by the equatorially trapped wave processes noted above, strengthened upwelling w_e , and a further decrease in SST_e .

2.5.2. Thermodynamic Processes

2.5.2.1. Mixed and Barrier Layers

[37] More subtle, yet also climatically relevant, is the near-surface stratification of temperature and salinity in regions of seasonally high precipitation or river discharge, forming barrier layers. Within a surface layer of quasi-homogeneous temperature, lighter freshwater on top may cause a density gradient not recognizable in the temperature profile, defining a surface “barrier” layer [*Godfrey and Lindstrom*, 1989]. Surface heat fluxes are then confined to these thin layers, warming the ocean more rapidly than might otherwise be expected. Barrier layers exist west of India [*Shenoi et al.*, 2004], in the Bay of Bengal [*Vinayachandran et al.*, 2007], and south of Indonesia [*Qu and Meyers*, 2005]. They often went unnoticed during the times of XBT temperature profiling from commercial vessels, which formed the bulk of upper layer observations since the 1970s. Their prevalence has recently become much more apparent, with the advent of autonomous Lagrangian profilers [e.g., *Davis*, 2005] as part of the Array for Real-Time Geostrophic Oceanography (Argo) project, which now provide near-global coverage of both temperature and salinity profiles (section 6.2).

2.5.2.2. Wind-Evaporation-SST Feedback

[38] A prominent thermodynamic interaction that can lead to positive feedback of the climate system is wind-evaporation-SST (WES) feedback. Let $\Delta\mathbf{v}$, Δw_s , and ΔE be anomalies of wind velocity, wind speed, and evaporation, and let \mathbf{v}_b be the background wind velocity. Then, WES feedback is summarized by the loop

$$\Delta\text{SST} \rightarrow \Delta\mathbf{v} + \mathbf{v}_b \rightarrow -\Delta w_s \rightarrow -\Delta E \rightarrow \Delta\text{SST}_e. \quad (2)$$

To illustrate this process, consider an initial meridional SST dipole anomaly with its positive (negative) pole north (south) of the equator, a situation that sometimes occurs in the equatorial Atlantic. Anomalous southerly cross-equatorial winds develop in response to the SST dipole, and Coriolis force bends the southerlies to have a westerly

(easterly) component north (south) of the equator. Under mean easterly conditions ($u_b < 0$) as for the Atlantic trades, w_s and E decrease (increase) north (south) of the equator, amplifying the SST dipole [*Xie and Philander*, 1994]. Note that an essential part of the loop is the connection between $\Delta\mathbf{v} + \mathbf{v}_b$ and Δw_s , which requires that \mathbf{v}_b interact with $\Delta\mathbf{v}$ in such a way as to weaken (strengthen) w_s in response to a positive (negative) ΔSST . In addition, it follows that WES feedback is likely to be stronger when the mixed layer is thin, as when there is a barrier layer, thereby allowing SST to respond more rapidly to anomalous heating by ΔE .

[39] Off the equator, WES feedback can cause coupled perturbations to propagate in the north-south direction (section 3.3 [*Xie*, 1999]). For simplicity, consider a zonally uniform band of warm SST north of the equator. An atmospheric thermal low forms over the band, driving westerly and easterly wind anomalies on its southern and northern flanks, respectively. Under mean westerlies, these wind anomalies strengthen (weaken) surface evaporation south (north) of the SST anomaly, causing a tendency for the SST anomaly to propagate northward. Such a situation is present over the Bay of Bengal during the summer monsoon, where it appears to enhance northward propagation of intraseasonal disturbances (section 3.3).

3. INTRASEASONAL VARIABILITY

[40] Several types of atmospheric intraseasonal oscillations (ISOs) are active in the IO, including eastward propagating Madden-Julian Oscillations (MJOs), northward propagating ISOs, and biweekly variability [*Chen and Chen*, 1993; *Chatterjee and Goswami*, 2004; *Fukutomi and Yasunari*, 2005]. Perhaps the most well-known type is the MJO (section 3.1). During the winter, they interact with the 5–10°S thermocline ridge, generating large SST anomalies there (section 3.2). During the summer, they spin off northward propagating ISOs, which impact rainfall over south Asia from India to the Philippines (Figure 8b; section 3.3). An extensive literature exists on MJO structure and dynamics and on atmospheric ISOs in general; see *Lau and Waliser* [2005] and *Zhang* [2005] for recent reviews. Here we limit our discussion to aspects of ISOs involving the IO. The ocean itself also exhibits intraseasonal variability, with biweekly variability being surprisingly strong in the central and eastern oceans (section 3.4).

3.1. MJOs

3.1.1. Properties

3.1.1.1. Atmosphere

[41] On the basis of analyses of tropical island observations, *Madden and Julian* [1972] first reported variability at periods of 30–60 days. These MJOs proved to be part of a planetary-scale mode of tropical variability, in which convection develops over the western tropical IO, propagates slowly eastward across the IO and maritime continent, and decays east of the international dateline, as schematically represented in Figure 8a. Associated with the eastward moving convective center are baroclinic circulations, with

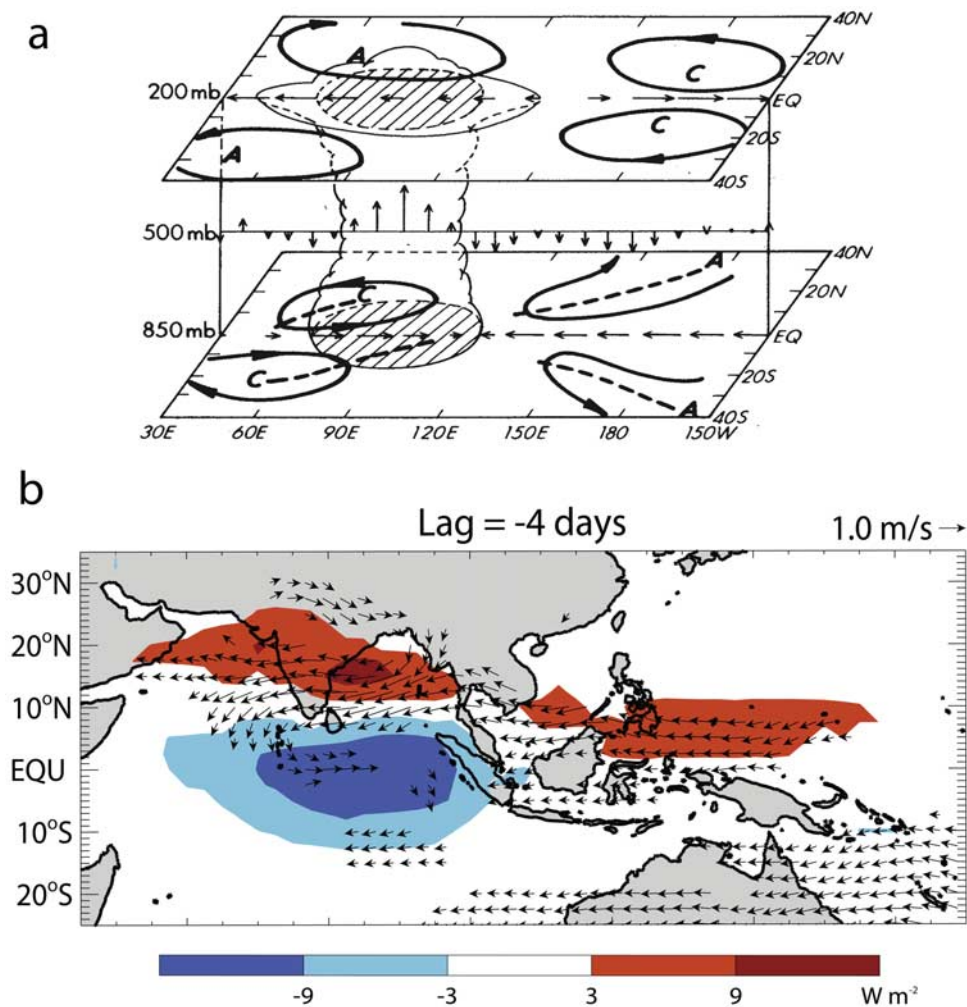


Figure 8. (a) Schematic representation of cyclonic (C) and anticyclonic (A) cells associated with the Madden-Julian Oscillations, showing their development in the Indian Ocean (IO) south of the equator [from *Rui and Wang*, 1990]. (b) Regression map for June–September at a lag of 4 days of outgoing longwave radiation (OLR) (shaded; interval is 3 W m^{-2} , and darkest shade $< -9 \text{ W m}^{-2}$) and 850-mbar wind (vectors; scale at top right) perturbations relative to a -1 standard deviation in OLR in the base region: $0\text{--}5^\circ\text{N}$, $85\text{--}90^\circ\text{E}$. All data are band-pass filtered to retain periods of 25–80 days prior to forming the regressions [from *Lawrence and Webster*, 2002].

anomalous easterlies in the lower troposphere east of the convection and anomalous westerlies west of it, much as depicted in the Matsuno-Gill model of the atmospheric response to an isolated heat source [*Hendon and Salby*, 1994]. These circulations in turn modulate the moisture field, atmospheric stability, and convection.

3.1.1.2. Ocean

[42] Coherent SST anomalies of $0.2^\circ\text{--}0.4^\circ\text{C}$ are observed to copropagate with MJOs in the tropical Indian and western Pacific oceans [e.g., *Kawamura*, 1988]. Variability in surface heat fluxes, latent heat flux and solar radiation in particular, is the dominant cause of the coherence, with typical ranges for surface zonal wind, latent heat flux, and surface solar radiation of $3\text{--}5 \text{ m/s}$, 80 W/m^2 , and 60 W/m^2 , respectively [*Shinoda et al.*, 1998]. East of the convection center, the anomalous easterlies are superimposed on mean westerlies, reducing the latent heat loss from the ocean; at the same time, the suppressed convection increases heating

by solar radiation. As a result, positive SST anomalies tend to lead MJO convection by about 90° in phase.

3.1.2. Dynamics

[43] The MJO is generally considered to be an intrinsic mode of atmospheric convection and circulation. While it seems clear that convection-circulation interactions give rise to the slow eastward propagation of MJOs (as compared to the much faster propagation of dry Kelvin waves), overall, MJO dynamics are still not well understood. One reason they are not is that MJOs are not well represented in state-of-the-art general circulation models (GCMs), exhibiting high sensitivity to physical parameterizations [*Slingo et al.*, 1996; *Lin et al.*, 2006]. In addition, several recent studies point toward the importance of coupled processes. For example, the inclusion of an interactive ocean generally improves the simulation of MJOs in comparison to their representation in stand-alone atmospheric GCMs forced by prescribed SST, with the MJOs displaying a more coherent

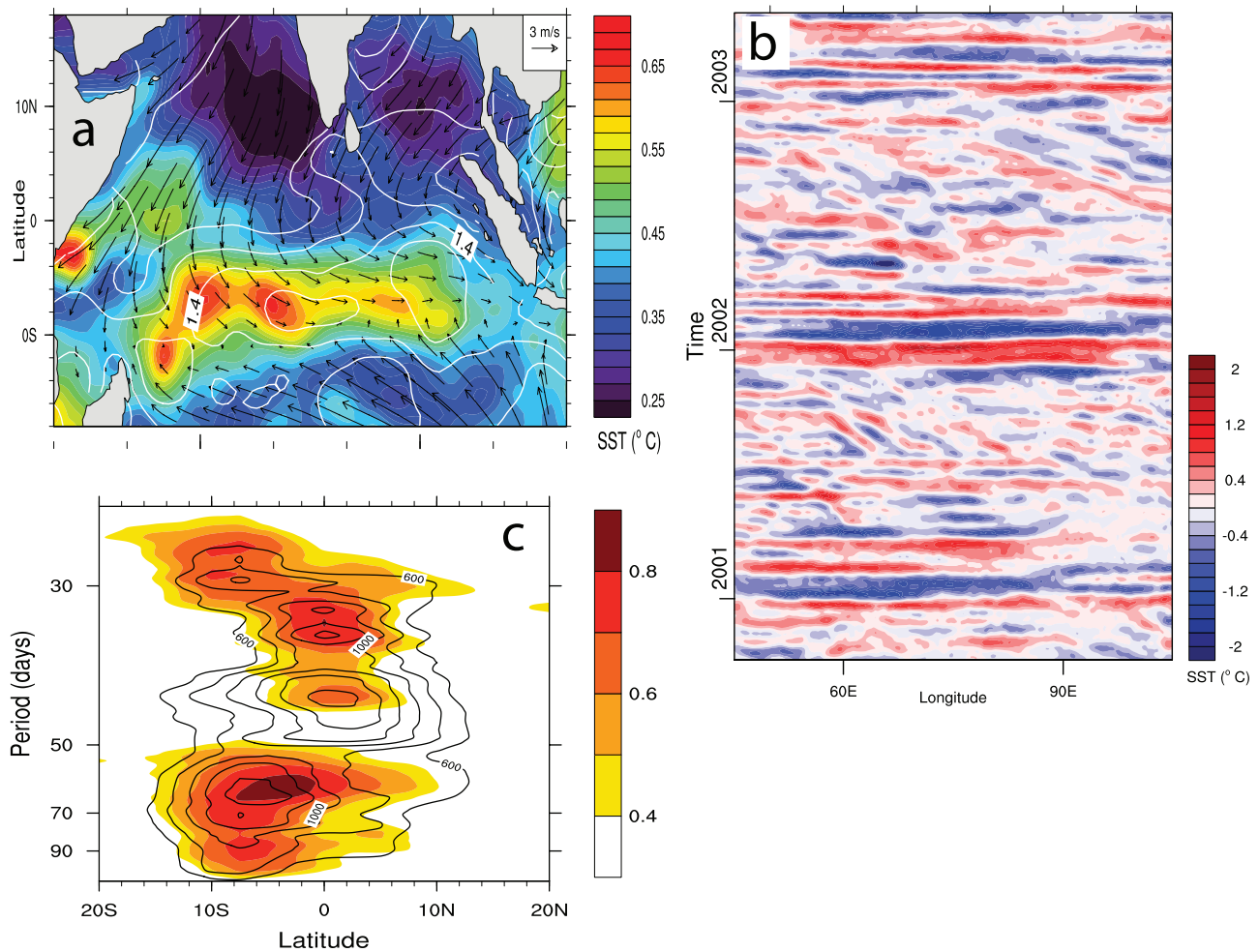


Figure 9. (a) Standard deviation of intraseasonal SST (color-shaded, °C) and wind speed (contours, m s^{-1}) anomalies during DJF superimposed on climatological wind velocity (vectors), (b) longitude-time section of band-passed (30–90 days) SST anomaly (°C) averaged in 10–5°S during 2000–2003, and (c) OLR power spectrum ($\text{W}^2 \text{m}^{-4}$) and SST-OLR coherence squared (shaded) and as a function of latitude and frequency for data averaged in 60–90°E during DJF [from Saji et al., 2006b].

eastward propagation [Inness et al., 2003; Zheng et al., 2004].

3.2. Wintertime ISOs

3.2.1. Properties

[44] Analyses of the Tropical Rain Measuring Mission (TRMM) satellite’s microwave imager (TMI) observations have revealed large intraseasonal SST variability in the 5–10°S band over the thermocline ridge (Figure 9a) [Harrison and Vecchi, 2001; Saji et al., 2006b; Duvel and Vialard, 2007]. (High cloudiness associated with active convection obscures the view of satellite infrared sensors, on which subseasonal SST observations have traditionally relied. Nearly free of cloud interference, the TMI has improved the spatiotemporal sampling of SST observations dramatically over the cloudy, tropical Indian Ocean.) The anomalies are nearly zonally uniform, occasionally exceed 3°C over a large area, and peak during December–March (Figure 9b) when the Intertropical Convergence Zone (ITCZ) is located at its southernmost position over the 5–10°S thermocline ridge and the mean winds are westerly (Figures 1 and 2).

They are accompanied by increased atmospheric convective activity and westerly wind anomalies (Figure 9a), both forcings reducing SST over the shallow thermocline.

[45] Recent observations using Argo floats reveal large variability in the mixed layer depth, which is negatively correlated with intraseasonal SST anomalies over the tropical South IO (W. Yu, personal communication, 2007). While one ocean model study indicates that ocean upwelling and entrainment play important roles in SST variability (G. A. Vecchi, personal communication, 2006), the ocean GCM study of Duvel et al. [2004] suggests that solar radiation and latent heat flux variability contributed about equally to the intraseasonal cooling events in 1999 with entrainment and advection being of secondary importance. While it is plausible that horizontal advection is small because background SST gradients are weak during December–March on and south of the equator in the tropical IO, the role of entrainment needs clarification.

3.2.2. Ocean-to-Atmosphere Feedback

[46] The fact that atmospheric anomalies lead SST anomalies in the 5–10°S band suggests the importance of

atmospheric forcing. Is there any indication that the large SST anomalies feed back onto the atmospheric MJO? The power spectrum of outgoing longwave radiation suggests the existence of two modes of variability: the MJO mode centered on the equator with a period of 30–50 days and a “southern mode” with largest power between 10°S and the equator and periods longer than 50 days (Figure 9c). Noting that the southern mode displays higher coherence with SST in the tropical South IO, *Saji et al.* [2006b] hypothesized that oceanic interactions may have lengthened the time scale of the southern mode and displaced it southward where the thermocline is shallow and SST variability is large. More research with coupled models is necessary to clarify the mechanisms that drive intraseasonal SST variability in the 5–10°S band and its role in modulating the atmospheric MJO.

3.3. Summertime ISOs

3.3.1. Properties

3.3.1.1. Atmosphere

[47] During boreal summer (June–September), precipitation anomalies associated with MJOs often exhibit northward propagation, with convection splitting from the MJO convection in the eastern IO to enter the Bay of Bengal [e.g., *Lawrence and Webster*, 2002, Figure 8]. These northward propagating ISOs are extremely important climatically, as they bring about active and break rainfall cycles of the Indian summer monsoon; these cycles last from a week to a month and are strong enough to impact the overall seasonal rainfall [*Yasunari*, 1980; *Lawrence and Webster*, 2002; *Annamalai and Sperber*, 2005].

3.3.1.2. Ocean

[48] Recent observations by moored buoys and the TMI sensor on the TRMM satellite have revealed large SST variations in the Bay of Bengal associated with northward propagating ISOs, with a peak-to-trough range of 2°C or more [*Sengupta et al.*, 2001; *Vecchi and Harrison*, 2002; *Roxy and Tanimoto*, 2007]. The heavy precipitation generates a thin barrier layer (section 2.5.2 [*Bhat et al.*, 2001; *Webster et al.*, 2002]), which strengthens SST variations forced by the surface heat fluxes. As for the MJOs, SST leads convection by 90° for northward propagating ISOs, with positive SST anomalies displaced north of the convection. Using an ocean GCM, *Schiller and Godfrey* [2003] found that surface heat fluxes, latent heat and radiative fluxes in particular, dominate the mixed layer heat budget on intraseasonal time scales over the summer Indian Ocean, with entrainment being locally important over the western Bay of Bengal.

3.3.2. Dynamics

[49] As for MJOs, northward propagating ISOs appear to be an intrinsic atmospheric phenomenon in that they can be simulated in stand-alone atmospheric GCMs, and a number of atmospheric mechanisms have been proposed for their existence [e.g., *Webster*, 1983; *Goswami and Shukla*, 1984; *Wang and Xie*, 1997]. *Jiang et al.* [2004] recently suggested that northward propagating ISOs are an unstable mode caused by summertime vortex tilting due to easterly vertical

shear of the background winds. At the same time, the close linkage between SST and convection in northward propagating ISOs suggests the possible influence of coupled processes, and several modeling studies support this idea. For example, *Fu et al.* [2003] compared simulations from both coupled and stand-alone atmospheric GCMs, reporting a decrease in the spectral power of northward propagating ISOs by as much as a factor of two in the latter (Figure 10). *Zheng et al.* [2004] reported a similar enhancement of summertime ISOs in their comparison of solutions to coupled and stand-alone GCMs.

[50] The coupling involves the following processes: Northward propagating ISOs are associated with a low-level cyclonic circulation. North of the convection, then, anomalous easterlies weaken the prevailing westerlies of the southwest monsoon, reducing surface evaporation and warming SST. Conversely, anomalous westerlies cool the SST south of it. The northward displaced positive SST anomalies create a tendency for the SST-convection couplet to propagate northward [*Vecchi and Harrison*, 2002]. This poleward propagation is characteristic of a coupled mode undergoing WES feedback in the presence of mean westerly winds [*Xie*, 1999] (see the discussion of equation (2)). In addition, the lack of clouds north of the disturbance helps to amplify the positive SST anomalies there.

3.3.3. South China Sea

[51] Northward propagating ISOs are not only confined to the Bay of Bengal but are also found over the South China Sea, as part of a northwest tilted planetary-scale banded structure in precipitation (Figure 8b) [*Lawrence and Webster*, 2002; *Fu et al.*, 2003]. TMI observations reveal a strong amplification of ISO-related SST anomalies there, with a peak-to-trough range of up to 3°C [*Xie et al.*, 2007], a consequence of wind-induced upwelling on and east of the east coast of Vietnam. In ISOs, atmospheric convection generally leads SST by 90°, but over the South China Sea, the ISO/SST and rainfall anomalies are nearly in phase, suggestive of a feedback for SST to reinforce local convective anomalies. Indeed, ISO variances in precipitation, surface wind, and SST all reach a local maximum over the South China Sea [e.g., *Duvel and Vialard*, 2007].

3.4. Oceanic Intraseasonal Variability

3.4.1. Current and Sea Surface Height Variability

[52] In addition to SST variability associated with ISOs, the tropical IO also exhibits pronounced intraseasonal variability in current velocity and sea surface height (SSH) fields. Early observational and modeling studies indicated that oceanic intraseasonal variability in the western IO is mostly caused by instabilities of the Somali Current as it crosses the equator (SMC01), and more recently, instability of the Great Whirl was diagnosed [*Brandt et al.*, 2003]. Over the past decade, observations farther east have shown that a large amount is also directly wind driven. For example, buoy observations in the eastern equatorial IO show spectral peaks at 30–60 days and 2 weeks for zonal and meridional velocities, respectively [e.g., *Sengupta et al.*, 2001, 2007; *Masumoto et al.*, 2005], the former likely driven by MJOs

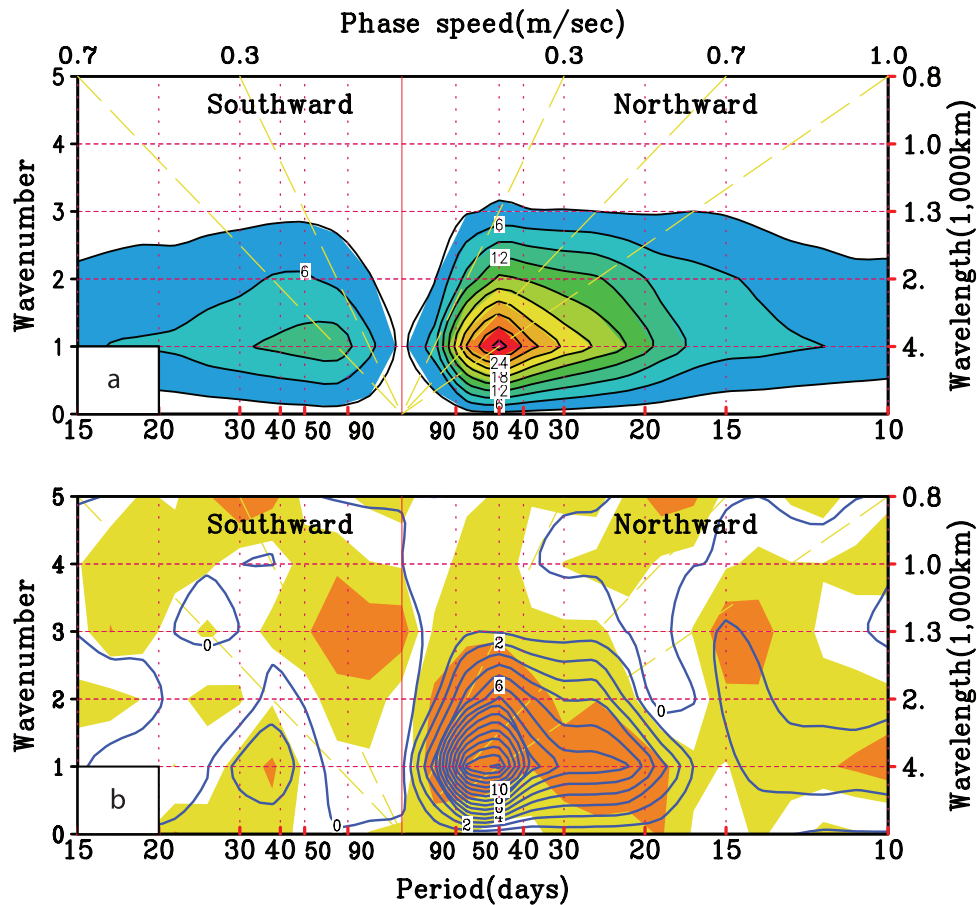


Figure 10. Wave number–frequency spectrum (a) from the coupled run and (b) the difference between the coupled run and the stand-alone atmospheric run. The contour intervals are 3 and 1 $(\text{mm/d})^2$, respectively. Yellow (orange) shaded areas in Figure 10b represent the significance larger than 75% (95%) [from *Fu et al.*, 2003].

and the latter likely driven by atmospheric biweekly variability [*Fukutomi and Yasunari*, 2005]. Figure 11 shows the difference in zonal velocity variance (meridional is similar) between a model simulation driven by daily winds and a reference run driven by smoothly varying seasonal climatology, confirming the large contributions of directly wind-forced ISO variability, particularly in the central and eastern tropical IO.

3.4.2. Biweekly Variability

[53] The spectral peak of the near-surface equatorial meridional velocity field is remarkably sharp and strong in the biweekly band (10–20 days). *Sengupta et al.* [2001] first identified this variability to be wind-forced Yanai waves using a numerical model: Observations of biweekly meridional velocity were well simulated in a solution forced by daily winds, whereas they were absent in a solution forced by climatological winds. At the same time, oceanic biweekly variability has a much sharper spectral peak than the winds that force it, pointing toward the importance of oceanic processes. Because atmospheric biweekly variability propagates westward, *Sengupta et al.* [2001, 2004] hypothesized that the sharper oceanic peak resulted from resonance. *Miyama et al.* [2006] used a hierarchy of ocean models to study the dynamics of biweekly variability in

detail, providing a precise definition of the resonance based on the propagation properties of Yanai waves and also noting the importance of remote forcing, vertical mixing, and vertical propagation in sharpening the oceanic response.

3.4.3. Ninety-Day Variability

[54] *Han* [2005] reported a prominent spectral peak with a period of 90 days in sea level data. On the basis of solutions to a hierarchy of models, she suggested that the peak resulted from the resonant response of an IO basin mode to wind forcing: The basin size and stratification of the IO are such that resonant modes may be excited at 90 and 180 days [*Jensen*, 1993; *Han et al.*, 1999; *Yuan and Han*, 2006]. The 180-day resonance is generated by the strong semiannual winds in the tropical IO. Regarding the 90-day peak, the resonance is rather broad and cannot in itself explain the peak's sharpness; it is likely, then, that it is forced by weak 90-day component in the climatological winds, with the ocean's response to this narrowband forcing amplified by the broad resonance.

3.4.4. Variability off Java and Sumatra

[55] Intraseasonal variability of SSH and mixed layer depth is also very active off Sumatra and Java. *Potemra et al.* [2002] and *Wijffels and Meyers* [2004] identified intraseasonal Kelvin waves forced by zonal wind anomalies

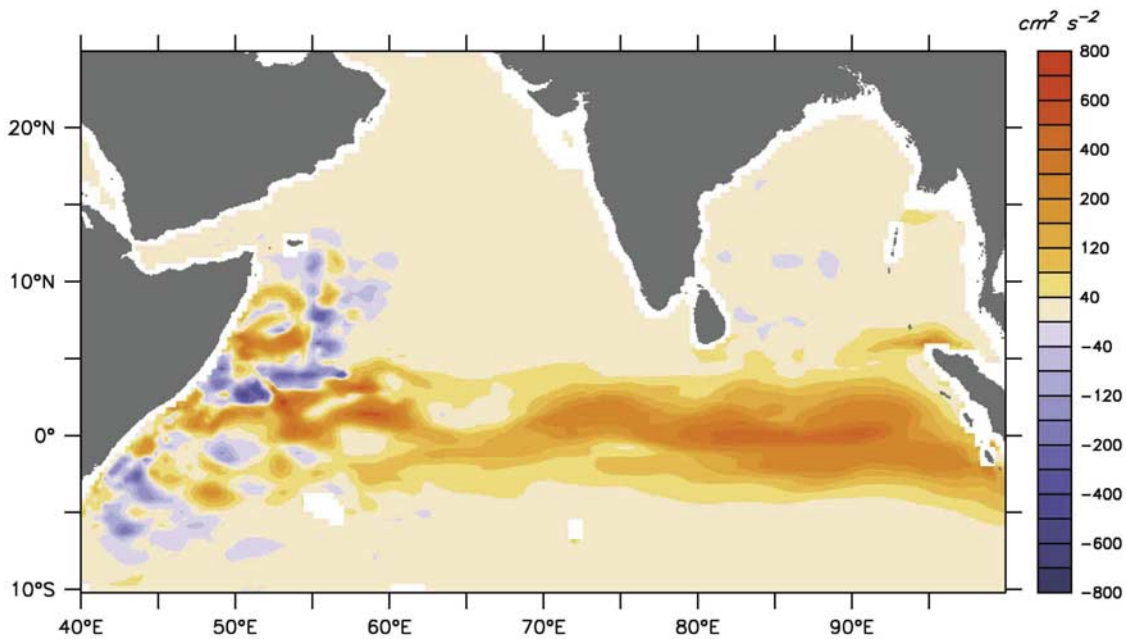


Figure 11. Difference in zonal velocity variance ($\text{cm}^2 \text{s}^{-2}$) between a model run driven by diurnal winds and a run driven by smooth seasonal climatology [from *Sengupta et al.*, 2001].

along the equator as the source of SSH variability along the IO eastern boundary and into the ITF passages. *Iskandar et al.* [2005] investigated these relations further, finding two bands of SSH variability off Sumatra and Java: 20–40 days during boreal summer and 60–90 days during boreal winter. They also reported seasonal differences in their generation mechanisms. In boreal summer, remote forcing by equatorial winds is the main source of the shorter-period variance, whereas local forcing contributes about equally to remote forcing to the longer-period wintertime fluctuations. On the basis of a modeling study, *Iskandar et al.* [2006] concluded that the longer-period signals were forced mostly by MJOs at ~60 days and by equatorial winds at 90 days.

3.4.5. Climate Impacts

[56] Aside from its potential importance on MJOs and northward propagating ISOs, the impact of oceanic intraseasonal variability on climate is not known. It is known, however, that oceanic intraseasonal variability can rectify to impact mean flows [*Waliser et al.*, 2003; *Han et al.*, 2004] and to generate interannual variability. For example, the “Great Whirl” (Figure 3) exhibits large interannual variability. *Brandt et al.* [2003] showed from observational analysis that it generates instabilities in the period range of 30–50 days that subsequently develop into free Rossby waves. *Wirth et al.* [2002] analyzed a solution to a high-resolution regional model of the Arabian Sea driven by

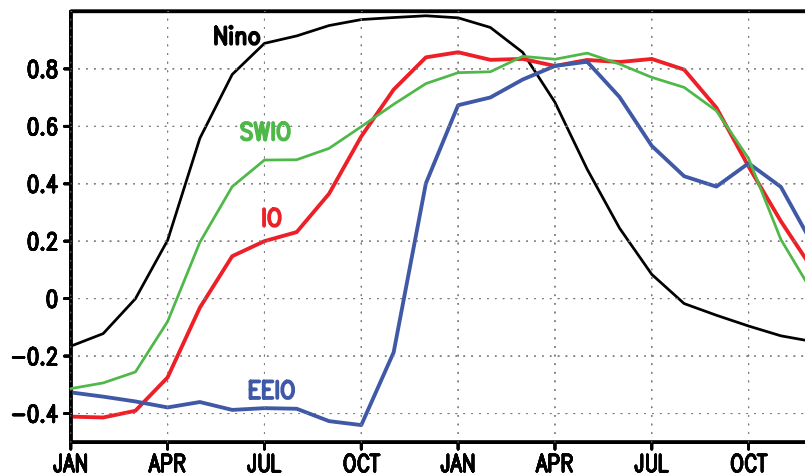


Figure 12. November (year 0)–January (year 1) Niño3 SST correlation with SST averaged in the eastern equatorial Pacific (160–120°W, 5°S–5°N; black), the tropical IO (40–100°E, 20°S–20°N; red), the southwest IO (50–70°E, 15–5°S; green), and the eastern equatorial IO (90–110°E, 10°S–equator; blue). The HadSST data set [*Rayner et al.*, 2006] for the 57-year period of 1950–2006 is used.

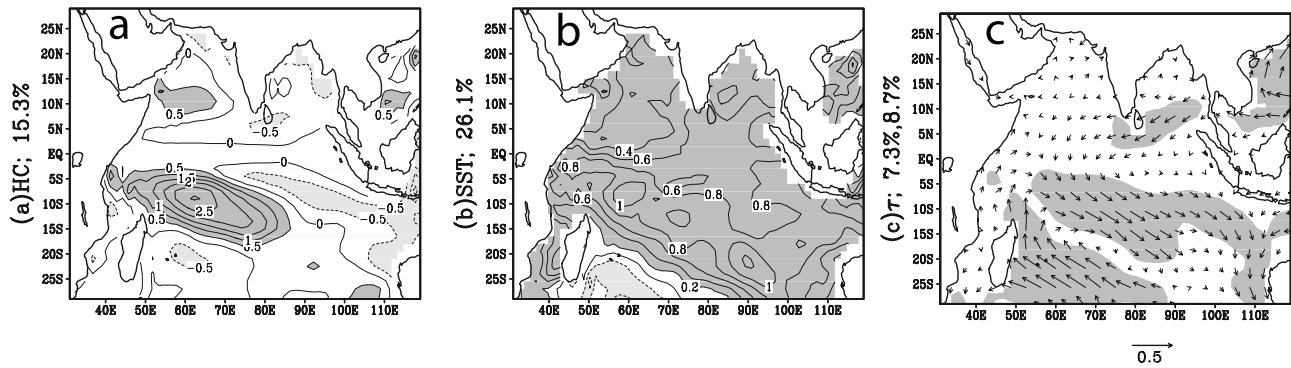


Figure 13. The spatial structures of the first combined empirical orthogonal function mode for (a) upper ocean heat content (HC in °C), (b) SST (°C), and (c) wind stress (dyn/cm²) for spring (March, April, and May) data. The shading in Figure 13c shows the regions of wind stress magnitude larger than 0.1 dyn/cm² [from *Huang and Kinter, 2002*].

climatological winds and also found large interannual variability of the Great Whirl, attributing it to instabilities. In a recent model study for the entire IO north of 23°S, *Jochum and Murtugudde [2005]* evaluated the eddy kinetic energy of a model driven by a mean seasonal wind stress cycle. They confirmed the western IO to be a source of instabilities that leads to interannual variability; moreover, they found the entire subtropical ocean in the 10–20°S band to be a region of large interannual SST variability caused by instabilities.

4. INTERANNUAL VARIABILITY

[57] Two prominent modes of interannual variability impact the IO, namely, ENSO and the IOD. Here we first review influences of ENSO in the IO (section 4.1), followed by an

overview of IOD history, basic properties, and generation mechanisms (section 4.2). Next, we note two other examples of interannual variability, namely, the Tropical Biennial Oscillation and subtropical dipole (section 4.3). Then, we report on the impacts of ENSO- and IOD-induced IO SST anomalies on regional and remote climate (section 4.4). We conclude with a discussion of recent efforts to predict IO SST (section 4.5).

4.1. ENSO

[58] ENSO is the dominant mode of natural climate variability in the instrumental record. It is characterized by recurrent warming and cooling of the eastern equatorial Pacific (El Niño) and changes in the zonal pressure gradient over the western equatorial Pacific (the Southern Oscillation) and is phase locked to the annual cycle, with eastern

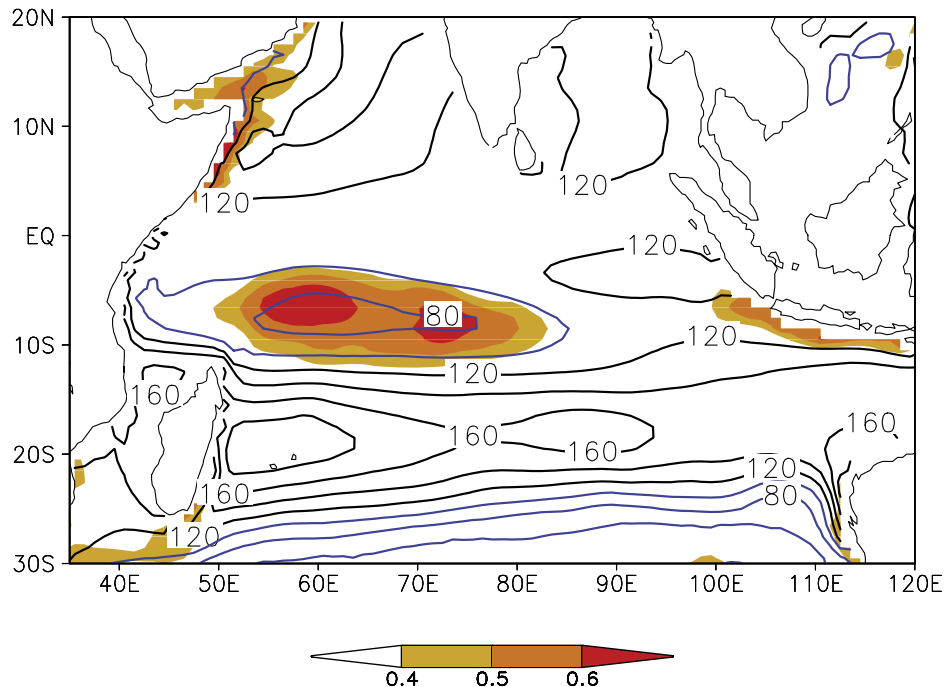


Figure 14. Annual mean depth of the 20°C isotherm (contours in m) and correlation of its interannual anomalies with local SST (color shades) [from *Xie et al., 2002*].

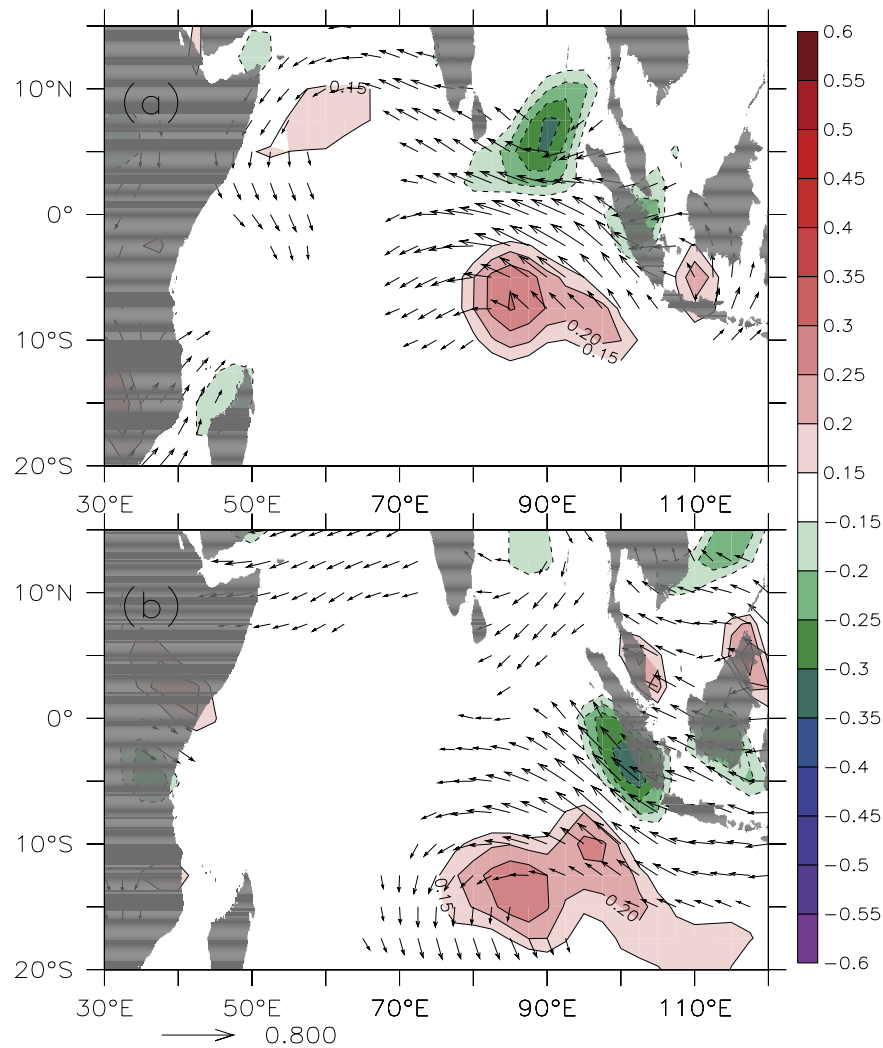


Figure 15. (a) Partial correlation of 1000 hPa winds (vectors) and wind curl (colors) with Indian Ocean Dipole (IOD) index. (b) As Figure 15a but for Niño-3 index. Only correlations significant at 99% level are shown [from Yu et al., 2005].

Pacific SST anomalies developing during boreal summer, peaking in winter, and decaying in the following spring (Figure 12). Bjerknes positive feedback (section 2.5.1) is a key part of its generation; see Philander [1990], McCreary and Anderson [1991], Neelin et al. [1998], and Wang and Picaut [2004] for discussions of ENSO dynamics.

[59] During El Niño, atmospheric convection shifts eastward and intensifies over the central-to-eastern equatorial Pacific, resulting in slow anomalous subsidence over the western Pacific and maritime continent. This large-scale shift in convection alters atmospheric circulation remotely in both the tropics and extratropics via atmospheric wave adjustments often referred to as an “atmospheric bridge” [Alexander et al., 2002; Liu and Alexander, 2007]. In this section, we describe the IO’s response to this remote forcing by ENSO.

4.1.1. IO Basin-Wide Warming

[60] The tropical IO gradually warms during an ENSO year, reaching a maximum during spring (March–May; Figure 13) about one season after NINO3 SST has peaked (Figure 12) [Nigam and Shen, 1993; Klein et al., 1999; Liu

and Alexander, 2007]. This SST response is so robust that it was even captured in earlier analyses of sparse ship observations. In the empirical orthogonal function analysis of Weare [1979], the first mode represents a basin-wide warming over the tropical IO that lags slightly behind El Niño warming over the Pacific. The composite analysis of Cadet [1985] referenced to the Southern Oscillation index reproduces this spatially uniform warming pattern over the IO. Klein et al. [1999] showed that much of this warming is caused by ENSO-induced surface changes in surface heat fluxes, particularly the wind-induced latent heat and cloud-induced solar radiation fluxes. During El Niño, atmospheric convection is suppressed over the IO, and the resultant increase in solar radiation contributes to the IO warming.

[61] During El Niño, tropospheric temperature increases over the entire tropics [Yulaeva and Wallace, 1994; Sobel et al., 2002]. Chiang and Sobel [2002] suggested that this tropospheric warming may directly raise temperature and humidity in the atmospheric boundary layer over regions of deep convection. There is observational and modeling evidence in support of this mechanism over the tropical

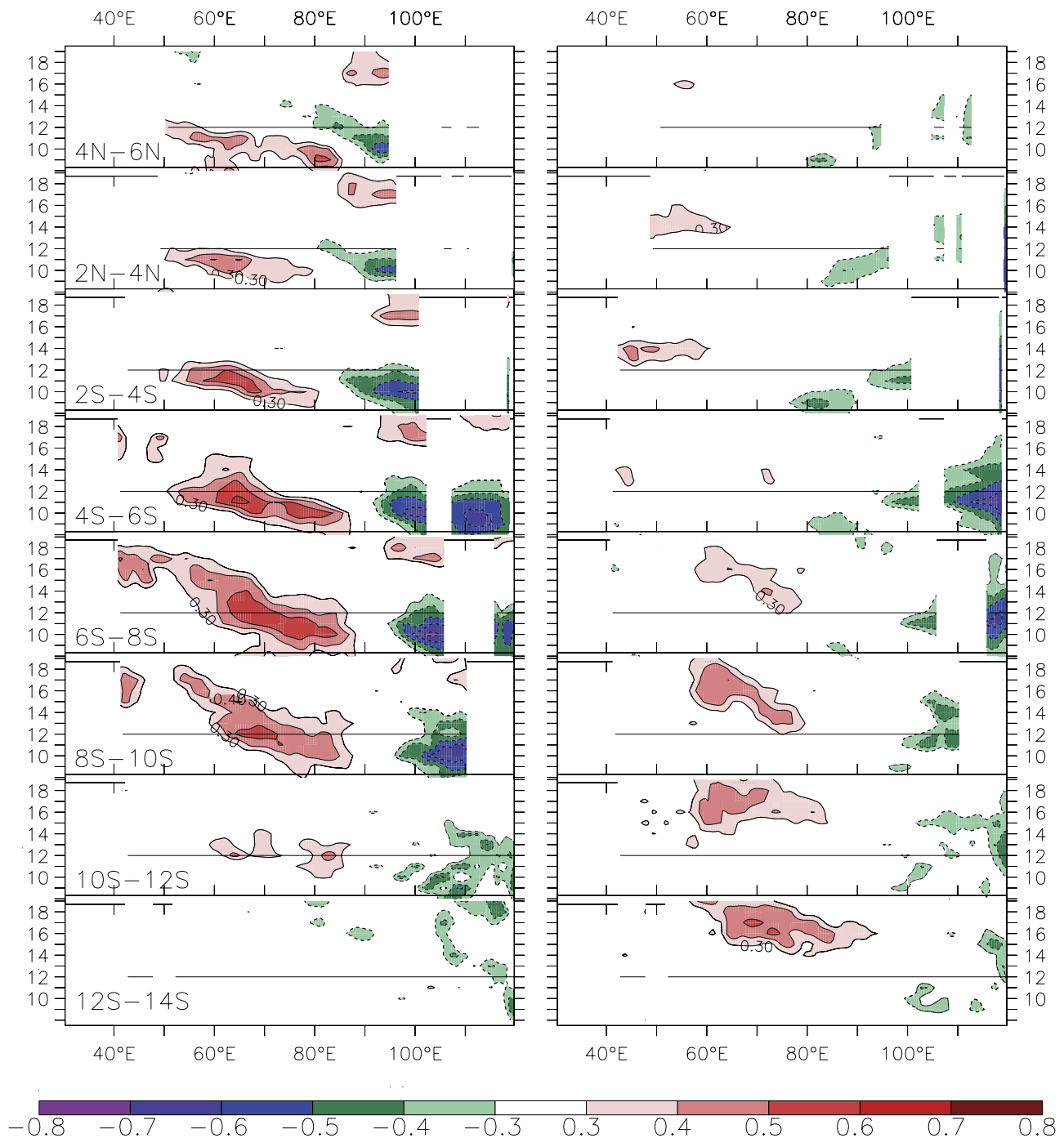


Figure 16. Lead/lag partial correlation for sea surface height anomalies for (left) September, October, and November (SON)–IOD and (right) October, November, and December (OND)–Niño-3, determined from output fields of the SODA assimilation model for latitude belts as function of calendar month and longitude. Only correlations significant at 95% level are shown [from Yu *et al.*, 2005].

North Atlantic [Saravanan and Chang, 2000; Chikamoto and Tanimoto, 2005], but further studies are necessary to corroborate its effect on the IO [Chiang and Lintner, 2005].

4.1.2. SWIO Warming

[62] While El Niño–induced warming covers the entire tropical IO, the cause of the warming in the tropical SWIO is different from that in the rest of the basin. Specifically, Klein *et al.* [1999] noted that the SWIO warming cannot be explained by surface fluxes. Indeed,

atmospheric GCMs forced by observed SST in the tropical Pacific and coupled to a slab mixed layer ocean elsewhere fail to reproduce the warming [Alexander *et al.*, 2002; Lau and Nath, 2003], pointing toward the importance of ocean dynamics (section 2.5.1).

[63] Recall that there is a thermocline ridge from 5 to 10°S in the SWIO, where cool isotherms lie near the surface (Figure 1; section 2.1). There, thermocline variability strongly influences SST as manifested in their high corre-

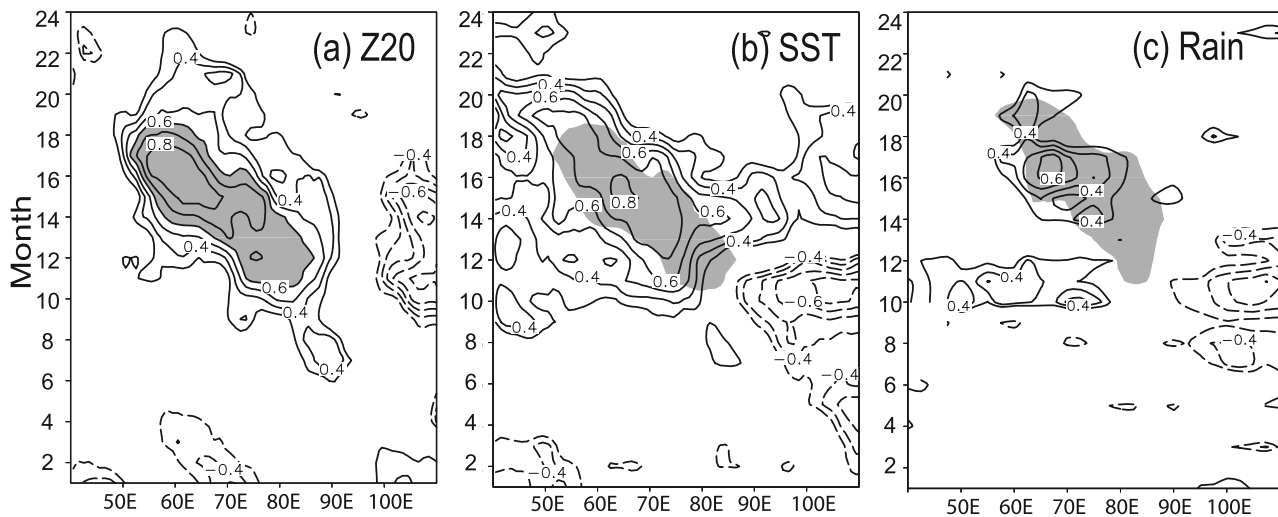


Figure 17. Correlation with eastern Pacific SST during October–December (months 10–12) as a function of longitude and calendar month: (a) Z20, (b) SST, and (c) precipitation averaged from 12 to 8°S. Shading denotes where correlation exceeds 0.6 with Z20 in Figures 17a and 17b and with SST in Figure 17c [from Xie et al., 2002].

lation (Figure 14). Toward the mature phase of El Niño (December), a region of anomalous anticyclonic wind stress curl forms in the tropical southeast IO (Figure 15b), caused by an atmospheric bridge from the Pacific, an anomaly of the Walker Circulation. It forces downwelling Rossby waves in the southeast IO (Figure 16, right) [Perigaud and Delecluse, 1993; Masumoto and Meyers, 1998; Chambers et al., 1999], which, after they arrive in the SWIO several months later, deepen the thermocline ridge and warm SST there [Xie et al., 2002]. Thus, the SWIO SST anomalies are largely determined by remotely forced changes in the depth of the ridge, a result supported by ocean model studies [Murtugudde and Busalacchi, 1999; Murtugudde et al., 2000; Behera et al., 2000].

[64] Figure 17 shows correlations of SWIO thermocline depth, SST, and precipitation anomalies with an ENSO index. The influence of the thermocline depth on SST is large, as manifested by their high cross correlation; indeed, interannual SST forms a local maximum over the ridge during April–July, with a standard deviation of 0.4°–0.5°C. Moreover, embedded in a basin-wide warming that peaks in February–April following El Niño, SST anomalies display a positive core that copropagates westward with the Rossby waves (Figures 17a and 17b) [Xie et al., 2002; Huang and Kinter, 2002; Jury and Huang, 2004; Baquero-Bernal and Latif, 2005].

[65] The ITCZ is displaced south of the equator during boreal winter, covering the 5–10°S thermocline ridge (Figures 1 and 2). Not surprisingly, then, the SWIO warming also increases atmospheric convection in the region (Figure 17c), with significant impacts on both local and remote climate (section 4.4.1).

4.1.3. Eastern Equatorial IO Warming

[66] In contrast to the warming elsewhere, warming in the eastern equatorial IO (EEIO) is more abrupt, taking place during October–March only after an earlier cooling episode

(Figure 12). IOD events often co-occur with El Niño, cooling the EEIO from July to November (section 4.2.2). Even without an IOD, though, EEIO SST anomalies cool during the growing El Niño (July–October) in response to intensified southeasterlies off Java and Sumatra, which are associated with an anomalous high-pressure system that is part of the Southern Oscillation (Figure 15b) [Wallace et al., 1998; Wang et al., 2003]. The strengthened southeasterlies increase surface evaporation, vertical mixing in the ocean, and coastal upwelling [Shinoda et al., 2004], cooling the southeast IO and suppressing atmospheric convection there. The southeasterlies weaken after October, and the resulting decreases in coastal upwelling [Murtugudde et al., 2000] and evaporation, as well as the increased solar radiation due to suppressed convective clouds, cause EEIO SST anomalies to switch from negative to positive [Tokinaga and Tanimoto, 2004]. In response to the anomalous equatorial easterlies, the thermocline shoals in the EEIO, thinning the mixed layer and, hence, intensifying the warming.

4.1.4. Asymmetrical Pattern During Boreal Spring

[67] The tropical IO warming often displays significant distributions in space. The North IO warming weakens as El Niño decays during boreal spring. Kawamura et al. [2001] show that the southward SST gradients anchor an antisymmetrical pattern of atmospheric anomalies during spring, with northeasterly and southwesterly wind anomalies north and south of the equator, respectively. They suggest that this antisymmetrical pattern is due to the WES feedback operating on the easterly climatological winds that prevail during boreal winter/early spring. Indeed, this antisymmetrical pattern emerges as the leading mode of March–May precipitation variability over the tropical IO from the empirical orthogonal function (EOF) analysis of Wu et al. [2008]. It features increased (decreased) rainfall south (north) of the equator and is associated with a southward increase of SST warming across the equator.

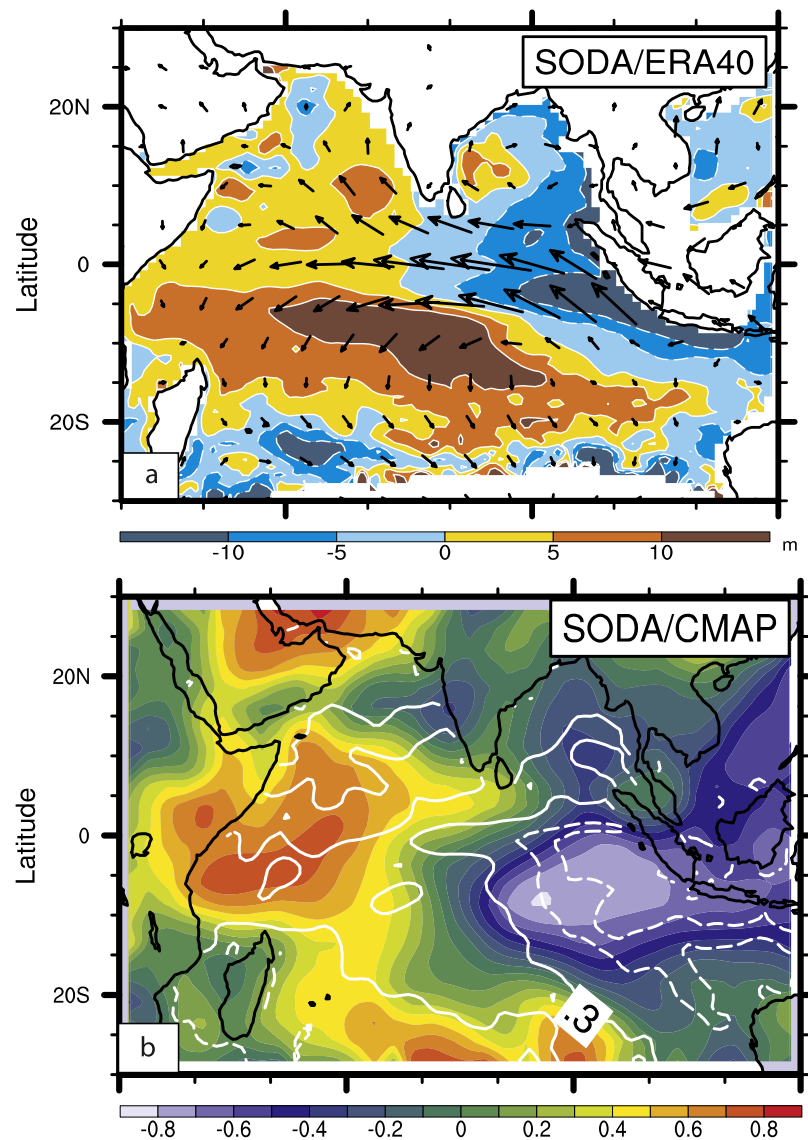


Figure 18. IOD pattern during September–November. (a) Regression of 20°C isotherm depth (Z20; shades in m) and surface wind velocity (m/s) upon the first principal component of Z20 and (b) correlation of precipitation (shades) and SST (contoured at 0.3, 0.6, and 0.9 with zero omitted and negative dashed) with the first principal component of Z20 [from Saji et al., 2006a].

Both reduced surface evaporation and the downwelling Rossby wave are probably important to maintain the southern warming.

[68] The antisymmetric wind pattern tends to occur at the decay phase of El Niño. The northeasterly anomalies, superimposed on the northeast monsoon, weaken the North IO warming during boreal winter and early spring by intensifying surface evaporation. The antisymmetric wind pattern persists through early summer, anchored by the SWIO warming. The same northeasterly wind anomalies north of the equator turn into a warming mechanism after the onset of the southwest monsoon, causing a pronounced peak in SST anomalies over the North Indian Ocean and South China Sea [Du et al., 2009].

4.1.5. Models

[69] The basin-wide warming following El Niño is simulated in most coupled GCMs with a lag of 2–4 months

[Venzke et al., 2000], except in models where El Niño is weak or peaks in the wrong season [Saji et al., 2006a]. Many of the 15 models Saji et al. [2006a] examined have successfully simulated the ENSO-forced Rossby waves, which increase the persistence of SST anomalies over the SWIO. For example, Huang and Shukla [2007] reported that in their coupled model forced with observed SST in the tropical Pacific, ENSO-forced Rossby waves exert a discernible influence on SST and the atmosphere as late as June–August in the year after ENSO peaks.

[70] Nevertheless, modeling SST anomalies that copropagate with ocean Rossby waves in the SWIO and their atmospheric effects remains a challenge. Few models capture the westward propagating SST anomalies [Saji et al., 2006a]. This deficiency may result from the models' poor simulation of ENSO, atmospheric teleconnections from the Pacific into the IO, or the SWIO thermocline ridge.

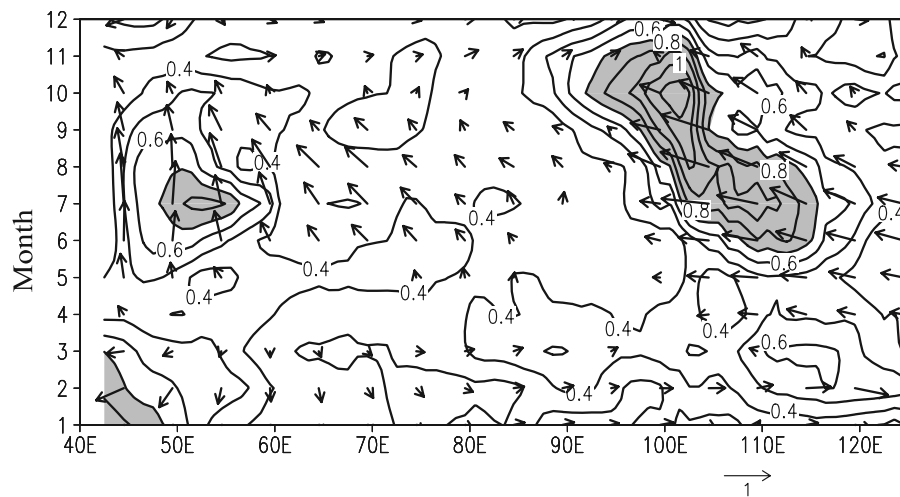


Figure 19. Distance-time section of climatological wind stress vectors (N/m^2) and root-mean-square interannual variance of SST (contours; shade $> 0.7^\circ\text{C}$) along the equator and the Indonesia coast (east of 97°E). Along Indonesia, the alongshore (across-shore) wind component is given by the horizontal (vertical) component of the vector [from Xie *et al.*, 2002].

4.1.6. Effect on the ITF

[71] On the basis of repeat XBT sections across the upper 400 m of the throughflow regime during the 1970s to early 1990s it has been reported that the ITF was higher during La Niñas than during El Niños [Meyers, 1996]. On the other hand, on the basis of the SODA reanalysis covering the time period 1958–2001, England and Huang [2005] determined a rather low correlation between an ENSO index and total ITF, with the ITF reduction lagging El Niño by 8 months. More recently, Potemra and Schneider [2007] determined from both SODA reanalysis and a coupled model solution that the reason for the overall low ITF-ENSO coherence was baroclinicity of the ITF transport variability: Transports in the upper 100 m were mainly caused by interannual alongshore winds off Sumatra-Java, whereas from 100 to 500 m they were mostly driven by divergent winds between the equatorial IO and Pacific Ocean.

4.2. IOD Events

[72] As noted above, the easterly trade winds that prevail over the equatorial Pacific and Atlantic oceans favor Bjerknes feedback, by shoaling the thermocline in the eastern equatorial ocean and, hence, allowing the upwelling of cool subsurface water (section 2.5.1). In contrast, the annual mean winds over the equatorial IO are weak and westerly, the thermocline is flat, and there is little or no upwelling in the EEIO, suggesting that Bjerknes feedback is not active there. In fact, because of the strong seasonal variability of the monsoon winds, conditions are favorable for Bjerknes feedback during the summer and fall, sometimes leading to the development of La Niña-like ocean-atmospheric anomalies, namely, IOD events (Figure 18).

4.2.1. History

[73] There has been considerable discussion of the air-sea interaction associated with IOD events in the literature. Analyzing sparse ship-based surface meteorological observations for 1954–1976, Reverdin *et al.* [1986] reported that

an east-west dipole of cloudiness sometimes develops in the tropical IO during October–November, together with zonal wind anomalies in the central ocean. Noting further that cool SST and negative cloudiness anomalies co-occur in the EEIO, they suggested that the cooling suppresses atmospheric convection, driving easterly anomalies along the equator as in the Gill [1982] model. Drawing an analogy to ENSO, they speculated further that the easterlies strengthen EEIO cooling by shoaling the thermocline there, as in Bjerknes feedback. Using longer data sets, Hastenrath *et al.* [1993] showed that high correlations exist among the zonal gradients of SST and atmospheric pressure, the equatorial zonal wind, and East African rainfall. On the basis of XBT observations, Meyers [1996] reported strong coupling between the shoaling thermocline and SST cooling off the south coast of Java in 1994, both phenomena later shown to be part of a major IOD event [Vinayachandran *et al.*, 1999; Behera *et al.*, 1999]. In solutions to an ocean model, Murtugudde and Busalacchi [1999] demonstrated a strong correlation between thermocline depth and SST off the Java coast during 1980–1995.

[74] Despite these prior findings, it was not until the dramatic development of an equatorial cold tongue during the major 1997 IOD event that the climate community began to recognize the IOD to be a distinct coupled ocean-atmosphere phenomenon [Webster *et al.*, 1999; Yu and Rienecker, 1999; Murtugudde *et al.*, 2000]. On the basis of a synthesis of 40 years of observations, Saji *et al.* [1999] clearly illustrated the remarkable covariability of near-equatorial SST, atmospheric convection, and winds during IOD events, providing strong support for Bjerknes feedback as a key process.

4.2.2. Properties

4.2.2.1. Observations

[75] IOD events develop in June and peak in October [Saji *et al.*, 1999], a seasonality that itself suggests the

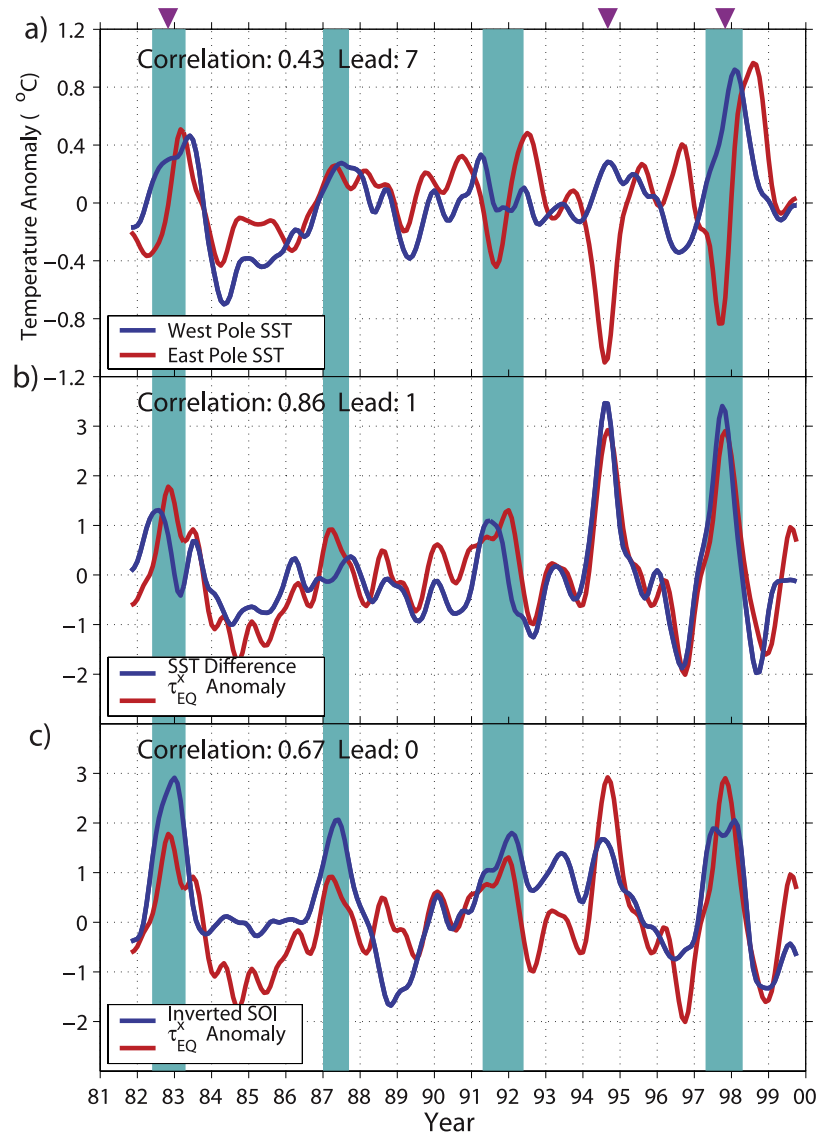


Figure 20. (a) SST anomalies 1981–1999 in western (blue) and eastern (red) IO, (b) west-east SST difference (blue) and zonal equatorial wind stress in central IO (red), and (c) zonal wind stress from Figure 20b with inverted SOI. Light blue shading indicates occurrence of El Niño events in the Pacific (reprinted from *Feng and Meyers* [2003], copyright 2003, with permission from Elsevier).

influence of ocean dynamics. The climatological winds are southeasterly off the Sumatra coast from April through October, reaching a peak during the summer at which time the winds have an easterly component all along the equator (Figure 19). This forcing favors a shallow thermocline and upwelling in the EEIO, offering a seasonal window for the development of Bjerknes feedback and the IOD. Indeed, major SST variance off the Indonesian coast is confined to this upwelling season (Figure 19) [*Susanto et al.*, 2001; *Xie et al.*, 2002]. Shortly thereafter, the intense monsoonal forcing weakens the southeasterly winds off Sumatra, closing the window and leading to the rapid termination of IOD events [e.g., *Tokinaga and Tanimoto*, 2004].

[76] The typical IOD manifests itself through a zonal gradient of tropical SST, with cooling off Sumatra and warming in the western ocean (Figure 18) [*Saji et al.*, 1999; *Saji and Yamagata*, 2003]. As the IOD develops

(September–November), an east-west dipole of anomalous rainfall is established over the tropical IO, with precipitation increasing in the west because of the low-level convergence associated with the anomalous equatorial easterlies and vice versa in the east [*Saji et al.*, 1999; *Webster et al.*, 1999]. The rainfall dipole is an important element of the air-sea interaction (Bjerknes feedback) that sustains the IOD. Easterly wind anomalies blow from the cold/dry EEIO to the warm/rainy western IO, lifting the thermocline in the EEIO and amplifying SST cooling there (Figure 18).

[77] Similar to ENSO, downwelling Rossby waves are generated during IOD (Figure 16, left), both by off-equatorial anticyclones and by equatorial τ^x (Figure 15a). A comparison of IOD and ENSO wind anomalies (Figure 15) shows that the IOD southern anticyclone is shifted northward, the northern anticyclone is better formed, and equatorial τ^x is stronger. These differences are reflected in

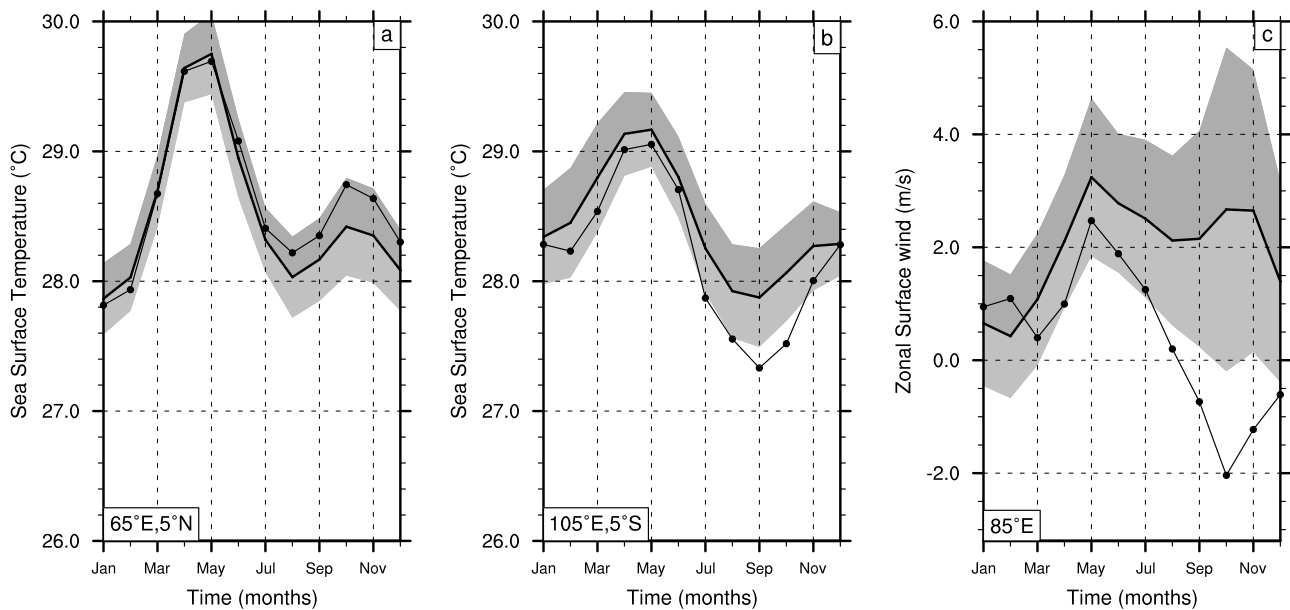


Figure 21. Seasonal cycles (heavy solid) with interannual variability (1 standard deviation, shaded) of SST and anomalies during IOD episodes (light solid) for (a) western IO and (b) eastern IO. (c) As Figures 21a and 21b but for zonal wind on equator at 85°E [from Saji and Yamagata, 2003].

the ocean's response, with IOD-forced (ENSO-forced) Rossby waves confined largely north (south) of 10°S (Figure 16) [Yu *et al.*, 2005; Rao and Behera, 2005]. In models without an interactive Pacific and hence ENSO, SWIO Rossby waves still exist, forced by IO wind variability [Baquero-Bernal and Latif, 2005]. The climatic importance of the IOD Rossby waves is not clear. They do not appear to provide delayed negative feedback to terminate IOD events, as similar waves do for ENSO. On the other hand, they have been hypothesized to provide such feedback for the generation of the Tropical Biennial Oscillation (section 4.3).

[78] Large sea level anomalies are also associated with IOD events. Using satellite altimetry, Palastanga *et al.* [2006] analyzed the resulting geostrophic anomalies of the subtropical gyre and western circulation branches. For positive IOD episodes, such as 1994 and 1997, they reported a northward extension of the subtropical gyre and a retreat of the tropical gyre, associated with a weakening of the western SEC and its extensions, namely, the NEMC, SEMC, and EACC (Figure 3). For negative IOD events, such as in 1996 and 1998, the opposite changes occurred. In the Mozambique Channel, stronger (weaker) southward flow and eddy activity occurred for positive (negative) IOD episodes. As the cause of these SWIO circulation anomalies, Palastanga *et al.* [2006] suggested a combination of remotely forced Rossby waves coming in from the east and forcing by wind stress curl anomalies east of Madagascar.

4.2.2.2. Models

[79] The identification of the IOD stimulated a flurry of model studies to simulate the phenomenon. Ocean models driven by IOD anomalies simulated the oceanic response well [e.g., Murtugudde *et al.*, 2000]. A number of coupled model studies have been able to simulate a mode of

variability very much like the IOD, with upwelling and strong cooling in the EEIO, weak warming and suppressed convection in the western equatorial ocean, and equatorial easterlies (Figure 18) [Iizuka *et al.*, 2000; Baquero-Bernal *et al.*, 2002; Yu *et al.*, 2002; Loschnigg *et al.*, 2003; Gualdi *et al.*, 2003; Lau and Nath, 2004; Fischer *et al.*, 2005; Spencer *et al.*, 2005; Behera *et al.*, 2006]. The EEIO cooling is generally most intense south of the equator off the Sumatra coast in the coupled models and displays a realistic seasonality with large variance during August to December [Saji *et al.*, 2006a]. The good agreement indicates that coastal/equatorial upwelling is a key to EEIO SST variability and the generation of IOD in the models and that the Bjerknes feedback is at work.

4.2.3. Generation

[80] Two issues concerning the generation mechanisms of IOD have been debated extensively. One is whether the IOD really is a dipole or is rather more accurately described as an eastern ocean “monopole.” The other is whether it is in fact an independent climatic mode or rather is simply an aspect of ENSO [e.g., Allan *et al.*, 2001; Yamagata *et al.*, 2004; Chang *et al.*, 2006].

4.2.3.1. Dipole Versus Monopole

[81] Figure 20a shows SST anomalies for the western and eastern IO during 1981–2000 [Feng and Meyers, 2003]. Not very often do the eastern and western SST curves show antiphase; indeed, the overall correlation between them is positive. Nevertheless, there is a tendency for the two poles to have opposite signs during IOD events. This paradox appears because of the IOD's strong seasonality: IOD events take place during June–November, whereas the basin-scale warming following an El Niño dominates during the rest of the year.

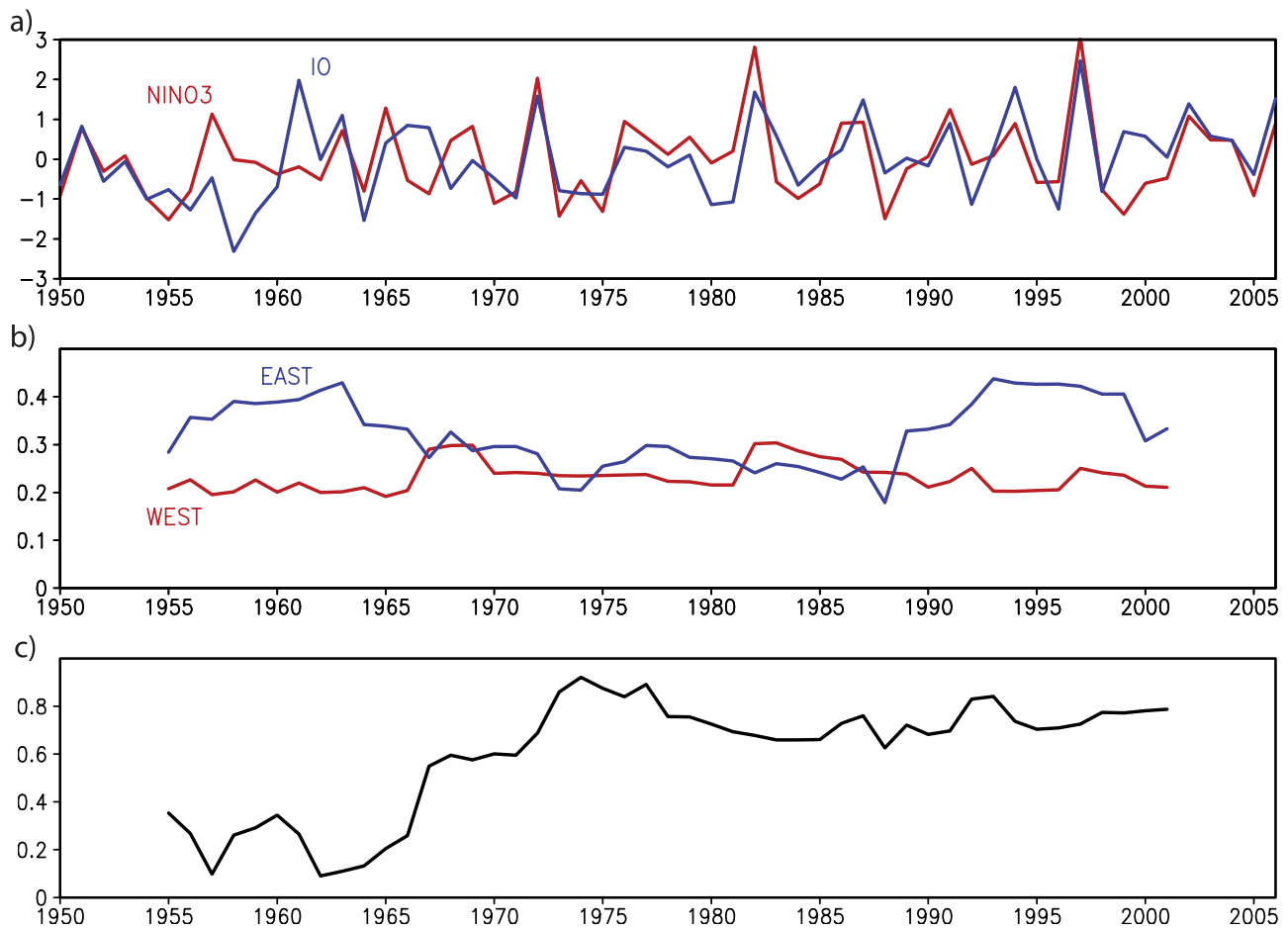


Figure 22. (a) Normalized time series of November–January SST averaged in the eastern equatorial Pacific (Niño-3.4 index, 160–120°W, 5°S–5°N; red) and the August–October IOD index (50–70°E, 10°S–10°N minus 90–110°E, 10°S–equator), based on the HadSST data set. The standard deviations are 1.06 and 0.42°C, respectively. (b) SST standard deviations (°C) in the western (red) and eastern (blue) boxes of the IOD index in 11-year sliding windows. (c) Correlation of the IOD and El Niño Southern Oscillation indices in 11-year sliding windows.

[82] Figures 21a and 21b show SST annual cycles from climatology (thick curves) and during IOD events (thin curves) in the western and eastern IO, respectively, and the western warming and eastern cooling after July is evident. On the other hand, SST variability associated with IOD events is weaker in the west than the east, the western SST anomalies lying within one standard deviation of the overall interannual variance (shading) and the eastern anomalies outside that range. Thus, although IOD events do exhibit an SST dipole, they are dominated by the eastern pole, for which ocean upwelling is an important process.

[83] The equatorial winds (a key measure of the IOD) are expected to respond to the equatorial temperature gradient, rather than to SST in an individual pole [Behera *et al.*, 2003]. (It is for this reason that some researchers prefer to refer to the IOD as the IO Zonal Mode.) Figure 20b shows curves for the equatorial zonal wind anomalies ($\Delta\tau_{eq}^x$) and the west-east SST difference along the equator (ΔT_{ew}), and the correlation between them is very high (0.86), considerably higher than for the western and eastern poles alone. A

comparison of Figures 20a and 20b shows that ΔT_{ew} is most often, but not always, determined by its eastern pole.

4.2.3.2. IOD Versus ENSO

[84] In support of the IOD being part of ENSO, IOD and El Niño episodes are significantly correlated (Figure 20c), particularly during the IOD mature phase (September–November); moreover, several recent IOD and ENSO events occurred simultaneously, most prominently in 1997 (Figures 20 and 22). Not all IOD events, however, co-occur with ENSO. For example, the strong IOD in 1994 occurred in a year with a very weak ENSO (Figure 22), and one of the largest IOD events on record happened in 1961, also a non-ENSO year. Analyzing observations from 1958 to 1997, Saji and Yamagata [2003] concluded that 11 out of the 19 episodes identified as moderate to strong IOD events occurred independently of ENSO. Similarly, Meyers *et al.* [2007] concluded that from 1876 to 1999, about half of the IOD events were independent from ENSO. Consistent with these results, the correlation between IO equatorial winds and an ENSO index (Figure 20c) is significantly less than

that between the winds and ΔT_{ew} (Figure 20b). In addition, Figure 21c plots the annual cycles of IO equatorial winds from climatology (thick curve) and during IOD (thin curve), and during the fall the latter lies well outside the range of total interannual variability (shading).

[85] A recent analysis of IO SST anomalies associated with ENSO and IOD events was carried out by *Nagura and Konda* [2007], on the basis of observed SST and National Centers for Environmental Prediction (NCEP) reanalysis. They found that IOD development depends on the seasonal switch from neutral or La Niña conditions in the Pacific to El Niño: IOD development is favored if this switch occurs from spring to summer; if La Niña conditions continue or El Niño does not develop until fall, an IOD event will not occur.

[86] Results from coupled models are mixed concerning the strength of the ENSO/IOD relationship. In many models, IOD tends to co-occur with El Niño [*Baquero-Bernal et al.*, 2002; *Yu and Lau*, 2004; *Loschnigg et al.*, 2003; *Lau and Nath*, 2004; *Fischer et al.*, 2005]. *Saji et al.* [2006a] examined the relationship in the 15 coupled models that participated in the Intergovernmental Panel on Climate Change (IPCC) Fourth Assessment Report (AR4). They reported that there is a large spread of simulated Z20 in the EEIO, ranging from 80 to 150 m as compared to the observed value of 110 m, and that the IOD–El Niño correlation tends to be high in solutions with a deeper thermocline off Sumatra. (The cause of this spread is unclear, but it likely results from differences in the parameterization of vertical mixing among the models.) *Saji et al.* [2006a] speculated that the Bjerknes feedback is stronger in models with a shallow Sumatra thermocline and that therefore IOD is more likely to occur independent of ENSO.

[87] In some models, the IOD becomes the dominant mode of climate variability when the Pacific Ocean is decoupled by prescribing the climatological SST there [*Baquero-Bernal et al.*, 2002; *Yu and Lau*, 2004; *Fischer et al.*, 2005; *Behera et al.*, 2006], and its spatial structure is largely unchanged compared to solutions with an interactive Pacific. In the *Fischer et al.* [2005] model, the IOD is generated within the IO region by stronger austral summer winds and related cooler SSTs. On the other hand, atmospheric anomalies dissipate quickly during December–February following IOD in Pacific decoupled runs without a lingering basin-wide warming, as compared to the runs with an interactive Pacific [*Fischer et al.*, 2005; *Behera et al.*, 2006].

[88] Overall, results from both observations and models suggest to us that the IOD is a natural mode of the IO coupled system, which either can be externally triggered, by ENSO, for example, or can self-generate, provided the thermocline off Sumatra is shallow enough to support Bjerknes feedback. The IOD is weak in most years, likely because the Sumatra thermocline is too deep, a property that appears to vary on decadal time scales (section 5.3).

4.3. Other Modes

4.3.1. Tropical Biennial Oscillation

[89] Interannual rainfall variability over the Asian–Australian monsoon region displays a biennial tendency,

the Tropical Biennial Oscillation (TBO), with above-normal years often followed by below-normal years (see *Meehl and Arblaster* [2002] for a recent overview). Furthermore, a year with above-normal summer rainfall over India is often followed a season later by above-normal rainfall during December–February over the Australian monsoon region. Similarly, *Feng and Meyers* [2003] reported a biennial tendency in sea level variability over the equatorial IO from decade-long satellite observations. Meridional heat transport in a 40-year ocean model simulation driven by the NCEP–National Center for Atmospheric Research reanalysis of *Chirokova and Webster* [2006] also showed a broadband biennial signal. These properties resemble the quasi-biennial oscillation identified by *Toure and White* [2003] in spatially coherent IO sea level pressure and SST patterns propagating northward and eastward from the SWIO, its amplitude waxing and waning with the decadal modulation of ENSO.

[90] The cause of the TBO is not clear. As for the IOD, some researchers have suggested that it is an independent coupled climate mode in its own right [*Chang and Li*, 2000], whereas other researchers suggested that it is a forced disturbance in response to ENSO or IOD events. Concerning the ENSO–TBO relation, *Yu et al.* [2003] used partial-coupling experiments with an atmospheric GCM to argue that the El Niño suppresses convection of the Indian and Australian monsoons during June, July, and August (JJA) (year 0) and December, January, and February (DJF) (year 1), respectively, via an atmospheric bridge from the Pacific, whereas the ENSO-induced IO warming during JJA (year 1) following ENSO causes excessive rainfall throughout the tropical IO [*Yang et al.*, 2007] and in the Indian monsoon region [*Meehl and Arblaster*, 2002]. Thus, weak Indian and Australian monsoons during ENSO are followed by a strong Indian monsoon subsequent to the event.

[91] Concerning the IOD–TBO relation, the downwelling favorable equatorially trapped Rossby waves generated during an IOD event have been hypothesized to reflect from the western boundary as equatorial Kelvin waves, leading to the anomalous deepening of the Sumatran thermocline and, hence, opposite climate anomalies during the following year [*Loschnigg et al.*, 2003; *Meehl et al.*, 2003; *Li et al.*, 2003]. In support of the IOD/TBO linkage, IOD events increase their biennial spectral power in solutions to coupled models with the Pacific decoupled [*Fischer et al.*, 2005; *Behera et al.*, 2006].

4.3.2. Subtropical Dipole

[92] During Austral summer a northwestward tilted band of high SST variance typically develops over the subtropical South Indian Ocean. *Behera and Yamagata* [2001] showed that SST anomalies in the subtropical southeast IO tend to be out of phase with those in the midlatitude southwest IO, and this subtropical dipole is associated with wind changes in the subtropical anticyclonic circulation. *Chiodi and Harrison* [2007] found that latent heat flux changes due to anomalous meridional advection of moisture are important for the formation of this subtropical SST dipole. Ocean Rossby waves may also play a role [*Hermes and Reason*, 2005].

[93] The South IO SST dipole is related to southern African rainfall [e.g., *Reason*, 2002]. Similarly, *England et al.* [2006] identified a correlation between an SST pattern similar to this SST dipole with southwest Australian rainfall. There is also evidence that the South IO dipole is correlated with ENSO [*Hermes and Reason*, 2005]. Indeed, the subtropical South IO warming at the peak of El Niño is reproduced in atmospheric GCMs forced by observed SST in the tropical Pacific and coupled with an ocean mixed layer model elsewhere [e.g., *Alexander et al.*, 2002].

4.4. Climatic Impacts of IO SST Anomalies

[94] In sections 4.1 and 4.2, we have described the SST anomalies that develop in the IO during ENSO and IOD events. Here we report on their climatic impacts.

4.4.1. ENSO-Related SSTs

4.4.1.1. Indian Ocean

[95] There is growing evidence that the ENSO-induced basin-wide warming of the tropical IO persists until the summer following the event (Figure 12), impacting both local and remote climate. On the basis of atmospheric models of intermediate complexity, *Su et al.* [2001] and *Watanabe and Jin* [2002] showed that the warming increases local precipitation anomalies (more precisely, reduces the decrease of IO rainfall caused by El Niño); the increased precipitation in turn excites baroclinic waves that impact the atmosphere remotely. *Annamalai et al.* [2005c] and *Yang et al.* [2007] refer to this feedback as the “capacitor effect”: The tropical IO warms in response to El Niño (the charging process), and this warming then influences precipitation in the IO and surrounding regions after El Niño decays (the discharge process). *Annamalai et al.* [2005c] emphasize the role of SWIO warming in the capacitor, as it is maintained by ocean dynamics rather than surface heat flux (section 4.1.2). The warming in the North IO also persists for one season after El Niño has dissipated, sustained by the northeasterly wind anomalies that are in turn induced by the SWIO warming [*Du et al.*, 2009].

[96] The increased SWIO precipitation following ENSO (Figure 17c) is associated with an anomalous cyclonic circulation in the lower troposphere in the region (Figure 13), as well as an increase in the number of tropical cyclones there [*Xie et al.*, 2002]. The atmospheric response to SWIO SST anomalies has recently been reproduced in both atmospheric [*Annamalai et al.*, 2005c] and coupled [*Huang and Shukla*, 2007] models.

[97] *Annamalai et al.* [2005c] generalized these findings, comparing atmospheric GCM solutions forced by ENSO-related SST anomalies in both the Pacific and Indian oceans and in each basin separately. They confirmed the high correlation between precipitation and SST anomalies in the SWIO. Furthermore, they showed that the persistent SWIO warming anchors convection south of the equator, delaying the onset of the south Asian monsoon in May, a result consistent with the observational studies of *Joseph et al.* [1994] and *Kawamura et al.* [2001]. The SWIO warming effect on the Indian summer monsoon may also be indirect, by inducing a north-south asymmetric mode in boreal spring

via WES feedback [*Kawamura et al.*, 2001] and western Arabian Sea warming [*Izumo et al.*, 2008]. Indeed, western Arabian Sea SST is a significant predictor for summer Indian rainfall, together with ENSO and other SST anomalies in other IO regions [*Clark et al.*, 2000; *Vecchi and Harrison*, 2004].

[98] Australian monsoon rainfall (DJF) is negatively correlated with El Niño. On the basis of coupled model experiments, *Wu et al.* [2008] suggested that an actively coupled IO is key to the ENSO-Australian monsoon relationship, by increasing the variance of modeled ENSO and by directly influencing Australian summer rainfall.

4.4.1.2. Pacific Ocean

[99] An anomalous anticyclonic circulation develops over the tropical northwest Pacific at the mature phase of El Niño and persists into the following summer [*Huang et al.*, 2004; *Wang et al.*, 2003]. It is a robust feature associated with El Niño, with important effects on east Asian climate [*Xie et al.*, 2003]. While local SST plays a role in maintaining the northwest Pacific anticyclone [*Wang et al.*, 2000; *Lau and Nath*, 2003], *Watanabe and Jin* [2002] suggested that the IO warming is instrumental in its onset. Other atmospheric GCM studies have confirmed the effects of the warming on local precipitation and the northwest Pacific anticyclone [*Misra*, 2004]. *Annamalai et al.* [2005c] estimated that 50–60% of the precipitation variability over the maritime continent and tropical West Pacific is related to SWIO SST anomalies, through a change of the IO Walker Circulation.

[100] *Yang et al.* [2007] linked the persistence of the northwest Pacific anticyclone during the summer after El Niño has dissipated to the IO warming and the resulting increase in precipitation over the tropical IO. In their coupled model experiment, the IO warming suppresses atmospheric convection over the northwest Pacific, even though SST is anomalously warm there in response to a weakened southwest monsoon. Over the South China Sea, the summer SST warming following El Niño is especially pronounced, associated with decreased local precipitation and the weakened southwest monsoon [*Xie et al.*, 2003; *Wang et al.*, 2006]. Such a negative local correlation between SST and precipitation over summer monsoon regions has been noted by *Wang et al.* [2004], indicating the importance of remote SST forcing such as that from the tropical IO.

[101] In atmospheric GCMs, a tropical IO warming indeed leads to the formation of an anticyclonic circulation over the summer northwest Pacific [*Wu and Liu*, 1995; *Ohba and Ueda*, 2006]. *Xie et al.* [2009] propose the following mechanism for this IO teleconnection: the IO warming excites a warm atmospheric Kelvin wave that propagates into the Pacific. Surface friction induces subtropical divergence on the northern flank of the Kelvin wave, suppressing convection and forming a surface anticyclone with the help of convection-circulation feedback. Suppressed convection in the subtropical northwest Pacific further excites a meridional teleconnection called the Pacific-Japan pattern [*Nitta*, 1987; *Kosaka and Nakamura*, 2006] to affect summer rainfall over eastern China and Japan.

[102] In an extension of their SWIO study, *Annamalai et al.* [2007] showed that IO SSTs add noticeably to the global effects of ENSO. Specifically, they found that the Pacific–North American pattern is more accurately reproduced in their atmospheric GCM solutions forced by Pacific SSTs augmented by IO SSTs rather than by Pacific SSTs alone. Atmospheric circulation anomalies forced by SWIO SST interact destructively with those forced by Pacific SST anomalies, reducing this teleconnective activity despite the strong Pacific forcing.

[103] While most studies examine ENSO-induced SST anomalies and their feedback on the Pacific, *Terry and Dominiak* [2005] suggest that eastern IO SST near Australia during January–February is a good predictor for the subsequent ENSO development. The mechanisms for such an IO triggering of ENSO are unclear, but they speculate that these SST anomalies may initiate air-sea interaction over the tropical IO and then influence the Pacific. This IO-lead correlation is significant only after the mid-1970s.

4.4.2. IOD-Related SSTs

4.4.2.1. Remote Effects

[104] East African rainfall shows two maxima, a main one during April–June when the climatological ITCZ crosses the equator and a secondary one in October–December known as the “short rains.” Traditionally, increased short rainfall has been attributed to El Niño [*Ropelewski and Halpert*, 1987; *Hastenrath et al.*, 1993], but recent empirical studies show that it is more closely correlated to IOD events, specifically, the development of an anomalous westward equatorial SST gradient in the IO [*Birkett et al.*, 1999; *Black et al.*, 2003; *Clark et al.*, 2003; *Saji and Yamagata*, 2003].

[105] During the 1997–1998 IOD/ENSO event, there was catastrophic flooding in East Africa during the short rain season. *Latif et al.* [1999] investigated its cause using an atmospheric GCM, comparing solutions forced by observed SST anomalies in both the Indian and Pacific oceans and in the IO alone. They found that the latter solution yielded approximately the same rainfall precipitation dipole and East African rainfall as the former, pointing toward the essential influence of IO SSTs. Other model studies reported similar results [*Goddard and Graham*, 1999; *Behera et al.*, 2005].

[106] The precipitation dipole during IOD may induce remote atmospheric circulation changes outside the tropics via planetary wave adjustment. For example, IOD influences have been suggested on the Indian [*Ashok et al.*, 2001] and east Asian [*Guan and Yamagata*, 2003] summer monsoons and over the extratropical Southern Hemisphere [*Saji and Yamagata*, 2003].

4.4.2.2. Feedback to ENSO

[107] As noted above (section 4.2.3), ENSO strongly influences IOD events, among other things, providing a trigger to initiate them. Given the robust changes in atmospheric convection and circulation during IOD, the reverse question may also be asked: Does the IOD impact ENSO [*Behera and Yamagata*, 2003]? Coupled modeling experiments with and without an interactive IO suggest a positive

answer, with NINO3 SST variability increasing in amplitude and period in the latter case [*Yu et al.*, 2002; *Wu and Kirtman*, 2004].

[108] *Annamalai et al.* [2005a] presented observational evidence that El Niño grows faster during its onset (September–November) with than without an IOD. To investigate the cause of the difference, they compared solutions to an atmospheric GCM forced by a basin-wide warming and an IOD SST pattern over the tropical IO. The basin-wide warming forced an atmospheric Kelvin wave with anomalous easterlies in the western equatorial Pacific, whereas the IOD SST pattern excited little atmospheric response east of the maritime continent. Since anomalous easterlies over the western Pacific provide negative feedback to El Niño, the IOD development helps the growth of El Niño.

[109] There is observational and modeling evidence that El Niño decays more rapidly following an IOD than in the case without IOD [*Kug and Kang*, 2006]. In their coupled model study, *Kug et al.* [2006] showed that the rapid warming in the EEIO after IOD also excites an atmospheric Kelvin wave that causes Pacific easterlies. These winds shallow the thermocline in the eastern ocean, hastening the end of El Niño.

4.4.2.3. IOD-ISO Relation

[110] A relation between the zonal equatorial SST gradient and ISO activity was documented by *Shinoda and Han* [2005], who found strongly reduced submonthly and slightly reduced 30–90 day activity during IOD years (Figure 23). Their explanation was that intraseasonal atmospheric convection is highly suppressed in the eastern IO during a positive IOD phase, whereas it is enhanced during a negative phase; in the latter case, intraseasonal atmospheric convection occurs over the warm water in the east, causing westward propagating cyclonic atmospheric circulation anomalies that in turn generate anomalous westerlies over the EEIO.

[111] In 2006, an interesting interaction between MJOs, IOD, and Pacific El Niño was observed [*McPhaden*, 2008]. An IOD caused cool surface waters in the eastern equatorial IO, which damped the MJOs propagating over it during boreal fall. As a result, the MJOs had less of an effect in the western Pacific than they would otherwise have had in the case with no IOD.

4.5. Prediction

[112] The seasonal prediction of IO climate is still at the experimental stage, with varied success in predicting phenomena like the basin-wide warming following ENSO, Rossby waves in the South IO, and the IOD.

4.5.1. ENSO-Induced SSTAs

[113] The long persistence of NINO3 SST and the time lag of the IO response to ENSO give rise to predictability of IO SSTs. Indeed, a simple linear regression model with NINO3 as the sole predictor yields useful prediction of basin mean SST up to a 6-month lead [*Kug et al.*, 2004]. The long lead (6–12 months) in ENSO prediction boosts IO predictability and extends the lead of useful prediction by

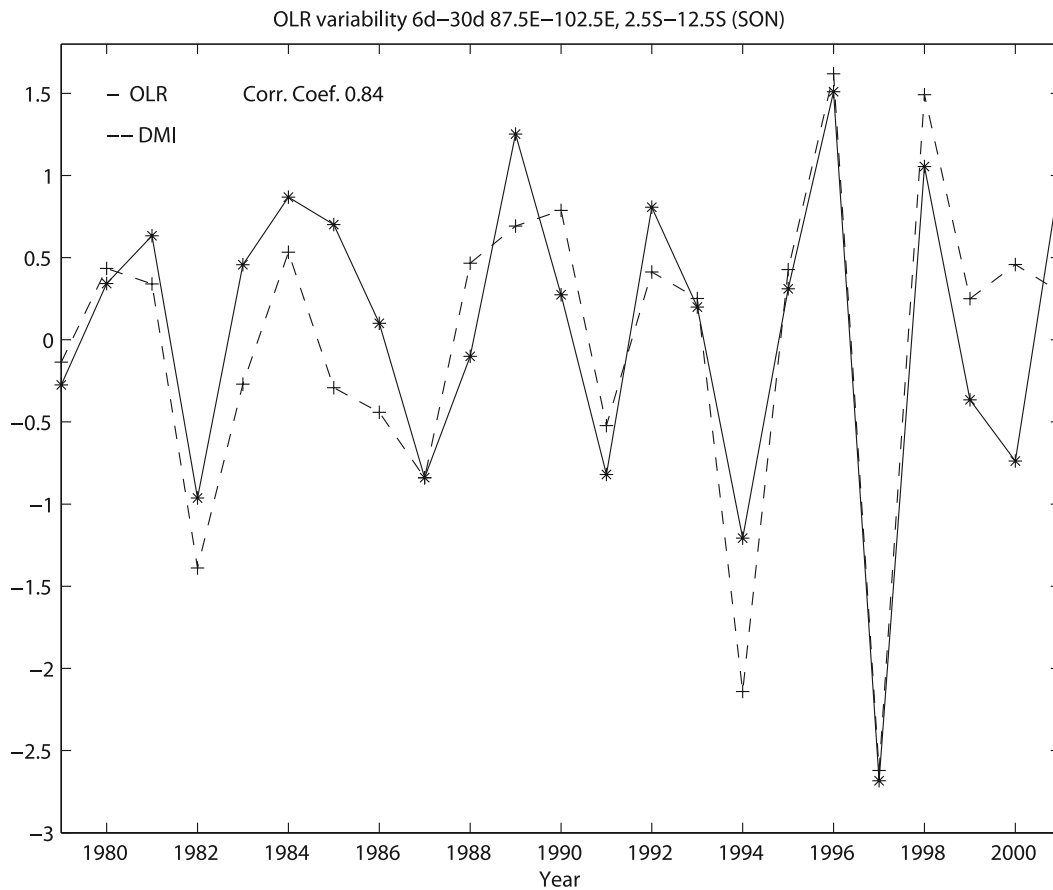


Figure 23. Variation of the intensity of the submonthly (6–30 days) OLR variability for the area 2.5–12.5°S, 87.5–102.5°E (solid line), and of the inverted dipole mode index (DMI) (dashed line) during SON. The intensity of OLR variability is measured by standard deviation of the band-pass-filtered (6–30 day) time series. Time series of the SON means are normalized by their standard deviations, and the overall means are subtracted [from *Shinoda and Han, 2005*].

more than 6 months [*Kug et al., 2004; Luo et al., 2005, 2007*].

[114] Because of the robust and slow propagation of ocean Rossby waves [e.g., *Xie et al., 2002*], the SWIO is one of the regions where SST has its highest predictability,

with an anomaly correlation coefficient (ACC) that remains above 0.6 at a 12-month lead for the 20-year experimental forecast from 1982 to 2001 [*Luo et al., 2005*]. SWIO SST is most predictable during March–May, the time of maximum thermocline depth variance associated with the arrival of

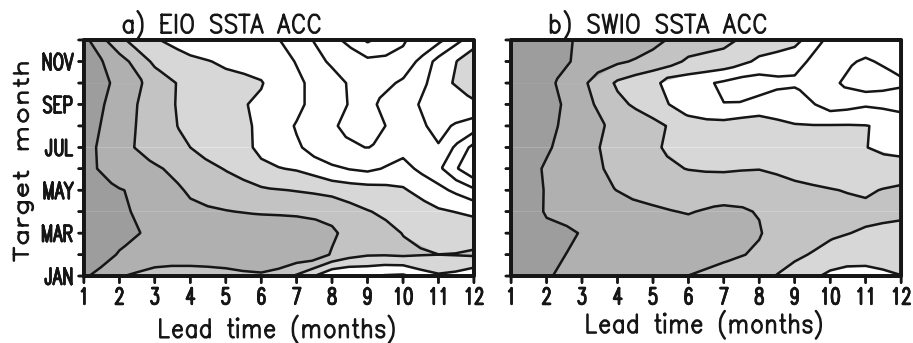


Figure 24. Seasonally stratified anomaly correlation coefficients (ACC) between the observations and model predictions during 1982–2006 for the SST anomalies in (a) the eastern Indian Ocean (EIO, 90–110°E, 10°S–0°) and (b) the southwestern region (southwestern IO (SWIO), 50–70°E, 15–5°S). Contour interval is 0.1, and values above 0.6 are shaded. Skills are calculated on the basis of the time series of 5-month running mean of both the observations and model hindcasts at each lead time (modified on the basis of *Luo et al. [2005, 2007]*).

oceanic Rossby waves [Xie et al., 2002], with an ACC as high as 0.7 at 12-month lead (Figure 24b). Similarly, the ACC minimum around October is associated with a minimum in thermocline depth variance.

[115] It is interesting to compare the skills of SWIO SST prediction between the coupled ocean-atmosphere models of Luo et al. [2005] and Alexander et al. [2002]. The former uses a dynamical ocean model and predicts Pacific SST in the coupled GCM, whereas the latter uses a mixed layer ocean model without wave dynamics and prescribes observed SST over the tropical Pacific. The high skill of the former model over the SWIO and the lack thereof in the latter support the importance of ocean dynamics there.

4.5.2. IOD SSTs

[116] Coupled GCMs show varied skill in predicting IOD events. The skills of SST prediction are generally higher over the western IO than the EEIO [Wajsowicz, 2004, 2005; Luo et al., 2005, 2007]. Over the EEIO, ACC decays rapidly, and useful skill is limited to about a 3-month lead (Figure 24a). Longer-lead forecasts give rise to many false alarms for EEIO cooling events if the coupled model features too strong a thermocline feedback [Wajsowicz, 2004]. Furthermore, a winter predictability barrier exists for EEIO SST with an ACC minimum in December [Luo et al., 2007] (Figure 24a): In December following IOD, EEIO SST shows a rapid reversal of sign in December (Figure 12) in observations as the southeasterly alongshore winds diminish [Xie et al., 2002; Li et al., 2003; Shinoda et al., 2004; Tokinaga and Tanimoto, 2004]. There is a tendency for ACC to recover during spring [Wajsowicz, 2007] because of El Niño-induced basin warming and/or ocean dynamic memory.

[117] The short lead for skillful prediction of EEIO SST appears to be related to the window for IOD development (June–October), which makes initialization important and may allow a larger role for atmospheric stochastic forcing by ISOs. Regarding the major IOD events of 1994 and 1997, some models predict both at 3-month lead [Wajsowicz, 2004, 2005] and some at only 1-month lead [Luo et al., 2005; Song et al., 2008]. On the basis of perfect model predictability experiments, Song et al. [2008] suggest that there are two types of IOD events, one unpredictable and one predictable. The former type may be triggered by weather noise, while the latter is predictable up to three seasons ahead and features a robust precursor of upper ocean warming over the central Pacific. A similar precursor is identified in observations [Annamalai et al., 2003].

[118] The IOD event in 2006 provided an opportunity for real-time forecast. The EEIO SST began with a rapid cooling in July, which peaked in September–October when the average SST change in the box, 90–110°E, 10°S–equator, was -1.2°C , and decayed rapidly after November. The dynamical prediction system at the Frontier Research Center for Global Change in Yokohama, Japan, showed the first indication of an upcoming IOD event in January 2006 [Luo et al., 2007] and produced a consistent IOD forecast from May onward (<http://www.jamstec.go.jp/frsgc/research/d1/iod/>). This result, along with the ongoing construction of

an IO observing system [Meyers and Boscolo, 2006], gives hope for skillful operational IO climate predictions in the future.

4.5.3. Impact of MJOs

[119] The propagation of MJOs from the IO into the western Pacific has proven to be a major “spoiler” in El Niño prediction [McPhaden, 2008]. The MJOs can suddenly interrupt a developing and seemingly predictable El Niño. Conversely, they can also force Ekman convergence, warming, and downwelling favorable Kelvin waves in a presumed non-ENSO year, which then suddenly develops an El Niño. The role of MJOs in modes of IO variability has not been fully explored.

5. LONGER-TERM VARIABILITY AND TRENDS

[120] In this section, we review observational and modeling evidence on IO variability at decadal and longer time scales. While there has been a basin-wide warming trend since the 1950s, the strong regional differences in heat storage and thermal structure changes require explanations involving ocean dynamics (section 5.1). The two shallow overturning cells, CEC and STC, both exhibit decadal variations, and variability in the ITF transport is likely to impact IO climate (section 5.2). Another issue is the variability in the IOD/ENSO relationship, which is strong during some decades and weak in others (section 5.3). Finally, the intensification of the Southern Annular Mode (SAM) over recent decades, which is projected to continue into the future, is having drastic effects on the South IO circulation and supergyre (section 5.4).

5.1. IO Warming Trend

5.1.1. Observed SST and Heat Storage Trends

[121] The IO SST warming trend, observed since the 1950s and amounting to about 0.5°C over the past 5 decades, appears to be part of the overall global warming, but there are some puzzling subbasin-scale features, which are difficult to explain by surface heating alone. Levitus et al. [2005] reported that IO heat storage has remained roughly constant in the upper 700 m in the northern IO over the past 50 years (Figure 25a) but has exhibited an increasing trend for the southern IO (Figure 25b); Barnett et al. [2005] suggested a possible explanation, noting that there is a hemispheric difference in net heat flux due to stronger concentrations of aerosols over the northern IO, which weaken the climate change signal there. Alory et al. [2007], analyzing a new Indian Ocean Temperature Archive (IOTA), reported other distinctive regional features: There was a particularly strong warming trend in the western subtropical IO from 40 to 50°S, corresponding to an increase of $1^{\circ}\text{--}2^{\circ}\text{C}$ over 40 years and extending to 800 m (Figure 25c); in contrast, the warming from 15°S to 5°N tended to be trapped above the 20°C isotherm with a subsurface cooling trend from 100 to 200 m. Such differences cannot be caused by surface heating; rather, they must involve shifts of the entire gyral temperature structure in response to changing dynamical forcing (e.g.,

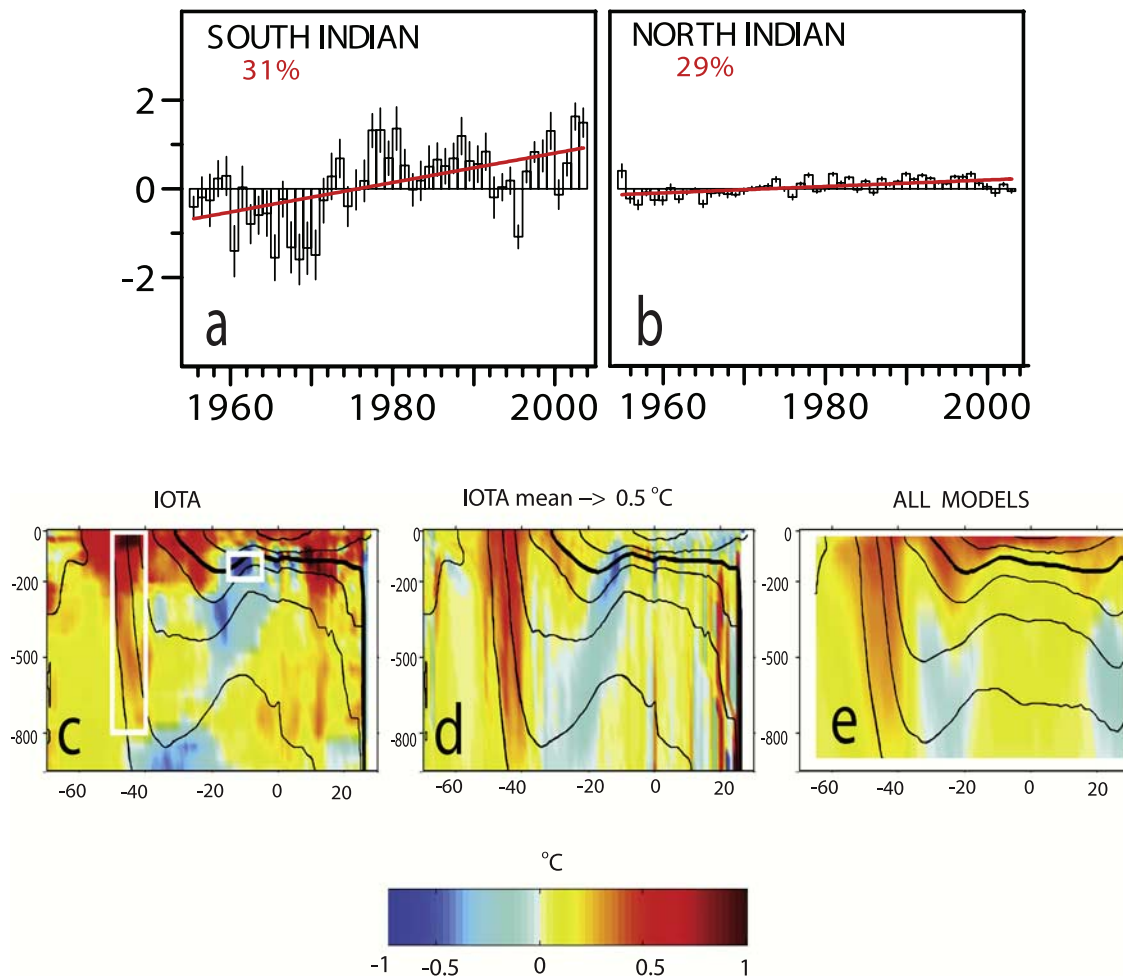


Figure 25. Time series 1955–2003 of yearly heat content (10^{22} J) of upper 700 m for (a) the southern and (b) the northern Indian Ocean, with vertical bars for ± 1 standard deviation of the annual means. Red lines are the respective trends, and percentages are the variances explained by each trend line (reprinted from Science [Levitus *et al.*, 2000]). (c) Zonally averaged temperature trends 1960–1999 (color shades) from new IO temperature archive (IOTA [from Alory *et al.*, 2007]). (d) As Figure 25c but calculated after shifting mean temperature structure by 0.5° southward. (e) Trends from mean structure of 10 Intergovernmental Panel on Climate Change models.

winds and across-boundary transports). In a cautionary note about such trend analyses, Harrison and Carson [2007] pointed out that the sparse data coverage in the IO, particularly the southern IO, makes an accurate determination of heat storage trends problematic. In fact, the IOTA analysis yields a much lower difference between the North Indian Ocean and South Indian Ocean heat content changes (G. Alory, personal communication, 2007).

5.1.2. Heat Flux Dilemma

[122] Concerning surface heating as a cause for the warming, there still exists a great uncertainty even about the sign of the net heat flux into or out of some parts of the IO. This uncertainty is illustrated in Figure 26a, which shows the zonally averaged net heat fluxes from six climatologies [Yu *et al.*, 2007]. The latest, and perhaps best validated climatology, is OAFflux, based on recent buoy-calibrated bulk formulae for latent and sensible heat fluxes and on longwave and shortwave radiation measurements from the International Satellite Cloud Climatology Project

(ISCCP); it differs by as much as 50 W m^{-2} from other frequently used climatologies, such as the European Centre for Medium-Range Weather Forecasts reanalysis or NCEP 1/2 (Figure 26a). As a result, there is a large spread in the cross-equatorial heat flux among the climatologies, determined by integrating the net heat fluxes southward from the northern boundary (Figure 26b), and ocean models even extend this spread [Godfrey *et al.*, 2007] (section 6.2.2).

[123] Nevertheless, when comparing time series of annual mean heat fluxes over the past 2 decades, the air-sea flux climatologies all agree that the net heat flux into the IO has not increased; rather, it has even slightly decreased during 1988–2000 (on the average by about $4\text{--}5 \text{ W m}^{-2}$), although the magnitude of the trends differs among the products (Figure 26c). This suggests that ocean dynamics play a role in the IO warming trend. The caveat here is that the accuracy and duration of these products may not allow an accurate determination of the trend in surface flux.

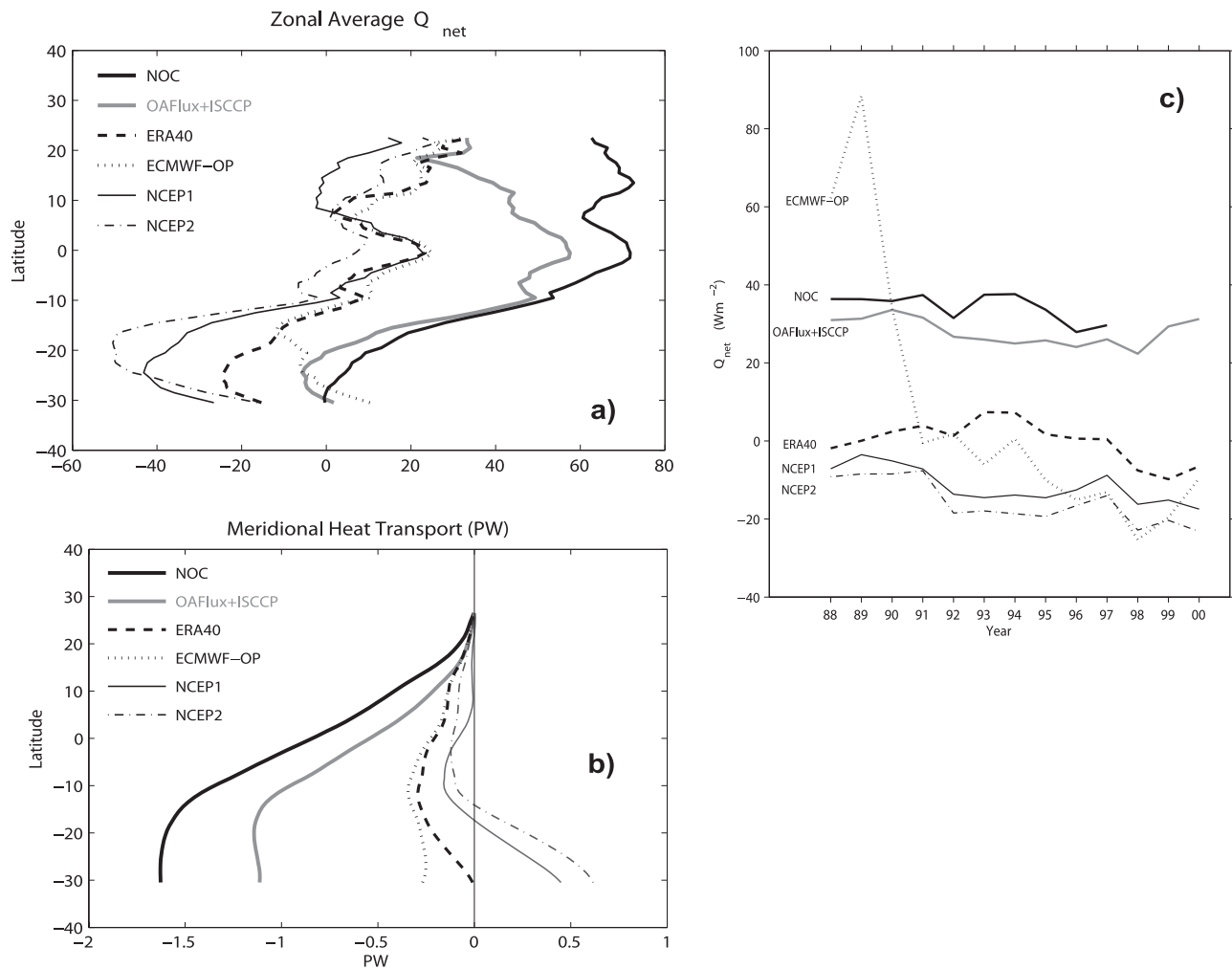


Figure 26. (a) Zonal means of net heat IO fluxes (downward positive in $W m^{-2}$) from different climatologies [from Yu *et al.*, 2007]; (b) northward heat transport (in petawatts = 10^{15} W) of the northern IO, from same climatologies (courtesy L. Yu); and (c) net heat fluxes for the climatologies over the IO 1988–2000 [from Yu *et al.*, 2007]. Note that meridional heat transport can only be taken equivalent to ocean heat transport north of about $5^{\circ}S$ before Indonesian Throughflow enters the IO (Q_{net} positive for heat flux into the ocean).

5.1.3. Models

[124] A number of modeling studies have investigated the causes of the IO warming trend. Many coupled GCMs simulate the warming trend when forced by the observed history of atmospheric trace gases, aerosols, and land cover types [Knutson *et al.*, 1999; Hoerling *et al.*, 2004; Barnett *et al.*, 2005; Alory *et al.*, 2007], and the trend is absent without anthropogenic forcing [Knutson *et al.*, 2006]. Seemingly contradictory, however, in the IPCC-AR4 models changes in net surface heat flux are small ($<1 W m^{-2}$) during the steady 20th century warming. Du and Xie [2008] suggested a solution to the dilemma by decomposing the flux into greenhouse radiative forcing, atmospheric feedback, and oceanic Newtonian damping. Increased downward long-wave radiation triggers the warming, which is then amplified by the water vapor feedback and atmospheric adjustments (such as relaxed wind) that reduce surface evaporation. The resulting SST warming, however, strengthens evaporative cooling through the Clausius-

Clapeyron effect, and the strengthened cooling then almost compensates for the increased radiative forcing and atmospheric feedback so that the net flux remains largely unchanged.

[125] In their comparison of 10 IPCC-AR4 models, Alory *et al.* [2007] concluded that increased Southern Hemisphere westerlies have strengthened the subtropical gyre, leading to a pattern in the heat storage trend very similar to the observations (Figure 25e): The trends of Figures 25c and 25e can be well approximated if the observed mean temperature structure is shifted just slightly southward by 0.5° (Figure 25d).

5.1.4. Remote Impacts

[126] Models have been used to isolate multidecadal effects of the IO warming trend on other parts of the globe. For example, the IO warming forces robust geopotential height anomalies during the boreal winter in the upper troposphere, with a strong projection onto the North Atlantic Oscillation and annular modes [Lu *et al.*, 2004; Hoerling

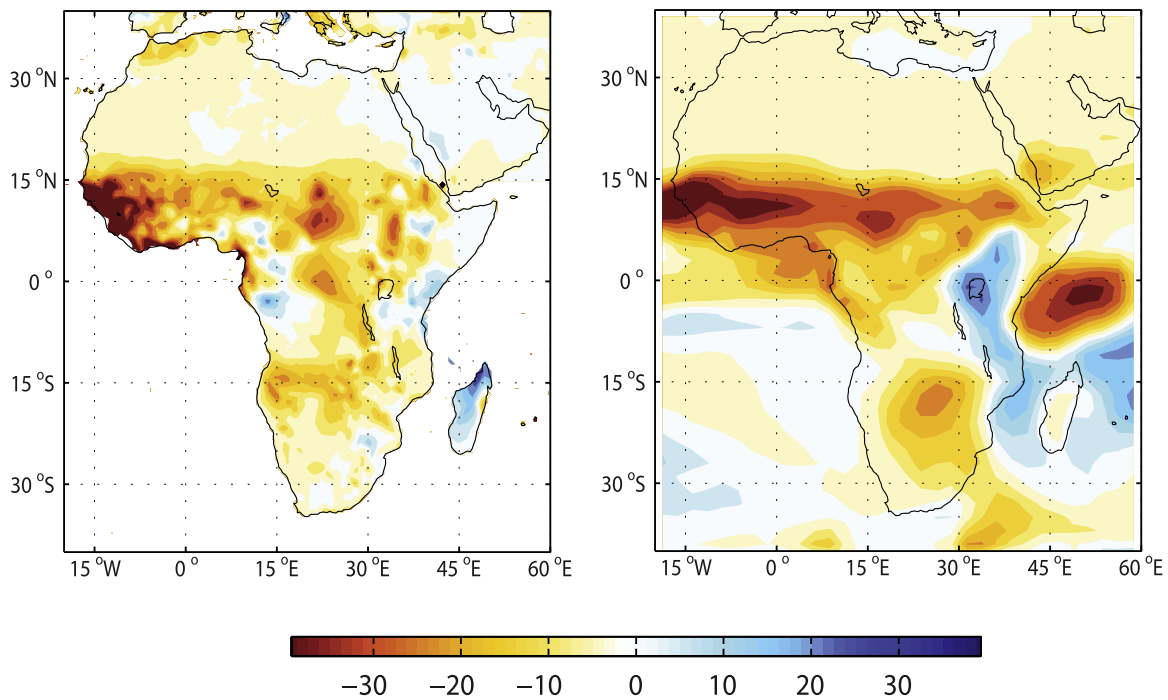


Figure 27. Observed and modeled rainfall trends. (left) The linear trend from 1950 to 2000 in the observed annual mean rainfall over land, in mm/month. Blue areas correspond to a trend toward wetter conditions, and brown areas correspond to a trend toward a drier climate. (right) Linear trend for an ensemble mean of 10 simulations with an atmospheric general circulation model (GCM) running over observed sea surface boundary conditions [from *Held et al.*, 2005].

et al., 2004]. Positive height anomalies are centered at 40°N/S with large values over the North Pacific and North Atlantic, but anomalies over the Arctic appear to vary from one model to another [Hoerling *et al.*, 2004; Lau *et al.*, 2006; Annamalai *et al.*, 2007]. Hoerling and Kumar [2003] suggested that both IO warming and a persistent La Niña in the Pacific caused the prolonged droughts for 1998–2002 over North America, the Mediterranean, and the Middle East; the La Niña cooling induced extratropical anomalies that reinforced those caused by the IO warming [Lau *et al.*, 2006].

[127] Another impact zone is the Sahel, a semiarid belt bordering the Sahara Desert to the north and wet equatorial Africa to the south. Sahel precipitation has steadily declined from 1950 to 1990 [Folland *et al.*, 1986] and only recently has shown signs of stabilization/recovery. Forced by observed SST, many atmospheric GCMs reproduce this drying trend (Figure 27) [Palmer, 1986; Giannini *et al.*, 2003; Lu and Delworth, 2005; Held *et al.*, 2005; Hoerling *et al.*, 2006]. Additional experiments suggest that much of the trends over the Sahel and other parts of Africa is due to the IO warming [Giannini *et al.*, 2003; Bader and Latif, 2003; Hoerling *et al.*, 2006]. Results from the 20th century runs of coupled models are mixed [Held *et al.*, 2005; Hoerling *et al.*, 2006], suggesting that other factors such as Atlantic SST [Zhang and Delworth, 2006] may also have an impact.

[128] Increased precipitation in response to the tropical IO warming trend is a key forcing for the remote responses noted above. We caution, however, that there still is no solid

observational evidence for such a tropical convective response to the warming trend [Deser and Phillips, 2006; Copsey *et al.*, 2006]. The observational study of Deser *et al.* [2004] related interdecadal changes in IO SST to those over the midlatitude North Pacific.

5.2. CEC and STC Slowdowns

[129] Schoenefeldt and Schott [2006] diagnosed a significant slowdown of the CEC (section 2.3) from 1955 to 1990 in the SODA reanalysis [Carton *et al.*, 2000], which is forced by Comprehensive Ocean-Atmosphere Data Set wind stress fields. The result of a downward trend in cross-equatorial Sverdrup transport was a simultaneous decrease of the northward thermocline flow by the Somali Current, of the southward shallow upper layer (Ekman/Sverdrup) return flow across the equator and of northwestern coastal upwelling. Somewhat unexpectedly, however, they also found that the cross-equatorial heat transport was not affected by this slowdown because the temperature fluxes of both the northward cold Somali Current and the southward warm near-surface warm counterflow equally declined, compensating each other.

[130] A slowdown of the IO STC during 1992–2000 was reported by Lee [2004]. Evaluating satellite altimetry and scatterometer winds, he found a decrease of the easterlies driving STC upwelling at 5–10°S by about 70% and corresponding downward trend in sea level at 10–15°S in the SWIO due to reduced southward Ekman transports. The SWIO sea level reduction in turn was associated with a decrease of zonal geostrophic pressure gradient and reduced

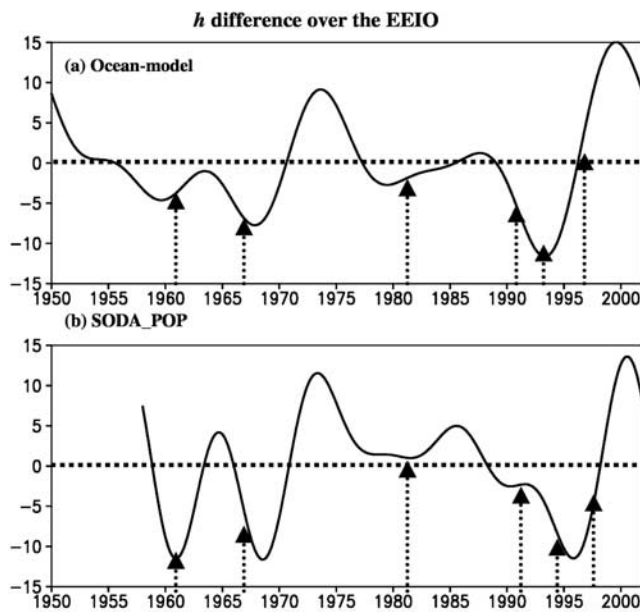


Figure 28. Mixed layer depth in eastern IO (10°S – 0° ; 90 – 110°E) in (a) ocean GCM driven by NCEP winds and (b) SODA assimilation model output. Vertical lines mark IOD occurrences [from Annamalai et al., 2005b].

northward thermocline flow. For the region north of the equator, however, zonal wind stresses stayed about constant during 1992–2000, suggesting no decrease of the CEC, in agreement with the post-1992 results from SODA.

[131] Most recently, a rebound of the IO STC was documented for the period 2000–2006 [Lee and McPhaden, 2008], with the easterlies at 10°S (and thus southward Ekman transports) returning to about their level prior to the decrease during the 1990s. Similarly, satellite altimetry indicated a reversal of the zonal sea level trend at about 15°S . It had exhibited a slowdown of the northward geostrophic thermocline STC flow during the 1990s, which recovered during 2000–2006.

5.3. Decadal IOD Variability and Role of ITF

5.3.1. Decadal IOD Variability

[132] The IOD has displayed decades of strong events in the 1960s and the 1990s (Figure 22a) [Ashok et al., 2004; Annamalai et al., 2005b] and was particularly weak in the 1980s (Figure 20). As the variance of SST in the western and eastern IOD poles shows (Figure 22b), the decadal variation of IOD amplitude is dominantly determined by the eastern pole, showing especially high SST variance in the 1990s and 1960s. ENSO also undergoes decadal variations (Figure 22a) and so does the correlation between ENSO and IOD (Figure 22c). The correlation, based on sliding 11 year segments, was low in the 1950s to 1960, had a maximum in the mid-1970s, and then stayed at a high level.

[133] Using SODA reanalysis and coupled model analysis, Ashok et al. [2004] determined decadal correlations between the IOD index and thermocline (Z20) depth variations. They identified a decadal pattern that resembles the interannual IOD, that is, with extended periods of

shallow thermocline in the east, and concluded that the decadal variations are not just air-sea interface effects but that ocean dynamics play a role. Annamalai et al. [2005b] investigated these changes in a suite of ocean model experiments. They preconditioned the initial state of the runs by first forcing the model with idealized easterly (westerly) winds over the tropical IO, yielding a shallow (deep) thermocline in the east; then, solutions were obtained by superimposing observed anomalous winds of past IOD episodes. They found that only for preconditioning with a shallow eastern thermocline could IODs develop.

[134] Noting that the EEIO thermocline in their ocean GCM solutions (Figure 28a), as well as in the SODA reanalysis (Figure 28b), was generally shallower during 1952–1971 and 1990–1996, they concluded that clustering of IOD events in those decades resulted from preconditioning by the shallow thermocline, thereby favoring Bjerknes feedback in the IO. They argued further that the preconditioning was related to Pacific decadal variability, both by an atmospheric bridge and by a slowing ITF.

[135] A corollary of these results is that when the EEIO thermocline is anomalously deep, the occurrence of IOD event requires strong triggering by ENSO, which is associated with alongshore wind anomalies along Sumatra and Java that force upwelling there (Figure 15b). Thus, there are more co-occurrences of ENSO and IOD under these conditions, in contrast to the more independent IODs that can be triggered at times when the EEIO thermocline is shallow. Indeed, the highest IOD-ENSO correlation occurs in the early 1970s, when the EEIO mixed layer was deep (Figures 22b and 28).

[136] A 200-year run of a coupled model was analyzed by Tozuka et al. [2007] for decadal IO SST variability (in the 9–35 year band), and two leading EOFs were identified: a basin-wide in-phase warming mode, resembling decadal ENSO variability (see section 4.1.1), and a decadal dipole mode, resembling IOD. Closer inspection, though, showed that this mode was not really decadal but was in fact due to decadal variations of interannual IOD events.

[137] In IPCC simulations under increased greenhouse gas forcing, the EEIO thermocline shallows as the equatorial westerlies weaken [Vecchi and Soden, 2007; Du and Xie, 2008]. Indeed, coral records show that SST warming during the 20th century is weaker in the EEIO than in the western tropical IO during the IOD season and that the frequency of IOD occurrence is on the rising trend [Abram et al., 2008]. Ocean GCM hindcasts forced by atmospheric reanalysis winds, however, show that the EEIO thermocline deepens instead from 1961 to 2000 in response to increased equatorial westerly winds [Trenary and Han, 2008]. Adding to the confusion, IOD variance remains largely unchanged in IPCC model projections under increased greenhouse gas forcing, despite the shoaling thermocline in the EEIO [Ihara et al., 2009]. Lack of reliable observations prevents a conclusive determination of spatial patterns of IO changes for the past century, and sustained observations are necessary to monitor future changes.

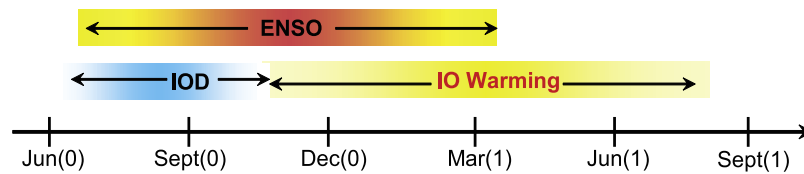


Figure 29. Seasonality of major interannual IO climate modes.

5.3.2. Indonesian Throughflow

[138] The ITF provides an oceanic bridge from the Pacific to the IO and vice versa which is known to be active at intraseasonal-to-interannual time scales (sections 2.5.1 and 4.1.6) and potentially has even larger impact at longer time scales through its impact on IO thermohaline structure. Besides being generated by thickness anomalies propagating in from the Pacific, IO variability can also be generated by across-basin wind stress, and both components are difficult to keep apart.

[139] A new Pacific wave pathway has been suggested to affect the ITF and thickness anomalies off northwest Australia on decadal time scales, namely, the propagation of midlatitude Rossby waves from the subtropical North Pacific [Cai *et al.*, 2005a]. On the basis of their evaluation of the SODA reanalysis and solutions to a coupled model, Shi *et al.* [2007] found the northern pathway to be unimportant (prominent) before (after) 1980, coinciding with periods of weak (strong) El Niños.

[140] Regarding the described multidecadal variations in coupled models forced by increased greenhouse forcing during the 20th century studies, Alory *et al.* [2007] found a relation between the multidecadal shallow surface warming and subsurface cooling at 15°S – 5°N in the IO (section 5.1.3) with the strength of the Pacific trade winds and proposed that advection via the ITF was involved. In their evaluation of IPCC models, Vecchi and Soden [2007] found that the EEIO thermocline structure shallowed under increased greenhouse gas forcing, weakening the zonal sea level gradient along the equator, and related these changes to a weakening of the ITF forced by a weaker Pacific Walker circulation.

5.4. Southern Annular Mode

[141] Over the past 3 decades there has been a strengthening of the circumpolar westerlies, as expressed by an upward trend of the SAM Index [e.g., Kushner *et al.*, 2001]. The observed upward decadal trend in wind forcing has resulted in a strengthening of the supergyre, at least regarding its barotropic stream function in a variety of models [Cai *et al.*, 2005b; Cai and Cowan, 2007]. In support of these findings, Cai [2006] presented evidence for a strengthened southward East Australian Current and southward propagation of lower-latitude Pacific marine species along the east coast of Australia toward the Tasman Sea, where these species were formerly not observed.

[142] The Antarctic ozone distribution has been identified as a major factor in the recent observed SAM strengthening. Gillett and Thompson [2003], forcing an atmospheric GCM just with the observed stratospheric ozone depletion, were

able to reproduce the observed SAM development. Model simulations into the 21st century under greenhouse gas forcing scenarios predict a further upward trend of SAM, leading to a further intensification of the supergyre [Cai *et al.*, 2005b].

[143] The role of ozone depletion in SAM trends and its effects on the IO needs further study. On the one hand, Cai and Cowan [2007] find in their IPCC-AR4 model evaluation that ozone depletion contributed as much to observed SAM trends over the past 4 decades as Greenhouse warming did. On the other hand, Alory *et al.* [2007] concluded that coupled models including ozone depletion do not show differences in IO subtropical warming against those that do not include ozone. They suggest that intermodel differences affect IO warming in the models more than the forcing differences, diluting the cause/effect chain from wind forcing to Sverdrup function, barotropic stream function, and then subsurface temperature trends, especially when all quantities are zonally averaged (G. Alory, personal communication, 2007).

6. SUMMARY AND CONCLUSIONS

[144] Only a decade ago, the IO was perceived by most climate scientists to be climatologically passive, essentially behaving as a slab mixed layer regarding its interaction with the atmosphere. (The sole exception to this view was the western Arabian Sea, where summertime Somali upwelling was known to cool SST locally and, hence, to suppress atmospheric convection.) Since that time, this perception has changed profoundly. In this paper, we have reviewed recent evidence pointing toward the climatic importance of IO SSTs and the role of ocean dynamics in generating them. Here we summarize what, in our view, the major recent discoveries have been and comment on the observational and modeling challenges that remain.

6.1. Main Research Findings of the Past Decade

[145] Without a doubt, the most influential finding about IO climate of the past decade is the Indian Ocean Dipole (IOD). IOD events are identified by cool (warm) SST and suppressed (enhanced) precipitation anomalies in the eastern (western) IO, together with anomalous equatorial easterlies (Figure 18). They are seasonally phase locked, reaching their peak in the fall (Figure 29) when the thermocline is sufficiently shallow off Sumatra and Java to allow upwelling of cool subsurface water. About half of the documented IOD events over the past several decades occurred independently of ENSO [Meyers *et al.*, 2007].

[146] ENSO impacts the IO through an atmospheric bridge, and a major study area has been the mutual interaction of ENSO and IOD. Associated with the eastward withdrawal of atmospheric convection over Indonesia at the beginning of El Niño, anticyclonic wind stress curl occurs over the tropical southeast IO with alongshore upwelling favorable winds off Sumatra (Figure 15b). Thus, the seasonal timing of the El Niño onset is crucial for IOD development (Figure 29). Conversely, IOD events can impact the life cycle of ENSO, both during its onset and decay (section 4.4.2.2).

[147] What processes favor IOD development in the absence of ENSO? First, intraseasonal variations can lift the thermocline off Sumatra, in particular, upwelling favorable equatorial Kelvin waves with a 90-day period [Iskandar et al., 2006]. Second, decadal variability of eastern thermocline depth (Figure 28) is caused either by an atmospheric bridge or by the ITF. Third, there are indications that the Walker circulation is changing under global warming [Vecchi et al., 2006], shallowing the thermocline in the east and thus causing quasi-permanent IOD preconditioning [Vecchi and Soden, 2007].

[148] An important process during El Niño (and IOD) events is remote forcing of the SWIO through downwelling favorable off-equatorial Rossby waves, which are caused by anticyclonic wind stress curl in the east (Figures 15 and 16). The associated mixed layer thickening and SST warming in the west causes increased cyclogenesis and precipitation (Figures 14 and 17). El Niño–induced basin-wide IO warming persists through the following summer (Figure 29). This “capacitor effect” impacts climate in the surrounding regions long after El Niño has dissipated (section 4.4.1).

[149] There have been several recent efforts for the experimental seasonal prediction of IO SSTs and their climatic impacts. The El Niño–induced basin-wide IO warming is now predictable with about a 1-year lead in coupled models that have skill in predicting ENSO and its IO teleconnections. Luo et al. [2007] were able to forecast the 2006 IOD with some success several months in advance.

[150] Intraseasonal variability occurs in both the atmosphere and the ocean, the two often being linked. The MJOs are perhaps the most well known of the atmospheric ISOs: During boreal winter, they interact strongly with the 5–10°S thermocline ridge; during the summer, they spin off northward propagating ISOs, which bring rainfall to India and Southeast Asia. Both MJOs and northward propagating ISOs are believed to be primarily atmospheric phenomena (they exist in stand-alone atmospheric GCMs), but there is an increasing recognition that they are also strengthened by feedbacks from covarying SST anomalies. A major climate role of the MJOs is that after propagating into the western Pacific, they can impact the enhancement or demise of developing ENSO events, bringing uncertainties to ENSO prediction [McPhaden, 2008].

[151] At decadal-to-interdecadal time scales, trends of SST and heat storage were reported in recent years, including a strong increase of South IO heat storage and the lack

thereof in the North IO (Figure 25a) and decadal changes in the strengths of the IO’s shallow overturning circulations, the CEC and the Southern Hemisphere STC (Figure 6). A puzzling aspect is that despite a robust SST warming, the net heat flux into the IO has been diagnosed from different observational data sets to have a slight downward trend (Figure 26c), although the net flux trend is probably too small to be detected [Du and Xie, 2008]. The secular IO warming trend appears to impact remote climate and may be causing the well-known trend in African rainfall. On the other hand, models disagree on the high-latitude response to IO warming, often with conflicting results.

[152] A number of studies have explored the role of the oceanic bridge via the ITF. At shorter time scales, Kelvin waves propagate from the IO into the Pacific, and Rossby waves propagate from the Pacific (both equatorial and off-equatorial, from the North Pacific) into the IO, while at ENSO/IOD and longer time scales the preconditioning of Sumatra upwelling can be set by advection of thermocline anomalies from the Pacific. Finally, the discovery of the “supergyre” (Figures 5 and 7) [Ridgway and Dunn, 2007] and its intensification in response to the ongoing strengthening of the Southern Annular Mode foreshadow significant changes of subtropical circulation and Indo-Pacific exchange [Cai and Cowan, 2007].

6.2. Observational and Modeling Challenges

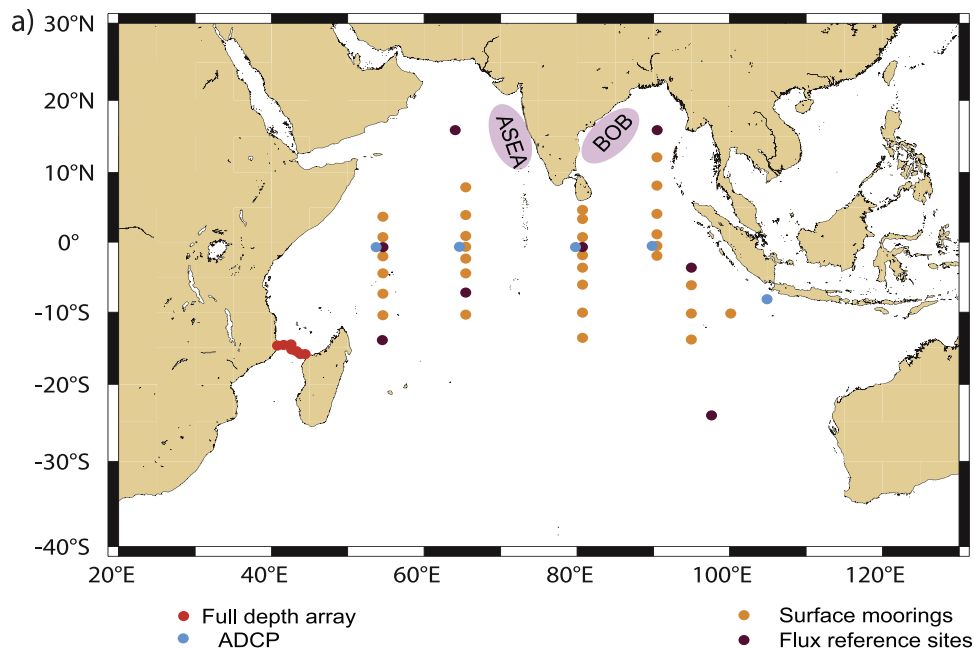
6.2.1. Observational Challenges

6.2.1.1. Satellite Observations

[153] Improved IO observations have been the key to many of the recent advances in IO climate research. For example, satellite altimetry has been instrumental for monitoring ocean thermocline adjustments (through the close relationship between sea level and thermocline depth), leading to the realization of the importance of dynamics in IO climate (e.g., Bjerknes feedback, South Indian Ocean Rossby waves, and wave connections between the Pacific and Indian oceans). The retention of altimetric satellites on a permanent basis is therefore of prime importance. Likewise, continuation of the TMI instrument aboard TRMM, which led to the discovery of covarying SST anomalies with ISOs over the Bay of Bengal and elsewhere, is essential.

6.2.1.2. Moored Station Network

[154] Apart from a few mooring sites of the past that were maintained for 1–2 years (SMC01), time series of subsurface structures and currents could only be estimated over longer time spans from repeat XBT lines reaching back to the 1980s. Establishing a system of moored stations similar to the Tropical Atmosphere-Ocean (TAO) array of the Pacific is pivotal for further success in understanding IO climate variability and improving predictive skill. Such an array has been proposed by the Climate Variability and Predictability (CLIVAR)/Global Ocean Observing System Indian Ocean Panel [International CLIVAR Project Office, 2006]. The proposed array, named Research Moored Array for African-Asian-Australian Monsoon Analysis and Prediction [McPhaden et al., 2009], consists of 46 stations (Figure 30a), covering the equatorial belt (including



Indian Ocean Moored Buoy Array

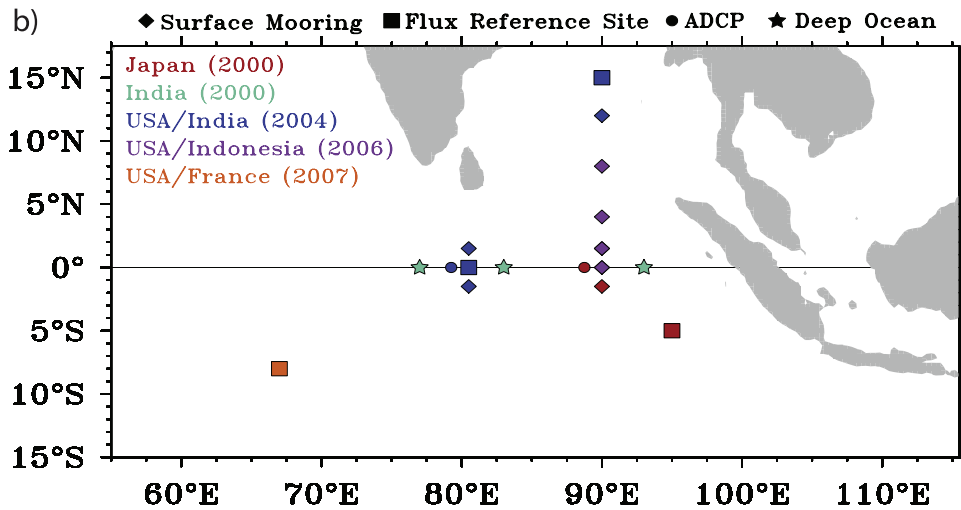


Figure 30. (a) Moored station network Research Moored Array for African-Asian-Australian Monsoon Analysis and Prediction, designed for IO climate studies [International CLIVAR Project Office, 2006]. (b) Status of deployed stations and plans in fall 2007 [McPhaden et al., 2009].

acoustic Doppler current profilers (ADCPs), blue in Figure 30a) and also the important wave guide in the 5–15°S latitude range (Figure 16). Eight sites have been selected for deploying flux measurement buoys (brown in Figure 30a), in order to resolve the discrepancies among existing products (Figure 26) [Yu and Weller, 2007].

[155] At present, the central and eastern equatorial part of the array is nearly complete, making about one third of the proposed network available (Figure 30b). In addition, regional moored buoy programs have been established east and west of India (ASEA and BOB in Figure 30a), and a moored array now covers the Mozambique Channel.

[156] An initial success of the array is the documentation of the IOD event of fall 2006 [Horii et al., 2008]. At the 90°E moorings (Figure 30b), a subsurface cooling and westward current anomaly were observed to begin in May followed by a decrease in SST about 3 months later. Thus, the array provided a comprehensive database for improved modeling of that IOD episode.

6.2.1.3. Hydrographic Profile Collection

[157] The coverage of hydrographic measurements in the IO, particularly in the Southern Hemisphere, has been sparse until recently. The Argo program of autonomous floats has developed into an IO success story, expanding the number of profiles from 628 in 2001 to more than 16,000 in

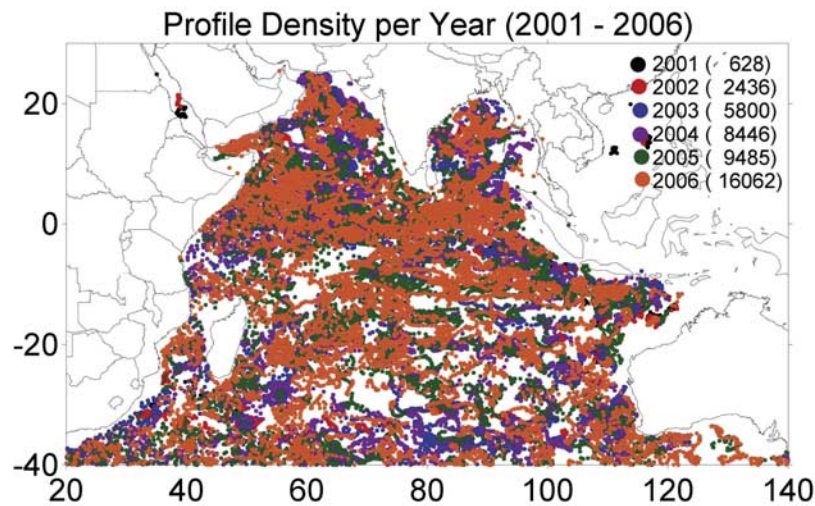


Figure 31. Annual distribution (colors) and number of Array for Real-Time Geostrophic Oceanography temperature-salinity profiles for 2001–2006 (courtesy M. Ravichandran).

2006 (Figure 31). These profiles provide hydrographic data in broad regions of the IO where no shipboard observations are taken. They are also important for determining the near-surface thermohaline structure in barrier layer regions. Argo captured the remarkable westward propagation of barrier layer development in the South IO during the 2006 El Niño/IOD event as the downwelling Rossby wave lowered the thermocline by as much as 60 m (J. Chowdary et al., Vertical structure of the 2006–07 Rossby wave event in the southwest Indian Ocean, submitted to *Geophysical Research Letters*, 2008).

[158] The continuation of Argo in the IO is essential for understanding IO climate. The next generation of instruments envisioned will be gliders, which can be programmed to crisscross current systems and provide simultaneous hydrographic and current profiles. Such profiling systems would also be less prone to vandalism than the present TAO-type moorings with surface buoys are.

6.2.2. Modeling and Reanalysis

6.2.2.1. Ocean Models

[159] One hindrance to progress is that existing models are deficient in a number of ways. For example, at the present time, ocean model performance does not appear to be helpful in deciding whether the larger or the lower estimate of meridional heat transports of Figure 26b should be more trustworthy. *Godfrey et al.* [2007], evaluating a variety of different models, IO basin and global, found a mean heat transport of the model group of more than double the mean obtained when averaging the climatology curves (Figure 26b). That difference corresponds to a heat flux difference of about 40 W m^{-2} for the northern IO. The authors concluded that the model physics were deficient, involving spurious convective overturning, numerical mixing, and unrealistic horizontal diffusion. If subsurface mixing is not adequately parameterized, the simulated thermocline becomes too thick; this error affects the temperature of the water that upwells and hence SST. Among the AR4 models, the EEIO thermocline depth varies

from 85 to 155 m [*Saji et al.*, 2006a]. Part of the model heat transport shortcomings can also be lack of proper representation of heat transports carried by ISO-generated covariances [*Halkides et al.*, 2007].

6.2.2.2. Atmospheric and Coupled Models

[160] Atmospheric and coupled GCMs continue to have problems in accurately simulating monsoon precipitation and its intraseasonal and seasonal variations, long-standing problems stemming from the poor representation of convection-circulation interaction and orographic effects of narrow mountain ranges. How does air-sea interaction modulate atmospheric ISOs, and do coupled models improve the prediction of intraseasonal variability?

[161] To the extent that ENSO is an important forcing for IO variability, it is important to improve ENSO simulations in coupled GCMs. For example, many models fail to simulate the observed ENSO seasonality in the IO, with El Niño peaking in boreal summer in some models instead of winter as observed. This erroneous seasonality surely affects the ENSO/IOD relationship in the model. In addition, while promising progress has been made in predicting IOD, some models produce too many false alarms for IOD prediction, whereas others underpredict IOD events. Most notably, many models failed to predict the 2006 IOD event, concurrent with a weak El Niño in the Pacific. Regarding the El Niño–induced IO warming, it remains unclear what sustains the warming during and after the decay of El Niño, a question of great practical importance for predicting summer anomalies over the northwest Pacific and east Asia.

[162] Inconsistencies need to be resolved between model simulations and observations with regard to how the atmosphere responds to the IO warming trend. Does IO precipitation increase in response, and what remote effects does the local response excite via teleconnections? While coupled models agree that Antarctic ozone depletion would increase the westerly winds, they disagree on the effect of this wind increase on the southern IO. What causes these intermodel differences, and how can they be overcome?

TABLE A1. List of Acronyms

Acronym	Definition
Argo	Array for Real-Time Geostrophic Oceanography
COADS	Comprehensive Ocean-Atmosphere Data Set
EACC	East African Coastal Current
EEIO	eastern equatorial IO
ENSO	El Niño–Southern Oscillation
EUC	Equatorial Undercurrent
GCM	general circulation model
GW	Great Whirl
IO	Indian Ocean
ISO	Intraseasonal Oscillation
ITF	Indonesian Throughflow
MJO	Madden-Julian Oscillation
NCEP	U.S. National Centers for Environmental Prediction
NEMC	Northeast Madagascar Current
NMC	Northeast Monsoon Current
POP	Parallel Ocean Program
SAM	Southern Annular Mode
SEC	South Equatorial Current
SECC	South Equatorial Countercurrent
SMC	Southwest Monsoon Current
SODA	Simple Ocean Data Assimilation
SSH	sea surface height
SST	sea surface temperature
SWIO	southwestern Indian Ocean
TAO	Tropical Atmosphere-Ocean
TRMM	Tropical Rain Measuring Mission
WOCE	World Ocean Circulation Experiment
XBT	expendable bathythermograph

6.2.2.3. Model-Data Integrations

[163] Assimilating data into models is perhaps the only approach for obtaining long time series from gappy data, which is a particularly severe problem in the IO. In this review, we have mentioned several results from the SODA reanalysis [Carton *et al.*, 2000] and more recent SODA-POP development [Carton and Giese, 2008], which are extensively used by the community. The SODA assimilation technique (optimum interpolation) has the well-known problem that it can generate density anomalies (jumps) that lead to fictitious geostrophic currents and Rossby waves in the ocean. Other assimilation methods, like the four-dimensional variational (4dVAR) method used by the Estimating the Climate and Circulation of the Ocean reanalysis [Stammer *et al.*, 2004], avoid this problem but introduce others. Much needs to be done to ensure that we have trustworthy assimilation reanalyses, especially when they are used to study subtle phenomena like water mass conversion and subsurface circulations. Another way to use models to improve the efficiency of observational arrays is to carry out Observing System Simulation Experiments [Vecchi and Harrison, 2007]; such studies seek to optimize the combined scientific return from different network components, such as moored time series and Argo floats.

APPENDIX A

[164] In Table A1, we list all the acronyms that appear in the paper.

[165] **ACKNOWLEDGMENTS.** Fritz Schott acknowledges support from Deutsche Forschungsgemeinschaft (DFG) through contract Scho 168/29. Julian McCreary and Shang-Ping Xie

acknowledge support from the Japan Agency for Ocean-Earth Science and Technology (JAMSTEC) and NASA through their sponsorship of the IPRC. We thank W. Wang (IFM-GEOMAR and ZMAW Hamburg), R. Schoenefeldt (Oxford University), and Jan Hafner and Ryo Furue (IPRC) for helping with the figures. J.-J. Luo (JAMSTEC), L. Yu (WHOI), Mike McPhaden (NOAA/PMEL), and M. Ravichandran (INCOIS) were kind enough to supply unpublished Figures 24, 26, 30, and 31. This manuscript is SOEST contribution 7457 and IPRC contribution 522. Finally, Fritz Schott is grateful to M. Kneba, H. Horst, and S. Neuman and their team of II. Medizinische Klinik, Kiel, for their help and support in fighting a grave illness during the time of this writing. Fritz did not survive his fight with leukemia. Remarkably, he worked on our paper throughout his struggle, learning that it had been accepted shortly before his death. His passion for science was the driving force that made this paper (and the other papers we have written with him) possible. Even 6 months later, we still cannot believe that our long-time friend and colleague is gone. We will always miss him.

[166] The Editor responsible for this paper was Henk Dijkstra. He thanks two technical reviewers along with one anonymous technical reviewer.

REFERENCES

- Abram, N. J., M. K. Gagan, J. E. Cole, W. S. Hantoro, and M. Mudelsee (2008), Recent intensification of tropical climate variability in the Indian Ocean, *Nat. Geosci.*, *1*, 849–853, doi:10.1038/ngeo357.
- Alexander, M. A., I. Bladé, M. Newman, J. R. Lanzante, N.-C. Lau, and J. D. Scott (2002), The atmospheric bridge: The influence of ENSO teleconnections on air-sea interaction over the global oceans, *J. Clim.*, *15*, 2205–2231.
- Allan, R. J., et al. (2001), Is there an Indian Ocean Dipole independent of the El Niño-Southern Oscillations?, *CLIVAR Exch.*, *6*(3), 18–22.
- Alory, G., S. Wijffels, and G. Meyers (2007), Observed temperature trends in the Indian Ocean over 1960–1999 and associated mechanisms, *Geophys. Res. Lett.*, *34*, L02606, doi:10.1029/2006GL028044.
- Annamalai, H., and R. Murtugudde (2004), Role of the Indian Ocean in regional climate variability, in *Earth's Climate: The Ocean-Atmosphere Interaction*, *Geophys. Monogr. Ser.*, vol. 147, edited by C. Wang, S.-P. Xie, and J. A. Carton, pp. 213–246, AGU, Washington, D. C.
- Annamalai, H., and K. R. Sperber (2005), Regional heat sources and the active and break phases of boreal summer intraseasonal (30–50 day) variability, *J. Atmos. Sci.*, *62*, 2726–2748.
- Annamalai, H., R. Murtugudde, J. Potemra, S.-P. Xie, P. Liu, and B. Wang (2003), Coupled dynamics over the Indian Ocean: Spring initiation of the zonal mode, *Deep Sea Res., Part II*, *50*, 2305–2330.
- Annamalai, H., S.-P. Xie, J.-P. McCreary, and R. Murtugudde (2005a), Impact of Indian Ocean sea surface temperature on developing El Niño, *J. Clim.*, *18*, 302–319.
- Annamalai, H., J. Potemra, R. Murtugudde, and J. P. McCreary (2005b), Effect of preconditioning on the extreme climate events in the tropical Indian Ocean, *J. Clim.*, *18*, 3450–3469.
- Annamalai, H., P. Liu, and S.-P. Xie (2005c), Southwest Indian Ocean SST variability: Its local effect and remote influence on Asian monsoons, *J. Clim.*, *18*, 4150–4167.
- Annamalai, H., H. Okajima, and M. Watanabe (2007), Possible impact of the Indian Ocean SST on the Northern Hemisphere during El Niño, *J. Clim.*, *20*, 3164–3189.
- Armstrong, E. M., and J. Vazquez-Cuervo (2001), A new global satellite-based sea surface temperature climatology, *Geophys. Res. Lett.*, *28*, 4199–4202.

- Ashok, K., Z. Guan, and T. Yamagata (2001), Impact of the Indian Ocean Dipole on the relationship between the Indian monsoon rainfall and ENSO, *Geophys. Res. Lett.*, *28*, 4499–4502, doi:10.1029/2001GL013294.
- Ashok, K., W.-L. Chan, T. Motoi, and T. Yamagata (2004), Decadal variability of the Indian Ocean Dipole, *Geophys. Res. Lett.*, *31*, L24207, doi:10.1029/2004GL021345.
- Bader, J., and M. Latif (2003), The impact of decadal-scale Indian Ocean sea surface temperature anomalies on Sahelian rainfall and the North Atlantic Oscillation, *Geophys. Res. Lett.*, *30*(22), 2169, doi:10.1029/2003GL018426.
- Baquero-Bernal, A., and M. Latif (2005), Wind-driven oceanic Rossby waves in the tropical South Indian Ocean with and without an active ENSO, *J. Phys. Oceanogr.*, *35*, 729–746.
- Baquero-Bernal, A., M. Latif, and S. Legutke (2002), On dipole-like variability of sea surface temperature in the tropical Indian Ocean, *J. Clim.*, *15*, 1358–1368.
- Barnett, T. P., D. W. Pierce, K. M. Achutarao, P. J. Gleckler, B. D. Santer, J. M. Gregory, and W. M. Washington (2005), Penetration of human-induced warming into the world's oceans, *Science*, *309*, 284–287.
- Behera, S. K., and T. Yamagata (2001), Subtropical SST dipole events in the southern Indian Ocean, *Geophys. Res. Lett.*, *28*, 327–330.
- Behera, S. K., and T. Yamagata (2003), Influence of the Indian Ocean Dipole on the Southern Oscillation, *J. Meteorol. Soc. Jpn.*, *81*, 169–177.
- Behera, S. K., R. Krishnan, and T. Yamagata (1999), Unusual ocean-atmosphere conditions in the tropical Indian Ocean during 1994, *Geophys. Res. Lett.*, *26*, 3001–3004, doi:10.1029/1999GL010434.
- Behera, S. K., P. S. Salvekar, and T. Yamagata (2000), Simulation of interannual SST variability in the tropical Indian Ocean, *J. Clim.*, *13*, 3487–3499.
- Behera, S. K., S. A. Rao, H. N. Saji, and T. Yamagata (2003), Comments on “A cautionary note on the interpretation of EOFs”, *J. Clim.*, *16*, 1087–1093.
- Behera, S. K., et al. (2005), Paramount impact of the Indian Ocean Dipole on the East African short rains: A CGCM study, *J. Clim.*, *18*, 4514–4530.
- Behera, S. K., J.-J. Luo, S. Masson, S. A. Rao, H. Sakuma, and T. Yamagata (2006), A CGCM study on the interaction between IOD and ENSO, *J. Clim.*, *19*, 1688–1705.
- Bhat, G. S., et al. (2001), Bay of BengalMEX: The Bay of Bengal Monsoon Experiment, *Bull. Am. Meteorol. Soc.*, *82*, 2217–2243.
- Birkett, C., R. Murtugudde, and T. Allan (1999), Indian Ocean climate event brings floods to East Africa's lakes and the Sudd marsh, *Geophys. Res. Lett.*, *26*, 1031–1034, doi:10.1029/1999GL000165.
- Bjerknes, J. (1969), Atmospheric teleconnections from the equatorial Pacific, *Mon. Weather Rev.*, *97*, 163–172.
- Black, E., J. Slingo, and K. R. Sperber (2003), An observational study of the relationship between excessively strong short-rains in coastal East Africa and Indian Ocean SST, *Mon. Weather Rev.*, *131*, 74–94.
- Brandt, P., M. Dengler, A. Rubino, D. Quadfasel, and F. Schott (2003), Intraseasonal variability in the southwestern Arabian Sea and its relation to the seasonal circulation, *Deep Sea Res., Part II*, *50*, 2129–2142.
- Cadet, D. L. (1985), The Southern Oscillation over the Indian Ocean, *J. Climatol.*, *5*, 189–212.
- Cai, W. (2006), Antarctic ozone depletion causes an intensification of the southern ocean super-gyre circulation, *Geophys. Res. Lett.*, *33*, L03712, doi:10.1029/2005GL024911.
- Cai, W., and T. Cowan (2007), Trends in Southern Hemisphere circulation in IPCC AR4 models over 1950–99: Ozone depletion versus Greenhouse forcing, *J. Clim.*, *20*, 681–693.
- Cai, W., G. Meyers, and G. Shi (2005a), Transmission of ENSO signal to the Indian Ocean, *Geophys. Res. Lett.*, *32*, L05616, doi:10.1029/2004GL021736.
- Cai, W., G. Shi, T. Cowan, D. Bi, and J. Ribbe (2005b), The response of the Southern Annular Mode, the East Australian Current, and the southern mid-latitude ocean circulation to global warming, *Geophys. Res. Lett.*, *32*, L23706, doi:10.1029/2005GL024701.
- Carton, J. A., and B. S. Giese (2008), A reanalysis of ocean climate using Simple Ocean Data Assimilation (SODA), *Mon. Weather Rev.*, *136*, 2999–3017.
- Carton, J. A., G. Chepurin, X. Cao, and B. Giese (2000), A simple ocean data assimilation analysis of the global upper ocean 1950–95. Part I: Methodology, *J. Phys. Oceanogr.*, *30*, 294–309.
- Chambers, D. P., B. D. Tapley, and R. H. Stewart (1999), Anomalous warming in the Indian Ocean coincident with El Niño, *J. Geophys. Res.*, *104*, 3035–3047.
- Chang, C.-P., and T. Li (2000), A theory for tropical tropospheric biennial oscillation, *J. Atmos. Sci.*, *57*, 2209–2224.
- Chang, P., et al. (2006), Climate fluctuations of tropical coupled system: The role of ocean dynamics, *J. Clim.*, *19*, 5122–5174.
- Chatterjee, P., and B. N. Goswami (2004), Structure, genesis and scale selection of the tropical quasi-biweekly mode, *Q. J. R. Meteorol. Soc.*, *130*(599), 1171–1194.
- Chen, T. C., and J. M. Chen (1993), The 10–20-day mode of the 1979 Indian monsoon: Its relation with the time variation of monsoon rainfall, *Mon. Weather Rev.*, *121*, 2465–2482.
- Chiang, J. C. H., and B. R. Lintner (2005), Mechanisms of remote tropical surface warming during El Niño, *J. Clim.*, *18*, 4130–4149.
- Chiang, J. C. H., and A. H. Sobel (2002), Tropical tropospheric temperature variations caused by ENSO and their influence on the remote tropical climate, *J. Clim.*, *15*, 2616–2631.
- Chikamoto, Y., and Y. Tanimoto (2005), Role of specific humidity anomalies in Caribbean SST response to ENSO, *J. Meteorol. Soc. Jpn.*, *83*, 959–975.
- Chioldi, A. M., and D. E. Harrison (2007), Mechanisms of summertime subtropical southern Indian Ocean sea surface temperature variability: On the importance of humidity anomalies and the meridional advection of water vapor, *J. Clim.*, *20*, 4835–4852.
- Chirokova, G., and P. J. Webster (2006), Interannual variability of Indian Ocean heat transport, *J. Clim.*, *19*, 1013–1031.
- Clark, C. O., J. E. Cole, and P. J. Webster (2000), Indian Ocean SST and Indian summer rainfall: Predictive relationships and their decadal variability, *J. Clim.*, *13*, 2503–2519.
- Clark, C. O., P. J. Webster, and J. E. Cole (2003), Interdecadal variability of the relationship between the Indian Ocean Zonal Mode and East African coastal rainfall anomalies, *J. Clim.*, *16*, 548–554.
- Copsey, D., R. Sutton, and J. R. Knight (2006), Recent trends in sea level pressure in the Indian Ocean region, *Geophys. Res. Lett.*, *33*, L19712, doi:10.1029/2006GL027175.
- Davis, R. D. (2005), Intermediate-depth circulation of the Indian and South-Pacific Oceans measured by autonomous floats, *J. Phys. Oceanogr.*, *35*(5), 683–707.
- de Ruijter, W. P. M., H. Ridderinkhof, J. R. E. Lutjeharms, M. W. Schouten, and C. Veth (2002), Observations of the flow in the Mozambique Channel, *Geophys. Res. Lett.*, *29*(10), 1502, doi:10.1029/2001GL013714.
- de Ruijter, W. P. M., H. M. van Aken, E. J. Beier, J. R. E. Lutjeharms, R. P. Matano, and M. W. Schouten (2004), Eddies and dipoles around South Madagascar: Formation, pathways and large-scale impact, *Deep Sea Res., Part I*, *51*, 383–400.
- Deser, C., and A. Phillips (2006), Simulation of the 1976/77 climate transition over the North Pacific: Sensitivity to tropical forcing, *J. Clim.*, *19*, 6170–6180.
- Deser, C., A. S. Phillips, and J. W. Hurrell (2004), Pacific interdecadal climate variability: Linkages between the tropics and the North Pacific during boreal winter since 1900, *J. Clim.*, *17*, 3109–3124.
- Domingues, C. M., M. E. Maltrud, S. E. Wijffels, J. A. Church, and M. Tomczak (2007), Simulated Lagrangian pathways between the Leeuwin Current System and the upper-ocean circulation of the southeast Indian Ocean, *Deep Sea Res., Part II*, *54*, 797–817.

- Donohue, K. A., and J. M. Toole (2003), A near-synoptic survey of the Southwest Indian Ocean, *Deep Sea Res., Part II*, 50, 1893–1932.
- Du, Y., and S.-P. Xie (2008), Role of atmospheric adjustments in the tropical Indian Ocean warming during the 20th century in climate models, *Geophys. Res. Lett.*, 35, L08712, doi:10.1029/2008GL033631.
- Du, Y., T. Qu, G. Meyers, Y. Masumoto, and H. Sasaki (2005), Seasonal heat budget in the mixed layer of the southeastern tropical Indian Ocean in a high-resolution ocean general circulation model, *J. Geophys. Res.*, 110, C04012, doi:10.1029/2004JC002845.
- Du, Y., S.-P. Xie, G. Huang, and K. Hu (2009), Role of air-sea interaction in the long persistence of El Niño-induced North Indian Ocean warming, *J. Clim.*, in press.
- Duvel, J. P., and J. Vialard (2007), Indo-Pacific sea surface temperature perturbations associated with intraseasonal oscillations of tropical convection, *J. Clim.*, 20, 3056–3082.
- Duvel, J. P., R. Roca, and J. Vialard (2004), Ocean mixed layer temperature variations induced by intraseasonal convective perturbations over the Indian Ocean, *J. Atmos. Sci.*, 61, 1004–1023.
- England, M. H., and F. Huang (2005), On the interannual variability of the Indonesian Throughflow and its linkage with ENSO, *J. Clim.*, 18, 1435–1444.
- England, M. H., C. C. Ummerhofer, and A. Santoso (2006), Interannual rainfall extremes over southwest Western Australia linked to Indian Ocean climate variability, *J. Clim.*, 19, 1948–1969.
- Feng, M., and G. Meyers (2003), Interannual variability in the tropical Indian Ocean: A two-year time scale of IOD, *Deep Sea Res., Part II*, 50(12–13), 2263–2284.
- Ffield, A., and A. L. Gordon (1992), Vertical mixing in the Indonesian thermocline, *J. Phys. Oceanogr.*, 22, 184–195.
- Fischer, A., P. Terray, E. Guilyardi, S. Gualdi, and P. Delecluse (2005), Two independent triggers for the Indian Ocean Dipole/Zonal Mode in a coupled GCM, *J. Clim.*, 18, 3428–3449.
- Folland, C. K., T. N. Palmer, and D. E. Parker (1986), Sahelian rainfall and worldwide sea surface temperatures 1901–1985, *Nature*, 320, 602–607.
- Fu, X., B. Wang, T. Li, and J. P. McCreary (2003), Coupling between northward-propagating, intraseasonal oscillations and sea surface temperature in the Indian Ocean, *J. Atmos. Sci.*, 60, 1733–1753.
- Fukutomi, Y., and T. Yasunari (2005), Southerly surges on sub-monthly time scales over the eastern Indian Ocean during the Southern Hemisphere winter, *Mon. Weather Rev.*, 133, 1637–1654.
- Ganachaud, A., C. Wunsch, and J. Marotzke (2000), The meridional overturning and large-scale circulation of the Indian Ocean, *J. Geophys. Res.*, 105, 26,117–26,134.
- Giannini, A., R. Saravanan, and P. Chang (2003), Oceanic forcing of Sahel rainfall on interannual to interdecadal time scales, *Science*, 302, 1027–1030.
- Gill, A. E. (1982), *Atmosphere-Ocean Dynamics*, 662 pp., Academic, New York.
- Gillett, N. P., and D. W. J. Thompson (2003), Simulation of recent Southern Hemisphere climate change, *Science*, 302, 273–275.
- Goddard, L., and N. E. Graham (1999), Importance of the Indian Ocean for simulating rainfall anomalies over the eastern and southern Africa, *J. Geophys. Res.*, 104(D16), 19,099–19,116.
- Godfrey, J. S., and E. J. Lindstrom (1989), The heat budget of the equatorial western Pacific surface mixed layer, *J. Geophys. Res.*, 94(C6), 8007–8017.
- Godfrey, J. S., and J. V. Mansbridge (2000), Ekman transports, tidal mixing, and the control of temperature structure in Australia's northwest waters, *J. Geophys. Res.*, 105, 24,021–24,044.
- Godfrey, J. S., G. C. Johnson, M. J. McPhaden, G. Reverdin, and S. Wijffels (2001), The tropical ocean circulation, in *Ocean Circulation and Climate*, edited by J. Church, J. Gould, and G. Siedler, pp. 215–24, Academic, London.
- Godfrey, J. S., R.-J. Hu, A. Schiller, and R. Fiedler (2007), Explorations of the annual mean heat budget of the tropical Indian Ocean. Part I: Studies with an idealized model, *J. Clim.*, 20, 3210–3228.
- Gordon, A. L. (2005), Oceanography of the Indonesian seas and their throughflow, *Oceanography*, 18, 14–27.
- Goswami, B. N., and J. Shukla (1984), Quasiperiodic oscillations in a symmetric general circulation model, *J. Atmos. Sci.*, 41, 20–37.
- Gualdi, S., E. Guilyardi, A. Navarra, S. Masina, and P. Delecluse (2003), The interannual variability in the tropical Indian Ocean as simulated by a CGCM, *Clim. Dyn.*, 20, 567–582.
- Guan, Z., and T. Yamagata (2003), The unusual summer of 1994 in East Asia: IOD teleconnections, *Geophys. Res. Lett.*, 30(10), 1544, doi:10.1029/2002GL016831.
- Halkides, D. J., W. Han, T. Lee, and Y. Masumoto (2007), Effects of sub-seasonal variability on seasonal-to-interannual Indian Ocean meridional heat transport, *Geophys. Res. Lett.*, 34, L12605, doi:10.1029/2007GL030150.
- Han, W. (2005), Origins and dynamics of the 90-day and 30–60 day variations in the equatorial Indian Ocean, *J. Phys. Oceanogr.*, 35, 708–728.
- Han, W., and J. P. McCreary (2001), Modelling salinity distributions in the Indian Ocean, *J. Geophys. Res.*, 106, 859–877.
- Han, W., J. P. McCreary, D. L. T. Anderson, and A. J. Mariano (1999), Dynamics of the eastern surface jets in the equatorial Indian Ocean, *J. Phys. Oceanogr.*, 29, 2191–2209.
- Han, W., P. Webster, R. Lukas, P. Hacker, and A. Hu (2004), Impact of atmospheric intraseasonal variability in the Indian Ocean: Low-frequency rectification in the equatorial surface current and transport, *J. Phys. Oceanogr.*, 34, 1350–1372.
- Harrison, D. E., and M. Carson (2007), Is the world ocean warming? Upper ocean trends, 1950–2000, *J. Phys. Oceanogr.*, 37, 174–187.
- Harrison, D. E., and G. A. Vecchi (2001), January 1999 Indian Ocean cooling event, *Geophys. Res. Lett.*, 28, 3717–3720.
- Hastenrath, S., A. Nicklis, and L. Greischar (1993), Atmospheric-hydropheric mechanisms of climate anomalies in the western equatorial Indian Ocean, *J. Geophys. Res.*, 98, 20,219–20,235.
- Held, I. M., T. L. Delworth, J. Lu, K. L. Findell, and T. R. Knutson (2005), Simulation of Sahel drought in the 20th and 21st centuries, *Proc. Natl. Acad. Sci. U. S. A.*, 102, 17,891–17,896.
- Hendon, H. H., and M. L. Salby (1994), The life cycle of the Madden-Julian Oscillation, *J. Atmos. Sci.*, 51, 2225–2237.
- Hermes, J. C., and C. J. C. Reason (2005), Ocean model diagnosis of interannual coevolving SST variability in the South Indian and South Atlantic oceans, *J. Clim.*, 18, 2864–2882.
- Hirst, A. C., and J. S. Godfrey (1993), The role of Indonesian Throughflow in a global ocean GCM, *J. Phys. Oceanogr.*, 23, 1057–1086.
- Hoerling, M., and A. Kumar (2003), The perfect ocean for drought, *Science*, 299, 691–694.
- Hoerling, M., J. W. Hurrell, T. Xu, G. T. Bates, and A. S. Phillips (2004), Twentieth century North Atlantic climate change. Part II: Understanding the effect of Indian Ocean warming, *Clim. Dyn.*, 23, 391–405.
- Hoerling, M., J. W. Hurrell, J. Eischeid, and A. Phillips (2006), Detection and attribution of twentieth-century northern and southern African rainfall change, *J. Clim.*, 19, 3989–4008.
- Horii, T., H. Hase, I. Ueki, and Y. Masumoto (2008), Oceanic precondition and evolution of the 2006 Indian Ocean Dipole, *Geophys. Res. Lett.*, 35, L03607, doi:10.1029/2007GL032464.
- Huang, B., and J. L. Kinter III (2002), Interannual variability in the tropical Indian Ocean, *J. Geophys. Res.*, 107(C11), 3199, doi:10.1029/2001JC001278.
- Huang, B., and J. Shukla (2007), On the mechanisms for the interannual variability in the tropical Indian Ocean. Part I: The role of remote forcing from the tropical Pacific, *J. Clim.*, 20, 2917–2936.

- Huang, R.-H., W. Chen, B. Yang, and R. Zhang (2004), Recent advances in studies of the interaction between the east Asian winter and summer monsoons and ENSO cycle, *Adv. Atmos. Sci.*, *21*, 407–424.
- Huffman, G. J., R. F. Adler, D. T. Bolvin, G. Gu, E. J. Nelkin, K. P. Bowman, Y. Hong, E. F. Stocker, and D. B. Wolff (2007), The TRMM multisatellite precipitation analysis (TMPA): Quasi-global, multiyear, combined-sensor precipitation estimates at fine scales, *J. Hydrometeorol.*, *8*, 38–55.
- Ihara, C., Y. Kushnir, M. A. Cane, and V. H. de la Peña (2009), Climate change over the equatorial Indo-Pacific in global warming, *J. Clim.*, in press.
- Iizuka, S., T. Matsuura, and T. Yamagata (2000), The Indian Ocean SST dipole simulated in a coupled general circulation model, *Geophys. Res. Lett.*, *27*, 3369–3372.
- Inness, P., J. M. Slingo, E. Guilyardi, and J. Cole (2003), Simulation of the Madden-Julian Oscillation in a coupled general circulation model. Part II: The role of the basic state, *J. Clim.*, *16*, 365–382.
- International CLIVAR Project Office (2006), Understanding the role of the Indian Ocean in the climate system—Implementation plan for sustained observations, *CLIVAR Publ. Ser.*, *100*, Southampton, U. K.
- Iskandar, I., W. Mardiansyah, Y. Masumoto, and T. Yamagata (2005), Intraseasonal Kelvin waves along the southern coast of Sumatra and Java, *J. Geophys. Res.*, *110*, C04013, doi:10.1029/2004JC002508.
- Iskandar, I., T. Tozuka, H. Sasaki, Y. Masumoto, and T. Yamagata (2006), Intraseasonal variations of surface and subsurface currents off Java as simulated in a high-resolution ocean general circulation model, *J. Geophys. Res.*, *111*, C12015, doi:10.1029/2006JC003486.
- Izumo, T., C. de Boyer Montegut, J.-J. Luo, S. K. Behera, S. Masson, and T. Yamagata (2008), The role of the western Arabian Sea upwelling in Indian monsoon rainfall variability, *J. Clim.*, *21*, 5603–5623.
- Jensen, T. G. (1993), Equatorial variability and resonance in a wind driven Indian Ocean model, *J. Geophys. Res.*, *98*, 22,533–22,552.
- Jensen, T. G. (2003), Cross-equatorial pathways of salt and tracers from the northern Indian Ocean: Modelling results, *Deep Sea Res., Part II*, *50*, 2111–2128.
- Jiang, X., T. Li, and B. Wang (2004), Structure and mechanisms of the northward propagating boreal summer intraseasonal oscillation, *J. Clim.*, *17*, 1022–1039.
- Jochum, M., and R. Murtugudde (2005), Internal variability of Indian Ocean SST, *J. Clim.*, *18*, 3726–3738.
- Joseph, P. V., J. K. Eischeid, and R. J. Pyle (1994), Interannual variability of the onset of the Indian summer monsoon and its association with atmospheric features, El Niño, and sea surface temperature anomalies, *J. Clim.*, *7*, 81–105.
- Jury, M. R., and B. Huang (2004), The Rossby wave as a key mechanism of Indian Ocean climate variability, *Deep Sea Res., Part I*, *51*, 2123–2136.
- Kalnay, E., et al. (1996), The NCEP/NCAR 40-year reanalysis project, *Bull. Am. Meteorol. Soc.*, *77*, 437–471.
- Kawamura, R. (1988), Intraseasonal variability of sea surface temperatures over the tropical western Pacific, *J. Meteorol. Soc. Jpn.*, *66*, 1007–1012.
- Kawamura, R., T. Matsumura, and S. Iizuka (2001), Role of equatorially asymmetric sea surface temperature anomalies in the Indian Ocean in the Asian summer monsoon and El Niño-Southern Oscillation coupling, *J. Geophys. Res.*, *106*, 4681–4693.
- Klein, S. A., B. J. Soden, and N.-C. Lau (1999), Remote sea surface temperature variations during ENSO: Evidence for a tropical atmospheric bridge, *J. Clim.*, *12*, 917–932.
- Knutson, T. R., T. L. Delworth, K. W. Dixon, and R. J. Stouffer (1999), Model assessment of regional surface temperature trends (1949–1997), *J. Geophys. Res.*, *104*, 30,981–30,996, doi:10.1029/1999JD900965.
- Knutson, T. R., T. L. Delworth, K. W. Dixon, I. M. Held, J. Lu, V. Ramaswamy, and M. D. Schwarzkopf (2006), Assessment of twentieth-century regional surface temperature trends using the GFDL CM coupled models, *J. Clim.*, *19*, 1624–1651.
- Koch-Larrouy, A., G. Madec, P. Bouruet-Aubertot, T. Gerkema, L. Bessières, and R. Molcard (2007), On the transformation of Pacific Water into Indonesian Throughflow Water by internal tidal mixing, *Geophys. Res. Lett.*, *34*, L04604, doi:10.1029/2006GL028405.
- Kosaka, Y., and H. Nakamura (2006), Structure and dynamics of the summertime Pacific-Japan teleconnection pattern, *Q. J. R. Meteorol. Soc.*, *132*, 2009–2030.
- Kug, J.-S., and I.-S. Kang (2006), Interactive feedback between ENSO and the Indian Ocean, *J. Clim.*, *19*, 1784–1801.
- Kug, J.-S., I.-S. Kang, J.-Y. Lee, and J.-G. Jhun (2004), A statistical approach to Indian Ocean sea surface temperature prediction using a dynamical ENSO prediction, *Geophys. Res. Lett.*, *31*, L09212, doi:10.1029/2003GL019209.
- Kug, J.-S., T. Li, S.-I. An, I.-S. Kang, J.-J. Luo, S. Masson, and T. Yamagata (2006), Role of the ENSO-Indian Ocean coupling on ENSO variability in a coupled GCM, *Geophys. Res. Lett.*, *33*, L09710, doi:10.1029/2005GL024916.
- Kushner, P. J., I. M. Held, and T. L. Delworth (2001), Southern Hemisphere atmospheric circulation response to global warming, *J. Clim.*, *14*, 2238–2249.
- Latif, M., D. Dommengot, M. Dima, and A. Grotzner (1999), The role of Indian Ocean sea surface temperature in forcing east African rainfall anomalies during December–January 1997/98, *J. Clim.*, *12*, 3497–3504.
- Lau, N.-C., and M. J. Nath (2003), Atmosphere-ocean variations in the Indo-Pacific sector during ENSO episodes, *J. Clim.*, *16*, 3–20.
- Lau, N.-C., and M. J. Nath (2004), Coupled GCM simulation of atmosphere-ocean variability associated with zonally asymmetric SST changes in the tropical Indian Ocean, *J. Clim.*, *17*, 245–265.
- Lau, N.-C., A. Leetmaa, and M. J. Nath (2006), Attribution of atmospheric variations in the 1997–2003 period to SST anomalies in the Pacific and Indian Ocean basins, *J. Clim.*, *19*, 3607–3627.
- Lau, W. K. M., and D. E. Waliser (2005), *Intraseasonal Variability of the Atmosphere-Ocean Climate System*, 474 pp., Springer, Heidelberg, Germany.
- Lawrence, D. M., and P. J. Webster (2002), The boreal summer intraseasonal oscillation: Relationship between northward and eastward movement of convection, *J. Atmos. Sci.*, *59*, 1593–1606.
- Lee, T. (2004), Decadal weakening of the shallow overturning circulation in the South Indian Ocean, *Geophys. Res. Lett.*, *31*, L18305, doi:10.1029/2004GL020884.
- Lee, T., and M. J. McPhaden (2008), Decadal phase change in large-scale sea level and winds in the Indo-Pacific region at the end of the 20th century, *Geophys. Res. Lett.*, *35*, L01605, doi:10.1029/2007GL032419.
- Levitus, S., J. I. Antonov, T. P. Boyer, and C. Stephens (2000), Warming of the world ocean, *Science*, *287*, 2225–2229.
- Levitus, S., J. Antonov, and T. Boyer (2005), Warming of the world ocean, 1955–2003, *Geophys. Res. Lett.*, *32*, L02604, doi:10.1029/2004GL021592.
- Li, T., B. Wang, C.-P. Chang, and Y. Zhang (2003), A theory for the Indian Ocean Dipole-Zonal Mode, *J. Atmos. Sci.*, *60*, 2119–2135.
- Lin, J. L., et al. (2006), Tropical intraseasonal variability in 14 IPCC AR4 climate models. Part I: Convective signals, *J. Clim.*, *19*, 2665–2690.
- Liu, Z., and M. Alexander (2007), Atmospheric bridge, oceanic tunnel, and global climatic teleconnections, *Rev. Geophys.*, *45*, RG2005, doi:10.1029/2005RG000172.
- Loschnigg, J., G. A. Meehl, P. J. Webster, J. M. Arblaster, and G. P. Compo (2003), The Asian monsoon, the Tropospheric Biennial Oscillation, and the Indian Ocean Zonal Mode in the NCAR CSM, *J. Clim.*, *16*, 1617–1642.

- Lu, J., and T. L. Delworth (2005), Oceanic forcing of the late 20th century Sahel drought, *Geophys. Res. Lett.*, *32*, L22706, doi:10.1029/2005GL023316.
- Lu, J., R. J. Greatbatch, and K. A. Peterson (2004), Trend in Northern Hemisphere winter atmospheric circulation during the last half of the twentieth century, *J. Clim.*, *17*, 3745–3760.
- Lumpkin, R., and K. Speer (2007), Global ocean meridional overturning, *J. Phys. Oceanogr.*, *37*, 2550–2562.
- Luo, J.-J., S. Masson, S. Behera, S. Shingu, and T. Yamagata (2005), Seasonal climate predictability in a coupled OAGCM using a different approach for ensemble forecasts, *J. Clim.*, *18*, 4474–4497.
- Luo, J.-J., S. Masson, S. Behera, and T. Yamagata (2007), Experimental forecasts of Indian Ocean Dipole using a coupled OAGCM, *J. Clim.*, *20*, 2178–2190.
- Madden, R. A., and P. R. Julian (1972), Description of global-scale circulation cells in the tropics with a 40–50 day period, *J. Atmos. Sci.*, *28*, 3138–3158.
- Masumoto, Y., and G. Meyers (1998), Forced Rossby waves in the southern tropical Indian Ocean, *J. Geophys. Res.*, *103*, 27,589–27,602.
- Masumoto, Y., H. Hase, Y. Kuroda, H. Matsuura, and K. Takeuchi (2005), Intraseasonal variability in the upper layer currents observed in the eastern equatorial Indian Ocean, *Geophys. Res. Lett.*, *32*, L02607, doi:10.1029/2004GL021896.
- Maximenko, N. A., and P. P. Niiler (2005), Hybrid decade-mean global sea level with mesoscale resolution, in *Recent Advances in Marine Science and Technology*, edited by N. Saxena, pp. 55–59, PACON Int., Honolulu.
- McCreary, J. P. (1981), A linear stratified ocean model of the coastal undercurrent, *Philos. Trans. R. Soc. London*, *298*, 603–635.
- McCreary, J. P., Jr., and D. L. T. Anderson (1991), An overview of coupled ocean-atmosphere models of El Niño and the Southern Oscillation, *J. Geophys. Res.*, *96*, 3125–3150, doi:10.1029/90JC01979.
- McCreary, J. P., Jr., P. K. Kundu, and R. L. Molinari (1993), A numerical investigation of dynamics, thermodynamics and mixed-layer processes in the Indian Ocean, *Prog. Oceanogr.*, *31*, 181–244.
- McCreary, J. P., R. Furue, T. Jensen, H.-W. Kang, B. Bang, and T. Qu (2007), Interactions between the Indonesian Throughflow and circulations in the Indian and Pacific oceans, *Prog. Oceanogr.*, *75*, 70–114.
- McPhaden, M. J. (2008), Evolution of the 2006–07 El Niño: The role of intraseasonal to interannual time scale dynamics, *Adv. Geosci.*, *14*, 219–230.
- McPhaden, M. J., et al. (2009), RAMA: The Research Moored Array for African-Asian-Australian Monsoon Analysis and Prediction, *Bull. Am. Meteorol. Soc.*, in press.
- Meehl, G. A., and J. M. Arblaster (2002), The Tropical Biennial Oscillation and Asian-Australian monsoon rainfall, *J. Clim.*, *15*, 722–744.
- Meehl, G. A., J. M. Arblaster, and J. Loschnigg (2003), Coupled ocean-atmosphere dynamical processes in the tropical Indian and Pacific oceans and TBO, *J. Clim.*, *16*, 2138–2158.
- Meyers, G. (1996), Variation of Indonesian Throughflow and the El Niño–Southern Oscillation, *J. Geophys. Res.*, *101*(C5), 12,255–12,263.
- Meyers, G., and R. Boscolo (2006), The Indian Ocean Observing System (IndOOS), *CLIVAR Exch.*, *11*, 2–3.
- Meyers, G., P. McIntosh, L. Pigot, and M. Pook (2007), The years of El Niño, La Niña, and interactions with the tropical Indian Ocean, *J. Clim.*, *20*, 2872–2880.
- Misra, V. (2004), The teleconnection between the western Indian and the western Pacific Oceans, *Mon. Weather Rev.*, *132*, 445–455.
- Miyama, T., J. P. McCreary Jr., T. G. Jensen, J. Loschnigg, S. Godfrey, and A. Ishida (2003), Structure and dynamics of the Indian Ocean cross-equatorial cell, *Deep Sea Res., Part II*, *50*, 2023–2047.
- Miyama, T., J. P. McCreary Jr., T. G. Jensen, D. Sengupta, and R. Senan (2006), Dynamics of biweekly oscillations in the equatorial Indian Ocean, *J. Phys. Oceanogr.*, *36*, 827–846.
- Murtugudde, R., and A. J. Busalacchi (1999), Interannual variability of the dynamics and thermodynamics, and mixed layer processes in the Indian Ocean, *J. Clim.*, *12*, 2300–2326.
- Murtugudde, R., J. P. McCreary, and A. J. Busalacchi (2000), Oceanic processes associated with anomalous events in the Indian Ocean with relevance to 1997–1998, *J. Geophys. Res.*, *105*, 3295–3306.
- Nagura, M., and M. Konda (2007), The seasonal development of an SST anomaly in the Indian Ocean and its relationship to ENSO, *J. Clim.*, *20*, 38–52.
- Neelin, J. D., D. S. Battisti, A. C. Hirst, F.-F. Jin, Y. Wakata, T. Yamagata, and S. E. Zebiak (1998), ENSO theory, *J. Geophys. Res.*, *103*, 14,261–14,290.
- Nigam, S., and H. S. Shen (1993), Structure of oceanic and atmospheric low-frequency variability over the tropical Pacific and Indian Oceans. Part I: COADS observations, *J. Clim.*, *6*, 657–676.
- Niiler, P. P., N. A. Maximenko, and J. C. McWilliams (2003), Dynamically balanced absolute sea level of the global ocean derived from near-surface velocity observations, *Geophys. Res. Lett.*, *30*(22), 2164, doi:10.1029/2003GL018628.
- Nitta, T. (1987), Convective activities in the tropical western Pacific and their impact on the Northern Hemisphere summer circulation, *J. Meteorol. Soc. Jpn.*, *65*, 373–390.
- Ohba, M., and H. Ueda (2006), A role of zonal gradient of SST between the Indian Ocean and the western Pacific in localized convection around the Philippines, *SOLA*, *2*, 176–179.
- Palastanga, V., P. J. van Leeuwen, and W. P. M. de Ruijter (2006), A link between low-frequency mesoscale eddy variability around Madagascar and the large-scale Indian Ocean variability, *J. Geophys. Res.*, *111*, C09029, doi:10.1029/2005JC003081.
- Palastanga, V., P. J. van Leeuwen, M. W. Schouten, and W. P. M. de Ruijter (2007), Flow structure and variability in the subtropical Indian Ocean: Instability of the South Indian Ocean Counter-current, *J. Geophys. Res.*, *112*, C01001, doi:10.1029/2005JC003395.
- Palmer, T. N. (1986), The influence of Atlantic, Pacific, and Indian oceans on Sahel rainfall, *Nature*, *322*, 251–253.
- Penven, P., J. R. E. Lutjeharms, and P. Florenchie (2006), Madagascar: A pacemaker for the Agulhas Current system?, *Geophys. Res. Lett.*, *33*, L17609, doi:10.1029/2006GL026854.
- Perigaud, C., and P. Delecluse (1993), Interannual sea level variations in the tropical Indian Ocean from Geosat and shallow-water simulations, *J. Phys. Oceanogr.*, *23*, 1916–1934.
- Philander, S. G. H. (1990), *El Niño, La Niña, and the Southern Oscillation*, 293 pp., Academic, San Diego, Calif.
- Potemra, J. T., and N. Schneider (2007), Interannual variations of the Indonesian Throughflow, *J. Geophys. Res.*, *112*, C05035, doi:10.1029/2006JC003808.
- Potemra, J. T., S. L. Hautala, J. Sprintall, and W. Pandoe (2002), Interaction between the Indonesian seas and the Indian Ocean in observations and numerical models, *J. Phys. Ocean.*, *32*, 1838–1854.
- Qu, T., and G. Meyers (2005), Seasonal variation of barrier layer in the southeastern tropical Indian Ocean, *J. Geophys. Res.*, *110*, C11003, doi:10.1029/2004JC002816.
- Quartly, G. D., J. J. H. Buck, M. A. Srokosz, and A. C. Coward (2006), Eddies around Madagascar—The retroflexion re-considered, *J. Mar. Syst.*, *63*(3–4), 115–129, doi:10.1016/j.jmarsys.2006.06.001.
- Rao, S. A., and S. K. Behera (2005), Subsurface influence on SST in the tropical Indian Ocean: Structure and interannual variability, *Dyn. Atmos. Oceans*, *39*, 103–135.
- Rayner, N. A., P. Brohan, D. E. Parker, C. K. Folland, J. J. Kennedy, M. Vanicek, T. Ansell, and S. F. B. Tett (2006),

- Improved analyses of changes and uncertainties in sea surface temperature measured in situ since the mid-nineteenth century: The HadSST2 data set, *J. Clim.*, *19*, 446–469.
- Reason, C. J. C. (2002), Sensitivity of the southern African circulation to dipole sea-surface temperature patterns in the South Indian Ocean, *Int. J. Climatol.*, *20*, 377–393.
- Reppin, J., F. Schott, and J. Fischer (1999), Equatorial currents and transports in the upper central Indian Ocean: Annual cycle and interannual variability, *J. Geophys. Res.*, *104*(C7), 15,495–15,514.
- Reverdin, G., D. Cadel, and D. Gutzler (1986), Interannual displacements of convection and surface circulation over the equatorial Indian Ocean, *Q. J. R. Meteorol. Soc.*, *112*, 43–67.
- Ridgway, K. R., and J. R. Dunn (2007), Observational evidence for a Southern Hemisphere oceanic supergyre, *Geophys. Res. Lett.*, *34*, L13612, doi:10.1029/2007GL030392.
- Ropelewski, F., and M. S. Halpert (1987), Global and regional scale precipitation patterns associated with the El Niño/Southern Oscillation, *Mon. Weather Rev.*, *115*, 1602–1626.
- Roxy, M., and Y. Tanimoto (2007), Role of SST over the Indian Ocean in influencing the intraseasonal variability of the Indian summer monsoon, *J. Meteorol. Soc. Jpn.*, *85*, 349–358.
- Rui, H., and B. Wang (1990), Development characteristics and dynamic structure of tropical intraseasonal convection anomalies, *J. Atmos. Sci.*, *47*, 357–379.
- Saji, N. H., and T. Yamagata (2003), Structure of SST and surface wind variability during Indian Ocean Dipole mode events: COADS observations, *J. Clim.*, *16*, 2735–2751.
- Saji, N. H., B. N. Goswami, P. N. Vinayachandran, and T. Yamagata (1999), A dipole in the tropical Indian Ocean, *Nature*, *401*, 360–363.
- Saji, N. H., S.-P. Xie, and T. Yamagata (2006a), Tropical Indian Ocean variability in the IPCC 20th-century climate simulations, *J. Clim.*, *19*, 4397–4417.
- Saji, N. H., S.-P. Xie, and C.-Y. Tam (2006b), Satellite observations of intense intraseasonal cooling events in the tropical South Indian Ocean, *Geophys. Res. Lett.*, *33*, L14704, doi:10.1029/2006GL026525.
- Saravanan, R., and P. Chang (2000), Interaction between tropical Atlantic variability and El Niño–Southern Oscillation, *J. Clim.*, *13*, 2177–2194.
- Schiller, A., and J. S. Godfrey (2003), Indian Ocean intraseasonal variability in an ocean general circulation model, *J. Clim.*, *16*, 21–39.
- Schoenefeldt, R., and F. A. Schott (2006), Decadal variability of the Indian Ocean cross-equatorial exchange in SODA, *Geophys. Res. Lett.*, *33*, L08602, doi:10.1029/2006GL025891.
- Schott, F., and J. P. McCreary (2001), The monsoon circulation of the Indian Ocean, *Prog. Oceanogr.*, *51*, 1–123.
- Schott, F., M. Dengler, and R. Schoenefeldt (2002), The shallow thermohaline circulation of the Indian Ocean, *Prog. Oceanogr.*, *53*, 57–103.
- Schott, F. A., J. P. McCreary, and G. C. Johnson (2004), Shallow overturning circulations of the tropical-subtropical oceans, in *Earth Climate: The Ocean-Atmosphere Interaction*, *Geophys. Monogr. Ser.*, vol. 147, edited by C. Wang, S.-P. Xie, and J. A. Carton, pp. 261–304, AGU, Washington, D. C.
- Sengupta, D., R. Senan, and B. N. Goswami (2001), Origin of intraseasonal variability of circulation in the tropical central Indian Ocean, *Geophys. Res. Lett.*, *28*, 1267–1270.
- Sengupta, D., R. Senan, V. S. N. Murty, and V. Fernando (2004), A biweekly mode in the equatorial Indian Ocean, *J. Geophys. Res.*, *109*, C10003, doi:10.1029/2004JC002329.
- Sengupta, D., R. Senan, and B. N. Goswami (2007), Intraseasonal variability of equatorial Indian Ocean zonal currents, *J. Clim.*, *20*, 3036–3055.
- Shenoi, S. S. C., D. Shankar, and S. R. Shetye (2004), Remote forcing annihilates barrier layer in southeastern Arabian Sea, *Geophys. Res. Lett.*, *31*, L05307, doi:10.1029/2003GL019270.
- Shi, G., J. Ribbe, W. Cai, and T. Cowan (2007), Multidecadal variability in the transmission of ENSO signals to the Indian Ocean, *Geophys. Res. Lett.*, *34*, L09706, doi:10.1029/2007GL029528.
- Shinoda, T., and W. Han (2005), Influence of the Indian Ocean Dipole on atmospheric subseasonal variability, *J. Clim.*, *18*, 3891–3909.
- Shinoda, T., H. H. Hendon, and J. Glick (1998), Intraseasonal variability of surface fluxes and sea surface temperature in the tropical western Pacific and Indian Ocean, *J. Clim.*, *11*, 1685–1702.
- Shinoda, T., M. A. Alexander, and H. H. Hendon (2004), Remote response of the Indian Ocean to interannual SST variations in the tropical Pacific, *J. Clim.*, *17*, 362–372.
- Siedler, G., M. Rouault, and J. R. E. Lutjeharms (2006), Structure and origin of the subtropical South Indian Ocean Countercurrent, *Geophys. Res. Lett.*, *33*, L24609, doi:10.1029/2006GL027399.
- Slingo, J. M., et al. (1996), Intraseasonal oscillations in 15 atmospheric general circulation models: Results from an AMIP diagnostic subproject, *Clim. Dyn.*, *12*, 325–357.
- Sobel, A. H., I. M. Held, and C. S. Bretherton (2002), The ENSO signal in tropical tropospheric temperature, *J. Clim.*, *18*, 2702–2706.
- Song, Q., A. L. Gordon, and M. Visbeck (2004), Spreading of the Indonesian Throughflow in the Indian Ocean, *J. Phys. Oceanogr.*, *34*, 772–792.
- Song, Q., G. A. Vecchi, and A. J. Rosati (2008), Predictability of the Indian Ocean sea surface temperature anomalies in the GFDL coupled model, *Geophys. Res. Lett.*, *35*, L02701, doi:10.1029/2007GL031966.
- Speich, S., B. Blanke, P. de Vries, S. Drijfhout, K. Döös, A. Ganachaud, and R. Marsh (2002), Tasman leakage: A new route in the global ocean conveyor belt, *Geophys. Res. Lett.*, *29*(10), 1416, doi:10.1029/2001GL014586.
- Speich, S., B. Blanke, and W. Cai (2007), Atlantic meridional overturning circulation and the Southern Hemisphere supergyre, *Geophys. Res. Lett.*, *34*, L23614, doi:10.1029/2007GL031583.
- Spencer, H., R. T. Sutton, J. M. Slingo, M. Roberts, and E. Black (2005), Indian Ocean climate and dipole variability in Hadley Centre coupled GCMs, *J. Clim.*, *18*, 2286–2306.
- Stammer, D., K. Ueyoshi, A. Khl, W. G. Large, S. A. Josey, and C. Wunsch (2004), Estimating air-sea fluxes of heat, freshwater, and momentum through global ocean data assimilation, *J. Geophys. Res.*, *109*, C05023, doi:10.1029/2003JC002082.
- Su, H., J. D. Neelin, and C. Chou (2001), Tropical teleconnection and local response to SST anomalies during the 1997–98 El Niño, *J. Geophys. Res.*, *106*, 20,025–20,043.
- Susanto, R. D., A. L. Gordon, and Q. Zheng (2001), Upwelling along the coasts of Java and Sumatra and its relation to ENSO, *Geophys. Res. Lett.*, *28*(8), 1599–1602, doi:10.1029/2000GL011844.
- Terray, P., and S. Dominiak (2005), Indian Ocean sea surface temperature and El Niño–Southern Oscillation: A new perspective, *J. Clim.*, *18*, 1351–1368.
- Tokinaga, H., and Y. Tanimoto (2004), Seasonal transition of SST anomalies in the tropical Indian Ocean during El Niño and Indian Ocean Dipole years, *J. Meteorol. Soc. Jpn.*, *82*, 1007–1018.
- Tourre, Y. M., and W. B. White (2003), Patterns of coherent climate signals in the Indian Ocean during the 20th century, *Geophys. Res. Lett.*, *30*(23), 2224, doi:10.1029/2003GL018476.
- Tozuka, T., J.-J. Luo, S. Masson, and T. Yamagata (2007), Decadal modulations of the Indian Ocean Dipole in the SINTEX-F1 coupled GCM, *J. Clim.*, *20*, 2881–2894, doi:10.1175/JCLI4168.1.
- Trenary, L. L., and W. Han (2008), Causes of decadal subsurface cooling in the tropical Indian Ocean during 1961–2000, *Geophys. Res. Lett.*, *35*, L17602, doi:10.1029/2008GL034687.
- Vecchi, G. A., and D. E. Harrison (2002), Monsoon breaks and subseasonal sea surface temperature variability in the Bay of Bengal, *J. Clim.*, *15*, 1485–1493.

- Vecchi, G. A., and D. E. Harrison (2004), Interannual Indian rainfall variability and Indian Ocean sea surface temperature anomalies, in *Earth Climate: The Ocean-Atmosphere Interaction*, *Geophys. Monogr. Ser.*, vol. 147, edited by C. Wang, S.-P. Xie, and J. A. Carton, pp. 247–260, AGU, Washington, D. C.
- Vecchi, G. A., and M. J. Harrison (2007), An observing system simulation experiment for the Indian Ocean, *J. Clim.*, *20*, 3300–3319.
- Vecchi, G. A., and B. J. Soden (2007), Global warming and the weakening of the tropical circulation, *J. Clim.*, *20*, 4316–4340.
- Vecchi, G. A., S.-P. Xie, and A. S. Fischer (2004), Ocean-atmosphere co-variability in the western Arabian Sea, *J. Clim.*, *17*, 1213–1224.
- Vecchi, G. A., B. J. Soden, A. T. Wittenberg, I. M. Held, A. Leetmaa, and M. J. Harrison (2006), Weakening of tropical Pacific atmospheric circulation due to anthropogenic forcing, *Nature*, *441*, 73–76.
- Venzke, S., M. Latif, and A. Villwock (2000), The coupled GCM ECHO-2. Part II: Indian Ocean response to ENSO, *J. Clim.*, *13*, 1317–1383.
- Vinayachandran, P. N., N. H. Saji, and T. Yamagata (1999), Response of the equatorial Indian Ocean to an unusual wind event during 1994, *Geophys. Res. Lett.*, *26*(11), 1613–1616, doi:10.1029/1999GL900179.
- Vinayachandran, P. N., J. Kurian, and C. P. Neema (2007), Indian Ocean response to anomalous conditions in 2006, *Geophys. Res. Lett.*, *34*, L15602, doi:10.1029/2007GL030194.
- Wacongne, S., and R. Pacanowski (1996), Seasonal heat transport in a primitive equations model of the tropical Indian Ocean, *J. Phys. Oceanogr.*, *26*(12), 2666–2699.
- Wajsowicz, R. C. (2004), Climate variability over the tropical Indian Ocean sector in the NSIPP seasonal forecast system, *J. Clim.*, *17*, 4783–4804.
- Wajsowicz, R. C. (2005), Potential predictability of tropical Indian Ocean SST anomalies, *Geophys. Res. Lett.*, *32*, L24702, doi:10.1029/2005GL024169.
- Wajsowicz, R. C. (2007), Seasonal-to-interannual forecasting of tropical Indian Ocean sea surface temperature anomalies: Potential predictability and barriers, *J. Clim.*, *20*, 3320–3343.
- Waliser, D. E., R. Murtugudde, and L. E. Lucas (2003), Indo-Pacific Ocean response to atmospheric intraseasonal variability: 1. Austral summer and the Madden-Julian Oscillation, *J. Geophys. Res.*, *108*(C5), 3160, doi:10.1029/2002JC001620.
- Wallace, J. M., E. M. Rasmusson, T. P. Mitchell, V. E. Kousky, E. S. Sarachik, and H. von Storch (1998), On the structure and evolution of ENSO-related climate variability in the tropical Pacific: Lessons from TOGA, *J. Geophys. Res.*, *103*, 14,241–14,259.
- Wang, B., and X. Xie (1997), A model for the boreal summer intraseasonal oscillation, *J. Atmos. Sci.*, *54*, 72–86.
- Wang, B., R. Wu, and X. Fu (2000), Pacific–east Asia teleconnection: How does ENSO affect east Asian climate?, *J. Clim.*, *13*, 1517–1536.
- Wang, B., R. Wu, and T. Li (2003), Atmosphere–warm ocean interaction and its impact on Asian–Australian monsoon variability, *J. Clim.*, *16*, 1195–1211.
- Wang, B., I.-S. Kang, and J.-Y. Lee (2004), Ensemble simulation of Asian–Australian monsoon variability by 11 AGCMs, *J. Clim.*, *17*, 803–818.
- Wang, C., and J. Picaut (2004), Understanding ENSO physics—A review, in *Earth's Climate: The Ocean-Atmosphere Interaction*, *Geophys. Monogr. Ser.*, vol. 147, edited by C. Wang, S.-P. Xie, and J. A. Carton, pp. 21–48, AGU, Washington, D. C.
- Wang, C., W. Wang, D. Wang, and Q. Wang (2006), Interannual variability of the South China Sea associated with El Niño, *J. Geophys. Res.*, *111*, C03023, doi:10.1029/2005JC003333.
- Watanabe, M., and F. Jin (2002), Role of Indian Ocean warming in the development of Philippine Sea anticyclone during ENSO, *Geophys. Res. Lett.*, *29*(10), 1478, doi:10.1029/2001GL014318.
- Weare, B. C. (1979), A statistical study of the relationships between ocean surface temperatures and the Indian monsoon, *J. Atmos. Sci.*, *36*, 2279–2291.
- Webster, P. J. (1983), Mechanisms of low-frequency variability: Surface hydrological effects, *J. Atmos. Sci.*, *40*, 2110–2124.
- Webster, P. J., A. M. Moore, J. P. Loschnigg, and R. R. Leben (1999), Coupled oceanic-atmospheric dynamics in the Indian Ocean during 1997–98, *Nature*, *401*, 356–360.
- Webster, P. J., et al. (2002), The JASMINE pilot study, *Bull. Am. Meteorol. Soc.*, *83*, 1603–1630.
- Wijffels, S., and G. Meyers (2004), An intersection of oceanic waveguides: Variability in the Indonesian Throughflow region, *J. Phys. Oceanogr.*, *34*, 1232–1253.
- Wirth, A., J. Willebrand, and F. Schott (2002), Variability of the Great-Whirl from observations and models, *Deep Sea Res., Part II*, *49*, 1279–1295.
- Wu, G. X., and H. Liu (1995), Neighborhood response of rainfall to tropical sea surface temperature anomalies. Part I: Numerical experiment, *Chin. J. Atmos. Sci.*, *19*, 422–434.
- Wu, R., and B. P. Kirtman (2004), Understanding the impacts of the Indian Ocean on ENSO variability in a coupled GCM, *J. Clim.*, *17*, 4019–4031.
- Wu, R., B. P. Kirtman, and V. Krishnamurthy (2008), An asymmetric mode of tropical Indian Ocean rainfall variability in boreal spring, *J. Geophys. Res.*, *113*, D05104, doi:10.1029/2007JD009316.
- Wyrtki, K. (1973), An equatorial jet in the Indian Ocean, *Science*, *181*, 262–264.
- Xie, S.-P. (1999), A dynamic ocean-atmosphere model of the tropical Atlantic decadal variability, *J. Clim.*, *12*, 64–70.
- Xie, S.-P., and S. G. H. Philander (1994), A coupled ocean-atmosphere model of relevance to the ITCZ in the eastern Pacific, *Tellus, Ser. A*, *46*, 340–350.
- Xie, S.-P., H. Annamalai, F. Schott, and J. P. McCreary Jr. (2002), Origin and predictability of South Indian Ocean climate variability, *J. Clim.*, *15*(8), 864–874.
- Xie, S.-P., Q. Xie, D. X. Wang, and W. T. Liu (2003), Summer upwelling in the South China Sea and its role in regional climate variations, *J. Geophys. Res.*, *108*(C8), 3261, doi:10.1029/2003JC001867.
- Xie, S.-P., H. Xu, N. H. Saji, Y. Wang, and W. T. Liu (2006), Role of narrow mountains in large-scale organization of Asian monsoon convection, *J. Clim.*, *19*, 3420–3429.
- Xie, S.-P., C.-H. Chang, Q. Xie, and D. Wang (2007), Intraseasonal variability in the summer South China Sea: Wind jet, cold filament, and recirculations, *J. Geophys. Res.*, *112*, C10008, doi:10.1029/2007JC004238.
- Xie, S.-P., K. Hu, J. Hafner, H. Tokinaga, Y. Du, G. Huang, and T. Sampe (2009), Indian Ocean capacitor effect on Indo-western Pacific climate during the summer following El Niño, *J. Clim.*, in press.
- Yamagata, T., S. K. Behera, J.-J. Luo, S. Masson, M. Jury, and S. A. Rao (2004), Coupled ocean-atmosphere variability in the tropical Indian Ocean, in *Earth Climate: The Ocean-Atmosphere Interaction*, *Geophys. Monogr. Ser.*, vol. 147, edited by C. Wang, S.-P. Xie, and J. A. Carton, pp. 189–212, AGU, Washington, D. C.
- Yang, J., Q. Liu, S.-P. Xie, Z. Liu, and L. Wu (2007), Impact of the Indian Ocean SST basin mode on the Asian summer monsoon, *Geophys. Res. Lett.*, *34*, L02708, doi:10.1029/2006GL028571.
- Yasunari, T. (1980), A quasi-stationary appearance of 30 to 40 day period in the cloudiness fluctuations during the summer monsoon over India, *J. Meteorol. Soc. Jpn.*, *58*, 225–229.
- Yu, J.-Y., and K. M. Lau (2004), Contrasting Indian Ocean SST variability with and without ENSO influence: A coupled atmosphere-ocean GCM study, *Meteorol. Atmos. Phys.*, *90*, 179–191, doi:10.1007/s00703-004-0094-7.
- Yu, J.-Y., C. R. Mechoso, J. C. McWilliams, and A. Arakawa (2002), Impacts of the Indian Ocean on the ENSO cycle, *Geophys. Res. Lett.*, *29*(8), 1204, doi:10.1029/2001GL014098.

- Yu, J.-Y., S.-P. Weng, and J. D. Farrara (2003), Ocean roles in the TBO transitions of the Indian-Australian monsoon system, *J. Clim.*, *16*, 3072–3080.
- Yu, L., and M. M. Rienecker (1999), Mechanisms for the Indian Ocean warming during the 1997–98 El Niño, *Geophys. Res. Lett.*, *26*, 735–738.
- Yu, L., and R. A. Weller (2007), Objectively analyzed air-sea heat fluxes for the global ice-free oceans (1981–2005), *Bull. Am. Meteorol. Soc.*, *88*, 527–539.
- Yu, L., X. Jin, and R. A. Weller (2007), Annual, seasonal, and interannual variability of air-sea heat fluxes in the Indian Ocean, *J. Clim.*, *20*, 3190–3209.
- Yu, W., B. Xiang, L. Liu, and N. Liu (2005), Understanding the origins of interannual thermocline variations in the tropical Indian Ocean, *Geophys. Res. Lett.*, *32*, L24706, doi:10.1029/2005GL024327.
- Yuan, D., and W. Han (2006), Roles of equatorial waves and western boundary reflection in the seasonal circulation of the equatorial Indian Ocean, *J. Phys. Oceanogr.*, *36*, 930–944.
- Yulaeva, E., and J. M. Wallace (1994), The signature of ENSO in global temperature and precipitation fields derived from the microwave sounding unit, *J. Clim.*, *7*, 1719–1736.
- Zhang, C. (2005), Madden-Julian Oscillation, *Rev. Geophys.*, *43*, RG2003, doi:10.1029/2004RG000158.
- Zhang, R., and T. L. Delworth (2006), Impact of Atlantic multi-decadal oscillations on India/Sahel rainfall and Atlantic hurricanes, *Geophys. Res. Lett.*, *33*, L17712, doi:10.1029/2006GL026267.
- Zheng, Y., D. E. Waliser, W. F. Stern, and C. Jones (2004), The role of coupled sea surface temperatures in the simulation of the tropical intraseasonal oscillation, *J. Clim.*, *17*, 4109–4134.

J. P. McCreary Jr. and S.-P. Xie, International Pacific Research Center, University of Hawai'i, Honolulu, HI 96822, USA. (xie@hawaii.edu)